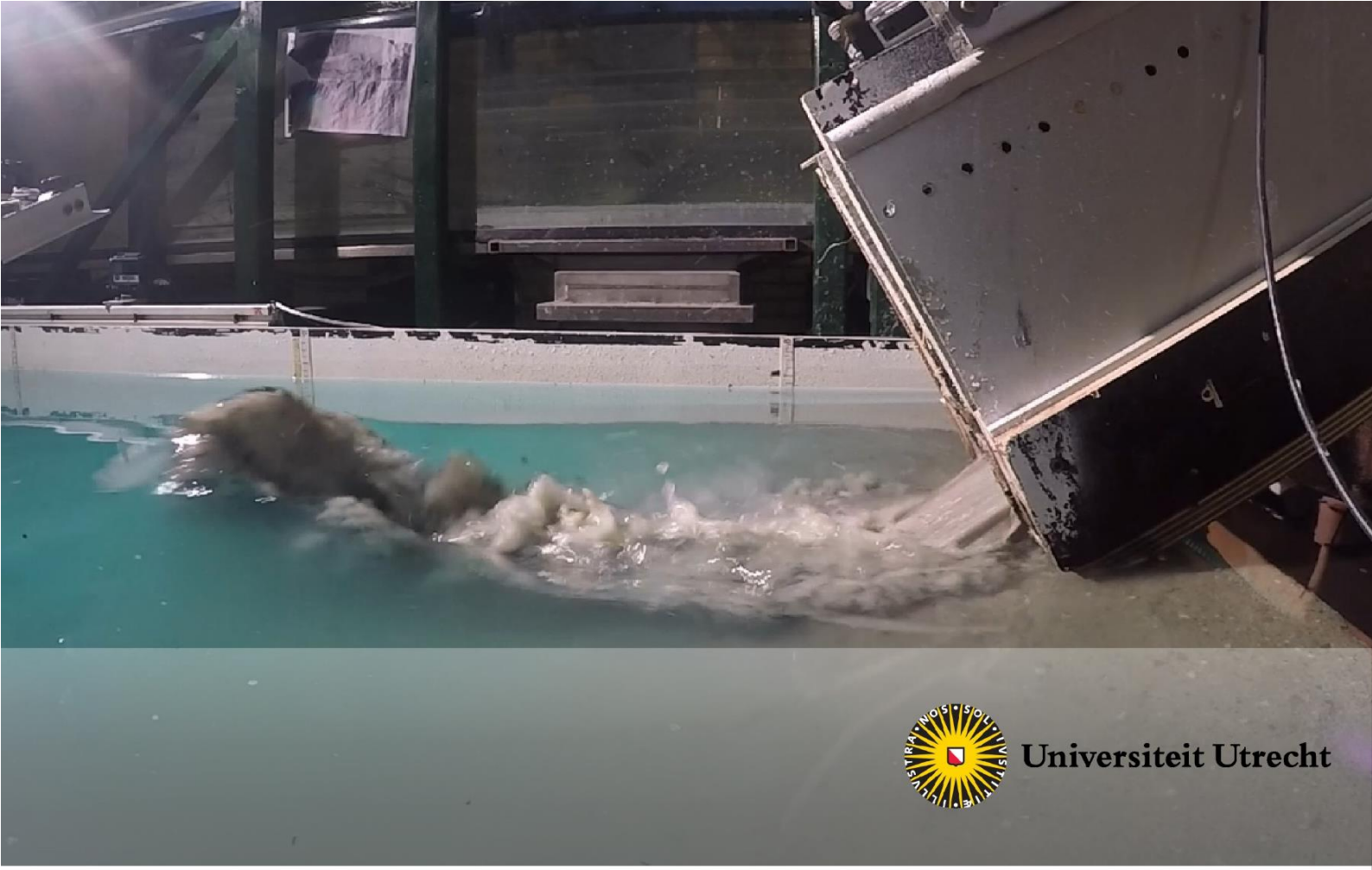

Universiteit Utrecht

Debris-flow generated tsunami waves

Physical experiments of debris-flow generated impulse waves and their dependence on debris-flow properties

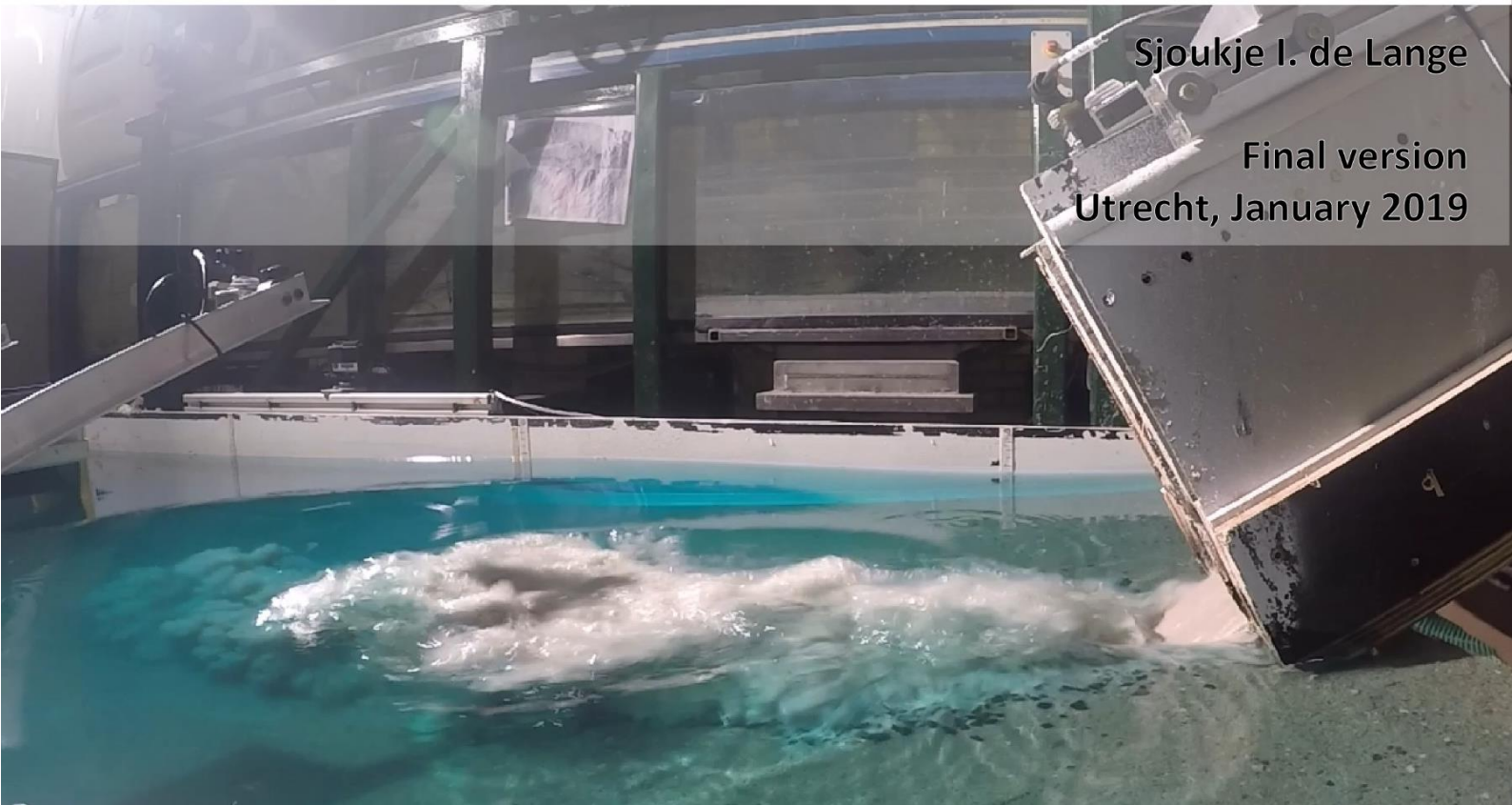

Sjoukje I. de Lange

Final version
Utrecht, January 2019

Debris-flow generated tsunami waves

Master graduation research

Final version
January 2019

Sjoukje I. de Lange (BSc)

4137493

Earth Surface Water

Supervisors

Dr. Tjalling de Haas

Prof. Dr. Maarten G. Kleinhans

Utrecht University

Faculty of Geosciences

Department of Physical Geography

Preface

This thesis is conducted as a part of the final year of the master study Earth Surface Water at Utrecht University. The aim of the assignment is to integrate the knowledge and skills gained in this master in a final project and to get an insight in the world of science.

This thesis continues on the work of Tjalling de Haas, who studies debris flows in an experimental setup. I expand on his research by letting the debris flow debouch in a reservoir and I study the generated tsunami waves. My laboratory partner Nikoleta Santa will study the subaqueous deposits in her master thesis. A famous example which I learned about in the second year of my bachelor is the disaster at the Vajont Dam, Italy 1963, when a landslide debouched into the hydropower lake, causing a tsunami of more than 250 m, which overtopped the just build dam and caused almost 2000 deaths. The relevance is once more confirmed with an earthquake in Sulawesi, Indonesia on 28 September 2018, which resulted in a terrible debris-flow generated tsunami. Indonesia was hit once more in that year, on 22 December 2018 in Lampung, when a volcanic eruption caused a 64 ha flank collapse, resulting in a tsunami wave. I am grateful to be able to contribute to research on such an important topic.

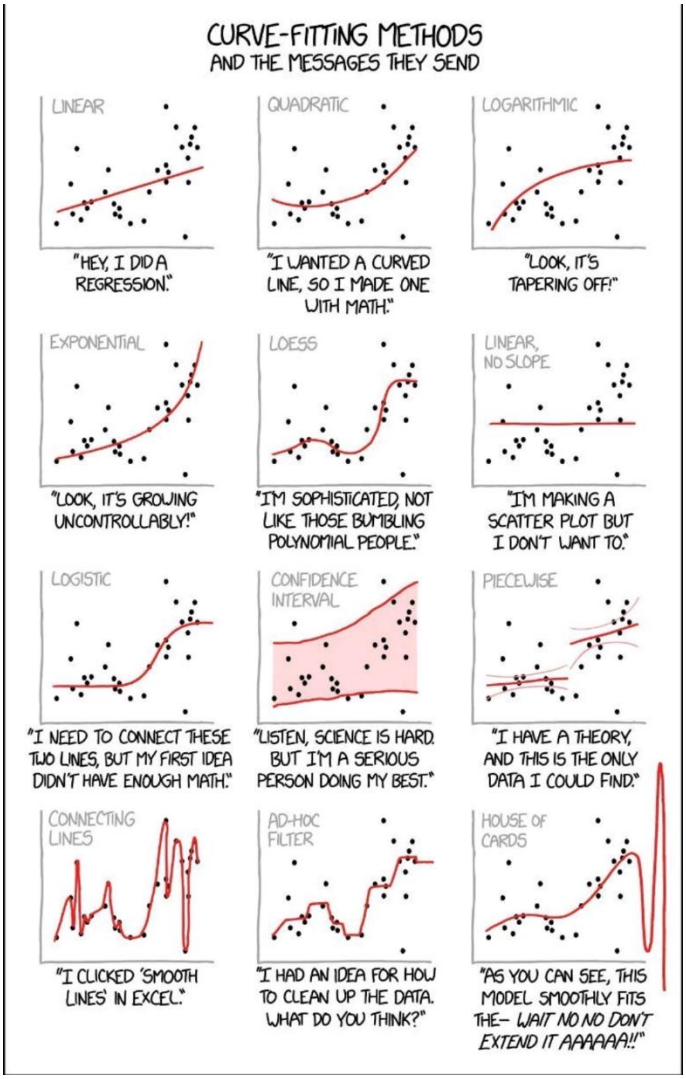

Self-reflection: for those who like scatter....

This research would not have been possible without the help of my first supervisor Tjalling de Haas, his valuable guidance, motivational words, confidence in my work, and his constructive comments to improve this thesis. Gratefulness for my second supervisor Maarten Kleinhans and his unlimited source of ideas. Furthermore, I would like to thank Nikoleta Santa for bringing an enthusiastic and optimistic mood every day we worked together in the laboratory. Next, Shiva Pudasaini from Bonn University is thanked for his physical viewpoint regarding the observations in the laboratory. Also, the technical staff of Utrecht University enabled a smooth progress of the experiments. Arjan van Eijk build and maintained the setup and Bas van Dam provided the technical support. Mark Eijkelboom is thanked for providing sediments for the experiments. Finally, I would like to thank all master students studying in the same workplace as I did for their emotional support.

Sjoukje de Lange

Utrecht, January 2019

Abstract

Debris-flow generated impulse waves can be extremely dangerous for lakeside settlements, and prediction of their characteristics is of major importance for hazard mitigation and management. However, the effects of debris-flow composition on wave generation and evolution are poorly understood. We investigate the influence of multi-phase debris-flow volume, composition (gravel, sand, clay, water) and subaerial outflow slope on wave celerity and amplitude, in a small-scale 3D physical laboratory model. The experimental setup consists of a mixing tank to stir the sediment mixture, a 2.00 m long and 0.12 m wide subaerial outflow channel inclined at 20-40° and a 0.90 m wide and 1.85 m long wave basin inclined at 10°, with a maximum water depth of 0.33 m.

When the debris flow debouches into the water, it transfers a substantial portion of its energy (~10 %) by pushing the water forward, until the wave celerity exceeds the subaqueous debris-flow velocity and the wave becomes 'detached'. The pushing of the debris flow over steepens and accelerates the wave, which increases its non-linearity but does not result in wave breaking.

We demonstrate that debris-flow velocity is the main driver for wave celerity (linearly related at R^2 = 0.79) and wavelength (linearly related at R^2 = 0.64), while debris-flow momentum (velocity times effective mass) mostly determines (far-field) wave amplitude (linearly related at R^2 = 0.60). An increasing debris-flow velocity increases the momentum exerted on the water by the debris flow, thereby increasing the wave celerity. It also increases duration of the pushing, thereby increasing the wave amplitude, which relation is strengthened by a thicker debris flow. Debris-flow velocity is enhanced with an increasing water and clay content (up to 22 %) of the debris flow, which both have a lubricating effect. Debris-flow thickness and thus effective mass, increase with increasing debris-flow volume.

We further show that the existing laws of transfer of momentum of a subaerial debris flow to the water body is applicable for predictions of wave characteristics generated by a multi-phase debris flows, but that formerly developed (semi-empirical) equations need to be adapted by including debris-flow composition and a sloping wave basin, to be able to make accurate predictions. Our results demonstrate the importance of debris-flow composition on impulse wave generation and evolution, and thus the necessity of including flow composition in predictive models.

Key words: "*multi-phase debris flow*", "*tsunami wave*", "*impulse wave*" , "*physical modeling*"

Contents

List of figures

List of tables

List of variables

A_{cell}	area of load cell	m^2
a	wave amplitude	m
Bg	Bagnold number	-
c	wave celerity	m/s
D	hydraulic diffusivity	m^2/s
Dc	Darcy number	-
E	energy	J
Fn	friction number	-
Fr	Froude number (theoretical)	-
Fr_d	Froude number (corrected)	-
Fr_m	Froude number (measured theoretical)	-
$Fr_{m,d}$	Froude number (measured corrected)	-
g	gravitational constant	m/s^2
h	still water depth	m
H	wave height	m
h_s	debris-flow thickness	m
k	hydraulic permeability	m^2
L	length	m
m	mass	kg
M	momentum	Ns
Mn	mass number	-
P	impulse product parameter	-
Re	Reynolds number	-
Re_g	grain Reynolds number	-
Sv	Savage number	-
t	time	s
T	wave period	s
T_p	wave type product	-
u	velocity	m/s
U	Ursell number	-
u_w	wave orbital velocity	m/s

V	volume	m^3
v	kinematic viscosity	m^2/s
v_f	fluid volume fraction	-
v_s	solid volume fraction	-
w	width	m
x_b	location along the wave basin	m
x_c	location along the outflow slope	m
α	outflow slope	°
γ	flow shear rate	1/s
δ	grain diameter	m
ϵ	wave steepness parameter	-
ϵ_c	crest steepness parameter	-
θ	slope of wave basin	°
λ	wavelength	m
Λ	scale factor	-
μ	fluid viscosity	Pa s
ρ	density	kg/m^3
σ	surface tension	N/m
ϕ	angle of internal friction	°

subscripts

1	leading crest/trough
c	crest
eff	effective (until detachment)
s	slide / debris flow
t	trough
w	water
pw	potential, wave

1. Introduction

Debris flows are common in mountainous areas and can cause catastrophic damage. Especially in recent times of climate change, debris flows may become more common and hazardous as a result of increased heavy rainfall events (*Hartmann et al., 2013).* A special condition which increases the potential hazard by a debris flow, is the presence of natural and hydropower lakes, into which debris flows may debouch and form a tsunami wave with devastating effects. Tsunamis are long water waves generated by an abrupt disturbance of the bed or surface of a water body (*Kafle et al., 2016*). Tsunamis created by debris flows are particularly dangerous because of their extreme wave run-up heights, and can flood regions located far away from the shore (Figure 1.1). Besides the creation of a tsunami when a debris flow enters a water body, the debris flow continues as a subaqueous debris flow, where it interacts with the water body. Altogether, the behaviour of different types of debris flow (different in terms of dimensions and composition) and its interaction with the water body are complicated and poorly understood.

Previous researchers have conducted many modelling studies to study the physics of debris-flows generated tsunami waves, but it is hard to verify these due to the lack of experimental or field data. Experimental studies include simplified 2D or 3D experiments with non-deformable blocks or granular uniform sized sediment representing the debris flow, sliding in the water. However, the representation of the debris-flow composition is far from realistic, since experimental debris flows consist in the best case of grains only. Its multi-phase composition, consisting of multiple grain sizes and water, has to date not been used in experimental studies. Also, the influence of composition on impulse wave development and evolution is disregarded. Therefore, there is need for more detailed analyses of the flow dynamics of multi-phase granular debris flows flowing into a body of water, to ultimately predict the impact on the landscape and society.

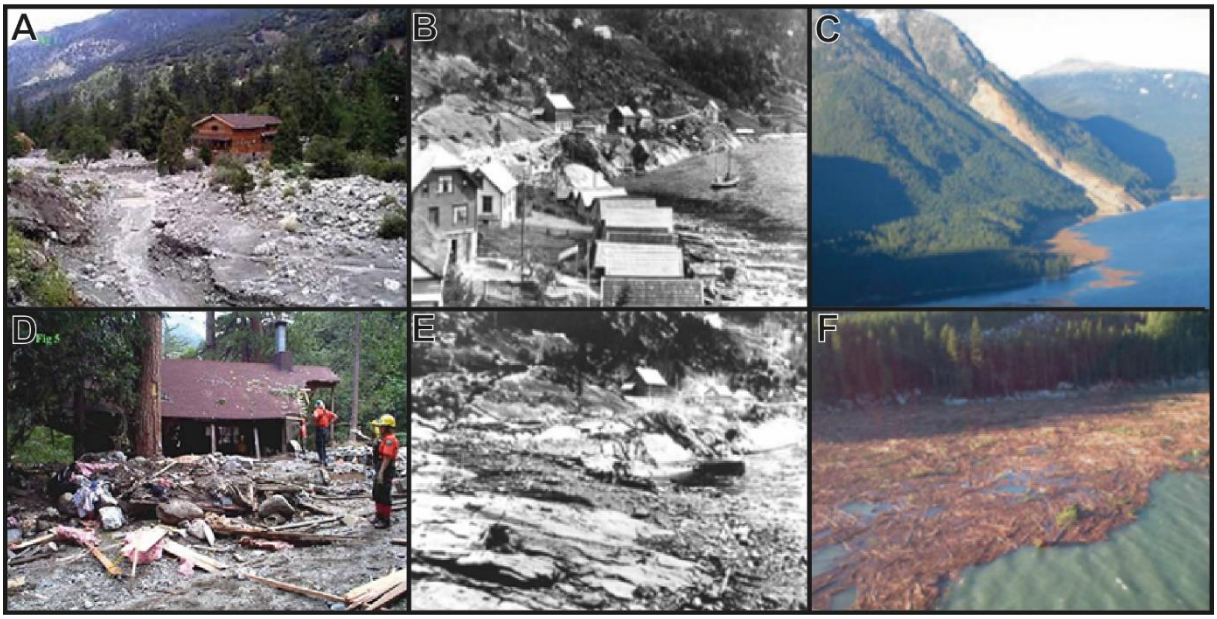

Figure 1.1. Examples of destruction by a debris-flow (inducing tsunami). **A)** Deposits of the debris flow, Mill Creek, Forest Falls (USGS, n.d.). **B)** and **E)** Before (B) and after (E) a debris-flow induced tsunami hit the coast, Tafjord, Norway (1934) (*Sassa & Canuti, 2009*). **C)** and **F)** Rock slide in Chehalis lake (C) and the tsunami damage (F), Vancouver, Canada (*Frank Ullman, n.d.*). **D**) Home destroyed by debris flow (*USGS, n.d.*)

The following main research question will be investigated: *"**How does tsunami wave generation and evolution depend on subaerial topography and debris-flow characteristics?**"*

In this master research, a series of small-scale debris-flow experiments will be conducted in an experimental flume, aiming to perform a detailed analysis on the effects of a debris flow debouching into a reservoir on the wave generation and evolution. The flume consists of a debris mixing tank, a subaerial inclined outflow slope and a water filled inclined wave basin in which the debris flow will generate a tsunami wave and ultimately deposit. *de Haas et al. (2015*) showed that debris-flow composition strongly influences the deposition pattern of subaerial debris flows. Therefore, I will vary the composition (grain sizes and water content) of the debris flow, as well as the flow volume. Ultimately, the outflow slope will be adjusted into different angles. Below, I will start with a theoretical framework around which this research is conducted (chapter 2). An overview of the conducted physical modelling, computer modelling and field studies regarding (subaqueous) debris flows is given. Next, I will describe the experimental setup in which I will measure the subaerial debris flow, subaqueous deposit characteristics (not described in this thesis) and wave generation and evolution (chapter 3). The results of these experiments will be analysed (chapter 4), and possible correlations between debris-flow properties and the resulting tsunami wave will be identified. Furthermore, comparison to existing literature comprising comparable simplified experiments, and natural cases will be performed. In addition, existing (semi-empirical) equations for landslide-tsunami interaction will be tested against my experimental data (chapter 5).

2. Theoretical framework

First, the general characteristics of a subaerial debris flow are discussed (2.1). Next, several important aspects of debris flows will be reviewed. This concerns subaqueous debris flows (2.2) and the tsunami wave generated by a debris flow flowing into a water body (2.3). The current state of knowledge is subdivided in fieldwork studies, physical modelling studies (laboratory studies, experiments) and computer modelling studies. Then I review the scaling dilemma, considering the downscaling of natural processes into an experimental setup (2.4). This chapter is finished with the discussion of the knowledge gap and the contribution of this research (2.5).

2.1 Characteristics of subaerial debris flows

2.1.1 General characteristics

A debris flow is a type of mass wasting, a subcategory of landslides. In this research, both terms are used interchangeably. A debris flow can also be seen as a type of flood, occurring in mountainous areas. These floods happen in three different ways, which all need their own distinct management strategy (*Costa, 1988*). Debris flows, besides water flows and hyper-concentrated flows, are the interest of this research. The following definition of a debris flow is chosen: "A flow of water and sediment particles, moving together as a single viscous body" (*Johnson, 1970*). *Costa (1988*) lists the following characteristics: irreversible sediment entrainment; solids are 70-90 % by mass and 47-77 % by volume; density around 1,800-2,300 kg/m^3; only shear stress along the boundaries. Furthermore, debris flows are gravity driven, flowing over a sloping surface; are poorly sorted and can be coarse grained (up to 10 m in diameter); and are saturated with water (*Iverson, 1997*). Its large volumes (>10^9 m^3), large potential energy release (10^{16} J) and large outflow lengths, give it its unique destructive power (*Iverson, 1997*). Debris flows differ from water flows and hyper-concentrated flows by sediment concentration (higher), density (higher) and shear strength (higher).

The interaction of fluids and solids are important in debris flows. The flow is mostly laminar, and the main support mechanisms are grain related: cohesion is determined by the amount of clay in the flow, and the buoyancy by the difference in density between the particles and supporting fluid. Dispersive stress (*Bagnold, 1954*) develops as particles collide or shear against each other and forces are transmitted. Finally, structural force is caused by grain to grain contact. Figure 2.1 shows the initiation, transport and deposition zone of a debris flow.

2.2.2 Research on subaerial debris flows

Conducting direct fieldwork on an active debris flow is particularly difficult due to the unpredictable occurrence, their destructive power and their often remote locations. Experimental catchments are used to gain insight (*Marchi et al., 2002; Comiti et al., 2014*), but despite that effort, still limited fieldwork studies are conducted on actual flowing subaerial debris flows. However, geological and geomorphological research to debris-flow deposits is performed. The main aim of these studies is to (1) obtain insights in initiation conditions (triggers) and timing (e.g. *Godt & Coe, 2007; Bussman & Anselmetti, 2010*), (2) explain the current landscape and shape of deposits (e.g. *Atwater & More, 1992*), and (3) collect evidence for the occurrence of a catastrophic event (e.g. *Hermanss, 2004*). For my research, fieldwork is less interesting since the actual dynamics within the flow are not easy to measure, and full control over the initial and boundary conditions is required. Therefore, physical and computer modelling is used.

Two distinct types of computer models exist: viscoplastic models and inertial grain flow models. For a review, see *Iverson (1997*). Interestingly, the basic viscoplastic model (Coulomb model) to describe flowing debris, is the same model as for ice flow in glaciers (*Iverson, 1997; Costa, 1988*; *Oerlemans, 2008*).

A lot of physical modelling is conducted regarding debris flow, starting in the mid-nineteenth century and still being a subject undergoing intense study. Experimental setups exist on various spatial scales (1-100 m) (see section 2.5), and most studies cover debris-flow deposits and runout length. Nearly all knowledge about initiation, flow and deposition as described below, is obtained via physical modelling and controlled experiments.

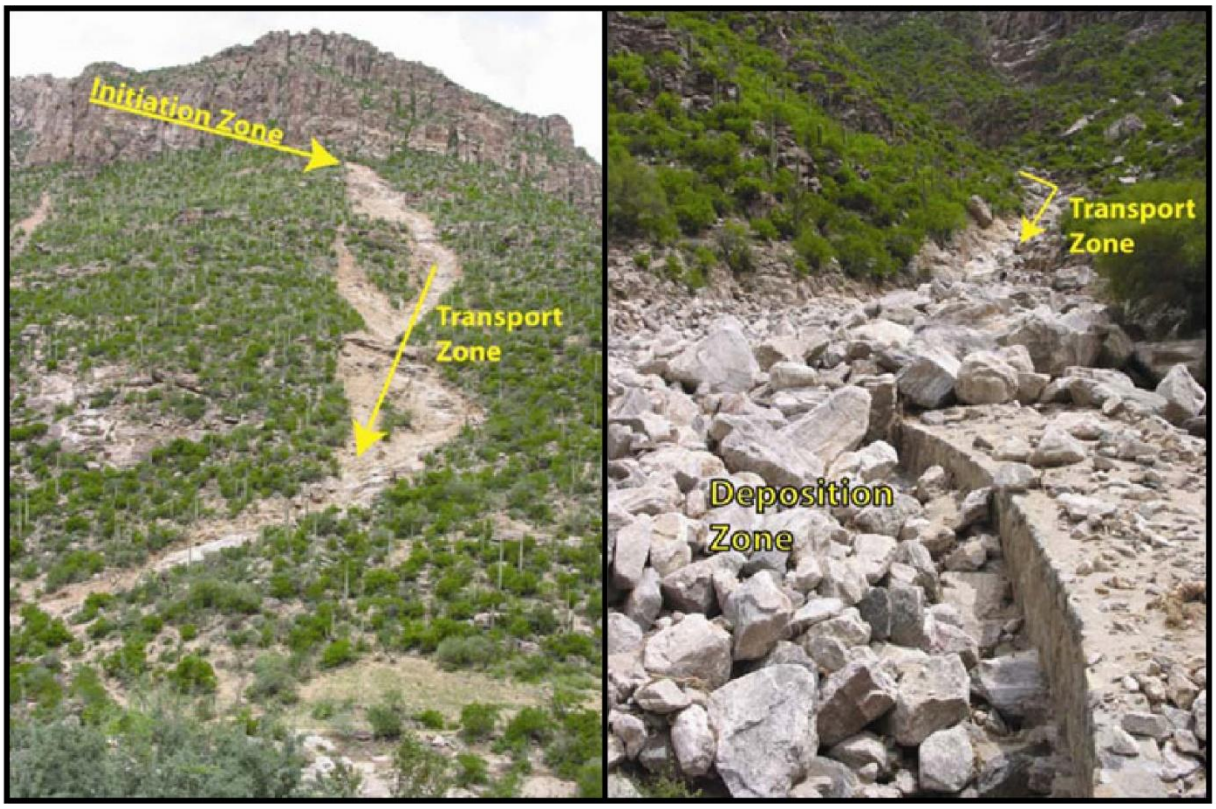

Figure 2.1. Initiation, flow and deposition zone of a debris flow, Arizona (*AZGS, n.d.)*

Initiation. Besides external factors such as earthquakes or volcanic eruptions, three different ways of landslide initiation are acknowledged (*Godt & Coe, 2007*). First, the development of a debris flow from a landslide, mostly occurring in vegetated areas with a thick soil layer. Here, the initiation or mobilization phase is defined as the process by which a debris flow develops from an initially static rigid mass of water-laden soil. For mobilization to occur, mass failure, water saturation and gravitational force work together to deform the soil and to develop a debris flow (*Iverson et al., 1997*). These conditions are mostly met as a result of infiltration of rain or snowfall (*Sitar et al., 1992*). During downslope movement of the landslide, it deforms and incorporates more water, which decreases the strength of the debris and increases the power of the fluid, which causes the mass to flow rather than slide (*Hampton, 1972*). The second process causing debris flow initiation is the transport of downslope material in rills, mostly on sparsely vegetated hill slopes. This type of debris flows has multiple initiation locations (multiple rills) (*Godt & Coe, 2007*), which ultimately merge together to one larger debris flow. Finally, 'firehosing', which often occurs in areas with bare bed rock or soils with a low permeability. When rain water cannot infiltrate in the soil anymore, overland flow occurs. A small overland flow can become concentrated and takes up and scours more and more debris, ultimately developing in a debris flow.

The existence and characteristics (strength, wetness) of the soil appear to be the determining factors for the type of debris flow initiation (*Godt & Coe, 2007; Chen & Yu, 2011*), while the channel gradient plays a role in the characteristics of the debris flow itself (*Van Dine, 1996*).

Flow. When moving, two types of energy facilitate the movement: vibrational energy of the grains and pressure exerted from the supporting fluid (*Iverson, 1997*). The flow moves in one or multiple surges, with a larger flow head and a thinner tail (Figure 2.2). During the flow, the largest clasts (e.g. boulders) are supported by a matrix of finer material (e.g. gravel and clay). The resistance against flow is caused by internal friction, cohesion and viscosity (*Iverson, 1997*). In the initiation phase of a debris flow the downward directed force has to exceed the friction and cohesion before flow occurs. Viscosity plays only a role in a moving debris flow (*Costa, 1988*). For an extensive review about the physics of debris flows, I refer to *Iverson (1997*).

Figure 2.2. Advancing debris-flow fronts. **A)** Nojiri River, Japan, 1987. Flow is 20m wide and 2-3m deep (*By Japan Ministry of Construction; Iverson, 1997*). **B)** Jiang Jia Ravine, China, 1990. Flow is 12m wide and 2-3m deep (*By K.M. Scott; Iverson, 1997).* **C)** Moscardo Torrent, Italy, 2013. (*Comiti et al., 2014*)

Deposition. Larger clasts accumulate at the head of the debris flow due to preferential transport, resulting in a strong lateral grading. The larger-grained front will, when the debris flow loses energy, drain water and form a dam, where behind the smaller grained higher pore pressure part of the flow will also slow down and deposit, or alternatively override the dam (*Iverson, 1997*). Deposits of a debris flow are characterized by marginal levees, a terminal lobe and an U-shaped channel. No vertical stratification is visible in the deposit, only a slight inverse grading at the top layer since buoyant forces result in a concentration of larger clasts at the top.

The USGS (*U.S. Geological Survey*) owns a large experimental flume setup with a length of 95 m, which is used for experiments of subaerial debris flows since 1992 (*Iverson et al., 1992*) and is still active now (*Logan et al., 2018). Johnson et al. (2012*) performed one of the many experiments, aiming to study the grain size segregation in the flow. They measured surface velocity and flow lines by adding tracer pebbles to the debris-flow mixture. After creating the experimental flow, the tracers were distributed in a 'horseshoe-shaped pattern, that became increasingly elevated closer to the deposit termination' and a strong lateral grading, but no vertical grading. A computer simulation of this run made them hypothesize that the transport of coarse material to the front can be explained by shear. However, at the very front the coarse material is overridden, which makes it circulate around in the front of the debris flow. Ultimately, the coarse material is advected to the edges of the flow forming levees enriched in coarse particles (Figure 2.3).

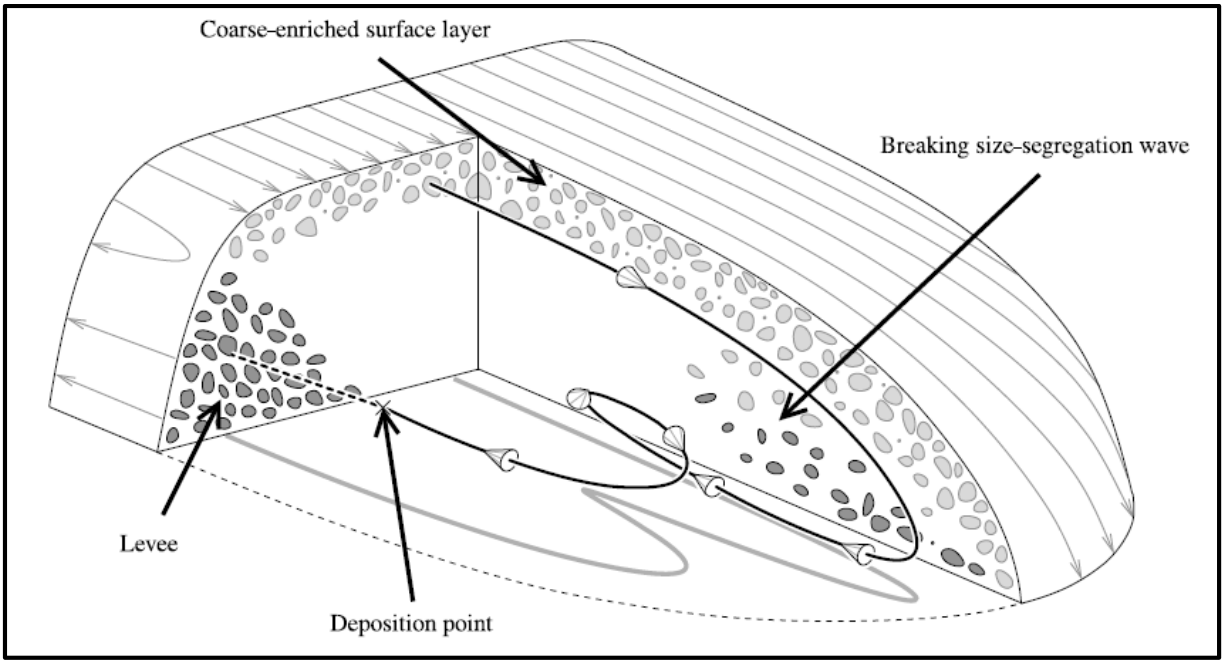

Figure 2.3. Hypothesis about accumulation of coarse material in front and levees of debris flow (*Johnson et al., 2012*)

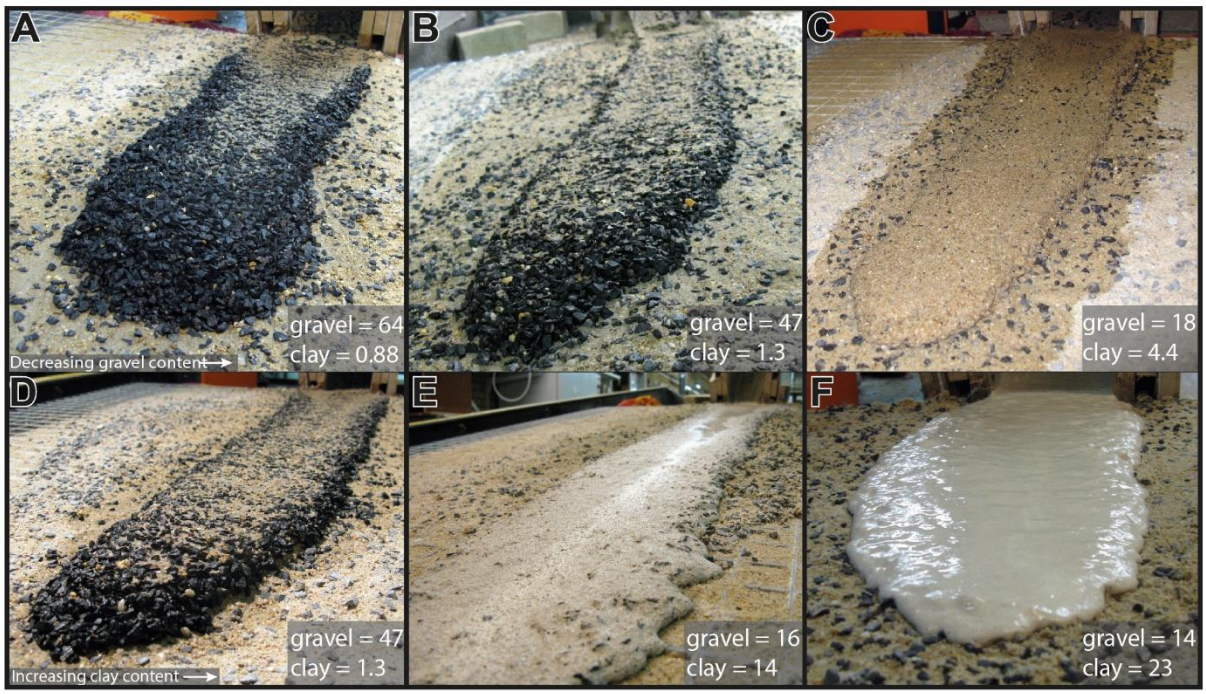

Figure 2.4. Depositional patterns of flow with decreasing gravel content (A-C) and increasing clay content (D-F) (after: *de Haas et al., 2015*)

These depositional patterns are also found in experiments conducted on a much smaller spatial scale, for example in *de Haas et al. (2015*), whose flume is 2.0 m long (Figure 2.4). They studied the influence of topographical parameters (channel slope and width, outflow plain slope) and debris-flow parameters (debris-flow volume and water fraction) on runout distance. They found that the runout distance (and therefore the characteristics of the deposits as researched by *Johnson et al. (2012*) described above) highly depends on the flow composition. The larger the coarse fraction, the larger the runout length until a certain threshold (coarse fraction = 0.4). At this moment, coarse grains accumulate in the front of the flow, increasing frontal friction and decreasing the runout length. Increasing the fraction of smaller particles (clay) also increases the runout length till the moment the

flow becomes too viscous (fraction > 0.2). Fine grains can become suspended in the flow, in which the viscous forces keep them suspended, but also altering the viscosity itself due to its surface electrical forces (*Coussot, 1997*). Larger grains depend on grain-to-grain interaction to remain suspended (*Iverson, 1997*). Hence, flow behaviour depends on the contained grain sizes. The grain size distribution highly influences the pore pressure (*Iverson, 1997*). Coarse-grained fronts have less pore pressure than fine-grained flow-fronts. The high pore pressure in fine grained debris flows, due to the greater compressibility and lower permeability, results in a higher mobility (up to a certain optimum, as shown by *de Haas et al., 2015*).

In short, both the topography and the grain size distribution influence the characteristics of a debris flow and its deposits. However, the characteristics of the deposits of aerial debris flow differ significantly from subaqueous debris flows. We investigate this in the next section.

2.2 Characteristics of subaqueous debris flows

2.2.1 General characteristics

The obvious difference that a subaqueous debris flow flows under water, has direct consequences for its initiation, evolution and deposition (*Locat & Lee, 2005*). Firstly, its main component is water and secondly literature suggests larger runout distances compared to subaerial flows. As opposed to subaerial flows, subaqueous debris flows have a much clearer vertical sorting, and show as well ungraded mud (by direct consolidation) as cross and laminar lamination due to floc settling (*Talling et al., 2012*).

Subaqueous debris flows distinguish themselves from turbidity currents by their laminar flow (*Costa & Williams, 1984; Elverhoi et al., 2000*). The sediment is supported by cohesion, dispersive stress and structural force, as described in section 2.1. However, a single surge event can contain several flow types (*Benzohng et al., 2017*), caused by picking up and depositing sediment and dilution or densification of the flow (*Hampton, 1972*). For example, thin and highly mobile debris flows could have been turbulent on a steeper slope (*Sumner et al., 2009*). Similar to subaerial debris flows, the flow state is mostly depended on the fraction of mud in the flow (*De Blasio et al. 2006*; *Talling et al., 2012*), and a subdivision between strongly coherent and weakly coherent flow is often made (*Yin et al., 2018*). The cohesiveness is caused by a higher mud content, increasing the viscosity and decreasing the permeability. More cohesive debris flows occur closer to the coast and are often caused by slope failure. A low coherent debris flow (sandy flow) is not able to resist water entrainment in the flow (*Yin et al., 2018*), hence the front part of the debris flow becomes turbulent (*Ilstad et al., 2004b)*. Therefore, not only the flow type, but also the outflow length, thickness and sorting highly depend on the sediment composition of the flow. Other factors influencing the outflow length of the debris flow are initial slope and sediment volume (*Elverhoi et al., 2000).* For an extensive explanation of the initiation, flow and deposition of a subaqueous debris flow, I refer to *Locat & Lee (2005*).

2.2.2 Research on subaqueous debris flows

Measuring subaqueous debris flows in the field involves the same problems as for subaerial debris flows. Therefore, only 5 direct measurements worldwide are conducted (*Talling et al., 2012*), and most of the field work focusses on deriving depositional processes from deposits (*Prior et al., 1984; LaBerg & Vorren, 1995*).

Numerical models are used to predict runout distance and impact pressure. The simple first 1D model was made in 1981 by *Edgers & Carlsrund*, and later more complex viscous models (*Imran et al., 2001*), viscoplastic models (*Norem et al., 1990*) and two-phase models (*Gauer et al., 2004*) were set up. Three-phase models, where water and multiple grain sizes can be included, have to become topic of future research.

Recent laboratory studies focus primarily on the exceptional high mobility of subaqueous debris flows observed in the lab (which cannot only be explained by the viscoplastic behaviour (*Elverhoi et al., 2000))* and mainly deal with hydroplaning and outrunner blocks.

Hydroplaning is the phenomenon that the front of the debris flow is heaved above the sea or lake bed by thin water layer (Figure 2.5). It is physically modelled by using a centrifugal setup in 1g (*Deng et al., 2017, Yin et al., 2018*) and in 40g (*Acosta et al., 2017*) or a (2D) flume (*Mohrig et al., 1999; Ilstad et al., 2004a, Yin & Rui, 2017*). Two hypotheses are proposed for this effect. First, the moving debris flows exerts a force on the water body, which induces a pressure higher than hydrostatic. There is an excess of pore water pressure, which results into the development of a layer of water which reduces the basal friction (*Elverhoi et al.,* 2000) and functions as a sliding surface (*Acosta et al., 2017*). Hydroplaning only occurs if the main part of the debris flow does not devolve into suspension (which happens in sandy debris flows (*De Blasio et al. 2006*)) and the flow velocity is large enough (*Elverhoi et al., 2000*). The flow therefore must be coherent, so the water cannot penetrate through the fluidized head. Hydroplaning is therefore not an explanation for the high mobility of sandy debris flows (*De Blasio et al., 2006*), rather the fluidized head causing low bed friction (*Ilstad et al., 2004a*). This is why *Deng et al. (2017*) proposed a different hypothesis for the high mobility of subaqueous debris flows. In a dense fast debris flow, particles hit the bottom plane of the flume. Thereby, fluid pressure between the debris flow and the bottom is increased, and hydroplaning can occur. As the water layer intrudes under the debris flow, the amount of collisions decreases, causing the flow to loose kinetic energy more slowly, hence the runout distance is increased (*Yin et al., 2018*). Hydroplaning can strongly influence the outflow length and interaction with the water, and the acceleration of the front can even lead to detachment of the body (*Mohrig et al., 1998; Ilstad et al., 2004c*). Hydroplaning is therefore an often-proposed hypothesis for the existence of outrunner blocks (*Mohrig et al., 1998; Ilstad et al., 2004c*) and the differences in outflow length between subaerial and subaqueous flows (*Mohrig et al., 1999*). Outrunner blocks are pieces of debris that detach from the subaqueous landslide and travel and deposit significantly further than the debris-flow front (*De Blasio et al., 2006*). A threshold for hydroplaning by the Froude number of 0.2 (due to turbulence in the experimental setup, *Yin et al., 2018*), 0.3 (*Elverhoi et al., 2000; Yin & Rui, 2017*) or 0.4 (*Mohrig et al., 1998*) is proposed. The Froude number is the dimensionless form of the of impact velocity of the slide (*Huber, 1980*).

$$\mathrm{Fr} = \frac{u_s}{\sqrt{g * h_s}} \tag{2.1}$$

Following *Mohrig et al. (1998*), the densimetric Froude number, corrected for buoyancy of the ambient fluid, reads:

$$\mathrm{Fr_d} = \frac{u_s}{\sqrt{\left(\frac{\rho_s}{\rho_w} - 1\right) * g * h_s * \cos\alpha}} \tag{2.2}$$

u_s = slide velocity [m/s]
ρ_s = slide density [kg/m³]
ρ_w = fluid density [kg/m³]
g = gravitational constant [m/s²]
h_s = slide thickness [m]
α = slope of outflow channel [°]

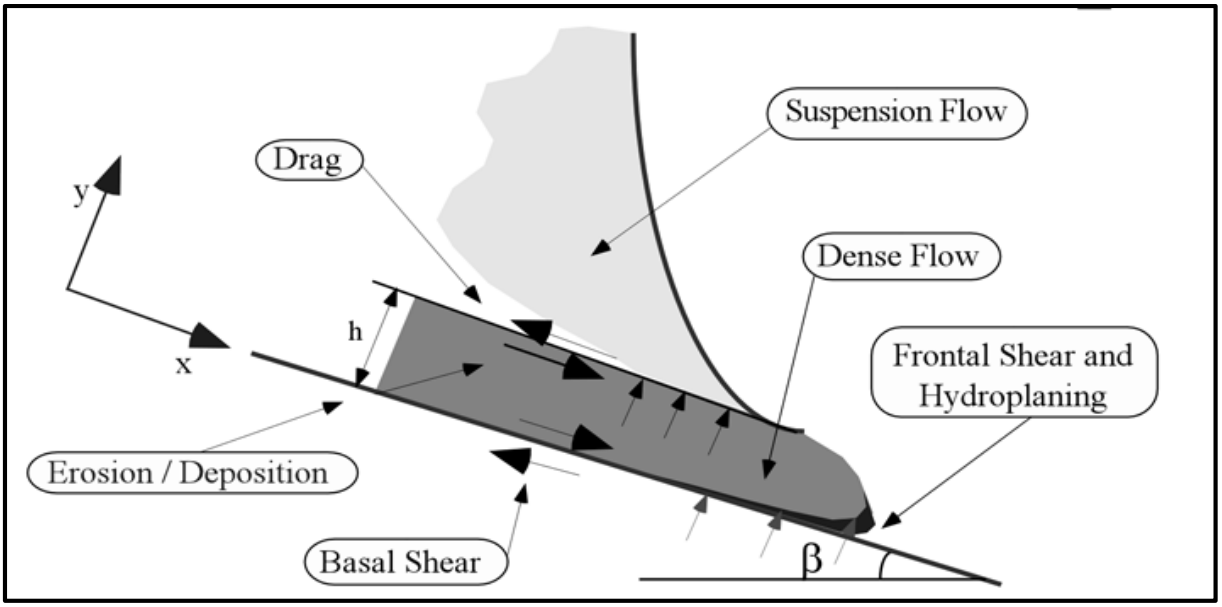

Figure 2.5. Forces and boundary conditions during a subaqueous debris flow. Note the hydroplaning at the front of the flow (*Locat & Lee, 2005*).

Regardless the different physical explanations of hydroplaning, the larger outflow length and a varying debris-flow composition will influence the debris-flow-wave interaction. Now the characteristics of as well subaerial as subaqueous debris flows are known, it is time to review their influence on the tsunami.

2.3 Debris-flow induced tsunami waves

As the subaerial debris flow enters a water basin, such as a natural or hydropower lake, two things happen. First, the debris flow continues as a subaqueous debris flow, changing its flow dynamics and inducing interaction with the water. Secondly, a tsunami wave (impulse wave), spreading in all directions (*Kafle et al., 2016*) is produced due to the transfer of momentum from the debris flow to the water (Figure 2.6). For a definition of the wave characteristics, see Figure 2.7.

No fieldwork is done to tsunami generation by debris flows due to its unpredictability. A limited amount of debris-flow scarp, tsunami run-up line, far-field tide gauge data and submarine deposits are mapped (*McFall & Fritz, 2016).*

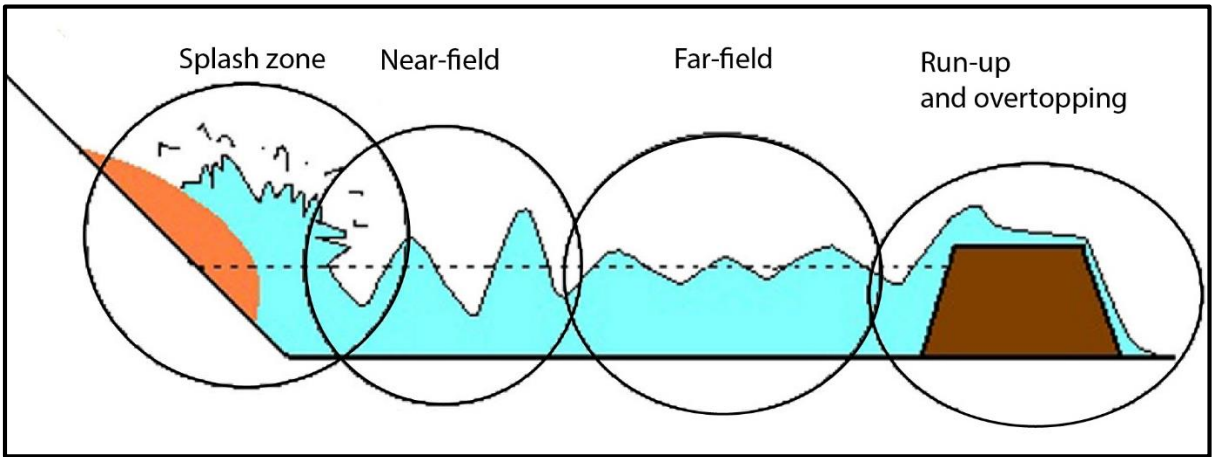

Figure 2.6. Schematic process of wave generation by a debris flow hitting the water surface (*Yavari Ramshe & Ataie-Ashtiani, 2016*).

However, wave generation recently became a subject of extensive numerical modelling, for understanding (process-based; e.g. *Mergili et al., 2017)* and hazard management purposes (*Charvet et al., 2015*). For an extensive review of computer modelling progress, I refer to *Yavari Ramshe & Ataie-Ashtiani* (*2016*). The challenge of these models is to model as well the subaerial debris flow, the subaqueous debris flow as the wave development in enough detail. Landslides are often modelled as rigid or deformable masses. The rigid assumption is used when focussed on simulation of wave propagation with Boussinesq-type-equations. If the more complicated deformable debris flow assumption is chosen, less complex equations are chosen for wave development. The results of a few multi-phase models provide relevant information for this study and are discussed below.

Pudasaini (2013) developed a two-phase debris mass-flow model, dealing with the debris flow, deposition and debris shock waves, as well generation, amplification and propagation of tsunami waves, and finally the corresponding wave run-up. They find that the generated tsunami depends on the amount of grains in the reservoir: with little sediment present, the debris flow will go faster than the wave propagation. In a dammed reservoir, this results in the debris shock wave arriving a few seconds earlier at the dam than the tsunami wave.

Kafle et al. (2016) introduced a 3D two-phase model to study the propagation of the debris flow, the wave, subaqueous debris, turbidity currents and the interactions between the subaerial and subaqueous debris and the wave. They show that modelling the deformability of the debris flow is essential to obtain the correct submergence time scale. Furthermore, the location of initiation of the subaerial debris flow is important. The exchange of momentum is both pressure driven (related to the thickness of the debris flow) and inertia driven (related to the velocity of the debris flow).

Mulligan & Take (2017) focus on the wave characteristic with a momentum-based model, letting uniform granular material travel downslope. They define the momentum flux from a landslide to the water body as the driving force behind the generation of impulse waves. They found that the maximum wave amplitude is dependent on the landslide properties (velocity, density, thickness), topography (slope) and reservoir depth. They also performed physical experiments to validate the model.

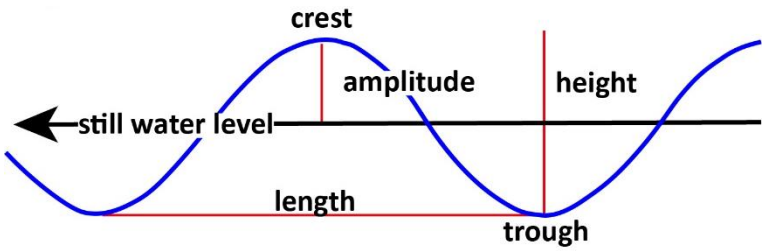

Figure 2.7. Definition of wave characteristics

The importance of confirming modelling results with laboratory experiments, is repeatedly stressed (*Pudasaini, 2013*; *Yavari Ramshe & Ataie-Ashtiani*, *2016*). The first studies (2D or 3D) were conducted with solids blocks representing debris flows (*Noda, 1970; Panizzo et al., 2005; Najafi-Jilani & Ataie-Ashtiani, 2008*; *Sælevik et al., 2009*). Researchers have opposing opinions about the influence of slide rigidity on the created impulse waves. Solid block studies overestimate the impact of the debris flow on the water by having a larger Froude number, creating a larger impact crater and unrealistically large wave heights, according to *Ataie-Ashtiani & Nik-Khah (2008*). These observations are contradicting the statement of *Heller & Spinneken (2013)* and *Ataie-Ashtiani & Najafi-Jilani (2008*) who argue block slides are relatively good representations of granular landslides, since it has a minor influence on the created near-field impulse wave.

2D experiments with granular material representing the debris flow, show that the energy transfer from landslide to wave increases when the Froude number or the rigidity of the landslide increases (*Ataie-Ashtiani & Nik-Khah, 2008*). However, the shape of the landslide seems to have a minor effect on the formed impulse wave. *Huber (1980*) notes that the Froude number has less influence on wave height at large values. He explains this by the fact that flows with a high Froude number flow faster, which means (1) the flow becomes flatter and stretches out, which spreads the impact of the momentum over a longer interval and (2) due to the higher velocity, the turbulence will increase, using part of the energy which otherwise would be transferred to the wave.

2D experiments overestimate the wave height and result in a different wave shape compared to 3D studies (*Mohammed & Fritz, 2012; Heller & Spinneken, 2015; McFall, C. & Fritz, 2016*). They have the disadvantage that the landslide is less deformed, and the spread of the wave front is unidirectional instead of radial. *Huber (1980*) notes that waves which move in the direction of the slide are the highest, the radial waves along the shore are lower. *Heller & Spinneken (2015*) compare 2D and 3D experiments with rigid blocks, and observe 4 different wave types (see below) in the 2D experiments, but only 2 different types in 3D experiments. The two observed waves are the least non-linear ones, and show a larger dispersal and smaller wave period.

3D studies with granular debris flows are described in detail below. The granular material is released on a slope from standstill (*Fritz et al., 2003a and 2003b; Mohammed & Fritz*'s*, 2012; Miller et al., 2017; McFall at al., 2018*) or first accelerated in a slide box (*McFall & Fritz, 2016*). This study does not seamlessly follow these experiments, since not only a singular granular material is used, but a multiple-phase debris flow is created with a water phase and multiple sediment types. However, the outcomes of these previous studies are still highly relevant and is summarized below.

2.3.1 Wave generation

A wave is generated at the moment the debris flow debouches into the water. As the slide penetrates the water it deforms and flow separation (water body detachment) occurs if the impact velocity is high enough (*Fritz et al., 2003a; Fritz et al., 2003b)*. The first displaced water can exceed the landslide volume by an order of magnitude (*Fritz et al., 2003a)*, and it becomes the leading wave crest, moving radially away from the debris flow (point) source (*McFall at al., 2018*). To account for the fact that only a portion of the landslide mass forms the leading wave crest, *Miller et al. (2017*) use "effective mass" in their calculations. Long and thin landslides have a smaller effective mass than thick landslides. In their experiments, long and thin landslides develop when the landslide has a long distance to accelerate before it hits the water. The wave is released (detached) when the wave celerity exceeds the decreasing subaqueous landslide velocity.

During the first impact of the debris flow into the water body, an impact crater is created which becomes the leading wave trough (*McFall & Fritz, 2016).* Secondary waves are formed if the impact crater collapses (*Fritz et al., 2003b*), which happens if the momentum transfer of the debris flow to the water is not large enough to oppose the restoring force of gravity (*Pudasaini, personal contact*). *Panizzo et al. (2015*) states that the underwater motion of the landslide is very important for wave characteristics. The head of their debris flow expands due to entrainment of water, before it deposits (*Miller et al., 2017)*.

The thickness of the landslide influences the secondary wave development: a thin landslide creates an oscillatory wave, while a thick landslide creates a dissipative bore (*Mohammed & Fritz, 2012*). The tail of the landslide is thinning while flowing into the water body, decreasing the oscillatory motion of the waves. However, *McFall et al. (2018*) explains the secondary waves by oscillations on the hillslope (run-up and rundown) caused by the primary wave.

2.3.2 Wave shape

First, it is important to define the wave types caused by the impacting landslide. *Fritz et al. (2004*) defined four different impulse wave types: weakly nonlinear oscillatory wave, non-linear transition wave, solitary-like wave and dissipative transient bore. They predict the wave type using the Froude number Fr (equation 2.1) and the relative slide thickness S (thickness divided by water level). *Heller & Hager (2011*) used the same types but a slightly different terminology: Stokes wave, cnoidal wave, solitary wave, bore wave, respectively (Figure 2.8). This terminology is used in this report. In all discussed studies, the observed wave types were non-linear. (non)Linearity is defined by the wave steepness parameter ϵ, the Ursell number U (*McFall & Fritz, 2016*) and the crest steepness (ϵ_c) (*Fritz et al.,* 2004). If ε> 0.006 or ϵ_c > 0.03 (*Dean & Dalrymple, 1991*) or when U > 1 (*Lighthill, 2001*) a wave is non-linear.

$$\epsilon = H/\lambda \quad (2.3)$$

ϵ = wave steepness parameter [-]
H = wave height [m]
λ = wavelength [m]

$$\epsilon_c = a_c / h \quad (2.4)$$

a = amplitude of crest [m]
h = still water depth [m]

$$U = a_c * \lambda^2 / h^3 \quad (2.5)$$

U = Ursell number [-]

Heller & Hager (2011) argue that with a different wave type, the fluid mass transport, run-up height and wave force significantly differ. However, wave types may change over a short distance due to energy dissipation and air detrainment. The landslide Froude number and the relative slide mass are dominant in determining the wave type caused by granular debris flows. A flow with a large Froude number and mass creates bore-type waves, smaller numbers generate in decreasing order solidary waves, cnoidal waves and stoke waves (*Heller & Hager, 2011*). The first wave crest as result of debris flow impact and penetration, develops as a solitary wave (*Mohammed & Fritz, 2012*). *Miller et al. (2017)* stress the importance of water depth (relative to landslide size) for the wave behaviour, causing in the near-field a solitary wave in deep water but a dissipative bore in shallow water. In shallow water, the waves break during generation and are the largest close to the impact zone, while the waves in deep water are long and stable, increasing in amplitude during propagation but do not break. The behaviour in the near-field influences the behaviour in the far-field, meaning that actively breaking waves do not follow the solitary wave approximation (see below). Theoretically, the breaking criterion is defined as $a_c / h = 0.78$ (*McCowan, 1894*).

2.3.3 *Wave energy*

The energy of the debris flow is partly transferred to the water body. 1-15 % of the kinetic energy of the landslide is used for wave development in *Mohammed & Fritz*'s *(2012)* experiments. The energy of the debris flow can be expressed as kinetic flow impact (equation 2.6, *Huber, 1980*).

$$E_s = 0.5 * m_s * u_s^2 \quad (2.6)$$

E_s = slide energy [J]
m_s = slide mass [kg]

The wave energy consists of potential energy (expressed by the amplitude) and kinetic energy (the orbital motion). For very small waves like capillary waves, surface tension should be included (*Fritz et al., 2004*). Assuming equipartition of the energy, wave energy is expressed as $2*E_{pw}$ (*Lamb, 1932; McFall and Fritz, 2016*).

$E_{pw} = m\ g\ h = 0.5\ w\ \rho_w\ g\ c \int_0^{\lambda} h\ dt$ (2.7)

w = width of wave basin [m]
c = wave celerity [m/s]

Decay of energy of the waves is mainly due to energy dispersion (the leading crest gives its energy to the following wave trail) and energy dissipation due to friction (*Fritz and Liu, 2002; Fritz et al., 2004*).

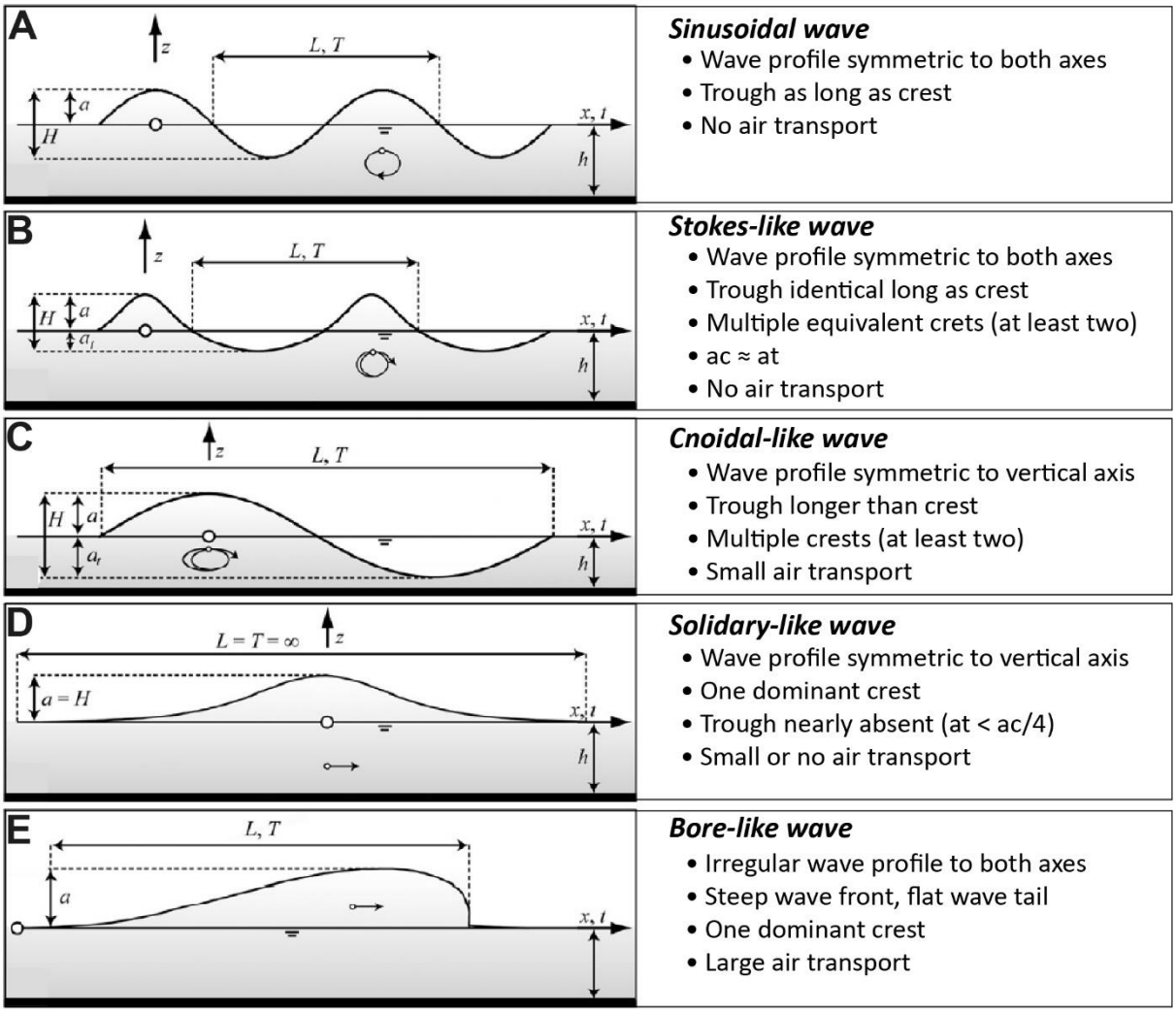

Figure 2.8. Wave profiles for different wave types and its characteristics **A)** Sinusoidal wave. **B)** Stokes wave. **C)** Cnoidal wave. **D)** Solidary wave. **E)** Bore (*Heller & Hager, 2011*).

2.3.4 Wave celerity, wavelength and wave amplitude

Celerity is generally calculated with equation 2.8a for deep water (h/L>0.5) and equation 2.8b for shallow water (h/L<0.05):

$c = gT/2\pi$ for deep water (2.8a)

T = period [s]

$c = \sqrt{gh}$ for shallow water (2.8b)

This means that in deep water the celerity of waves depends on its period, and frequency dispersion can occur. In shallow water, the celerity is only dependent on the water depth. This is an important fact, since in my experimental setup, the depth of the water body is increasing with increasing distance from the debris-flow source. In the shallow water regime (and thus near-field) the celerity of the wave crest and through differ due to the different water depth caused by its amplitude. However, *Mohammed & Fritz (2012*) find that the celerity of the leading wave is larger than the shallow water wave celerity (equation 2.8b) and can be approximated with the solidary wave approximation (*Laitone, 1960*; *Boussinesq, 1872; Fritz et al., 2004*):

$$\frac{C_{c1}}{\sqrt{gh}} = 1 + \frac{a_{c1}}{2h} \quad (2.9)$$

c_{c1} = celerity of the leading wave crest [m/s]

a_{c1} = amplitude of leading wave crest [m]

in which $a_c = H$

H = wave height [m]

The wavelength (distance between two subsequent crests) is the largest at the leading wave, and decreases for the wave train. Hence, the wave train has lower celerity than the leading wave (*Mohammed & Fritz, 2012*), following $c = \lambda / T$. Frequency dispersion occurs (*McFall & Fritz, 2016*), assuming that the smaller waves are in deep water and their energy is large enough to not have been dissipated already. The difference in celerity stretches the wave train. Due to its high celerity, the leading wave is the most important in hazard management. *Fritz et al. (2004*) notes that the subaqueous movement of the debris flow strongly influences the wavelength of the wave train.

According to *Fritz et al. (2004*), the primary wave crest is in most cases, at some point in time, the wave with the highest amplitude, but some wave types show a higher secondary wave. The maximum wave amplitude is the highest wave in a wave envelope (*Dean and Dalrymple, 1991*), which *Fritz et al. (2004*) estimate with the Froude number, slide thickness and water depth. However, the wave amplitude does not simply depend on water depth, but shows an optimum at a certain water depth for which breaking of waves just not occurs (*Miller et al., 2017)*. Conversely, *Sælevik et al. (2009)* determines debris-flow volume as the most important parameter. Furthermore, the wave amplitude of the leading wave is influenced by the material of the landslide. Cobble landslides produce higher wave amplitudes than gravel landslides, due to more efficient energy transfer caused by the high momentum of the cobble landslides (*McFall & Fritz, 2016*).

2.4 Scaling

Experiments are a great way to fully control the initial and boundary conditions, to speed up time (*Kleinhans et al., 2014*), and to make observations of normally inaccessible processes (*de Haas et al., 2016*). The degree of detail of the observations possible in experimental setups, is hardly possible in the field (*Paola et al., 2009*). Furthermore, they are necessary to verify numerical modelling by a lack of field data. This study is relatively small-scaled compared to other debris flow and impulse wave studies. This has the advantage that many systematic measurements can be done in a relatively small amount of time. On the other hand, small processes are more difficult to measure due to the relatively large instrumental accuracy compared to the measured values, and scaling can become an issue. In this section we will elaborate on the classical scaling problem, the counterapproach regarding similarity of processes, and the application of scaling in this research.

2.4.1 Traditional scaling rules

Scale effects exist because it is not possible to keep the force ratios between the model and the real world system constant. This results in deviations between the scale model and the real world system (*Heller, 2011*). The scale factor (Λ) is the ratio between the characteristic length of the real world system (L_p) and the length of the model (L_m) (*Novak & Cabelka, 1981*). The larger the scale factor, the larger the scale effects. However, a small value for Λ does not directly mean that scale effects can be ignored (*Heller, 2011*).

A model is similar to the real world if it follows the following three criteria (*Yalin, 1971; Novak, 1984*): geometric similarity (similarity in shape), kinematic similarity (similarity in motion, time, velocity) and dynamic similarity (similarity in force ratios, e.g. inertial, gravitational, viscous, surface tension). The largest problem in performing debris-flow experiments, is to keep the inertial force ratio correct. To maintain the same inertial force ratio, there must be modelled 1) in more than 1 g or 2) with a different fluid than water, characterized by a very small kinematic viscosity. *Yin et al. (2018*) choose the first option to get rid of these scaling problems and modelled in 40 g in a centrifugal setup. The most relevant force ratio selected is mostly the Froude (see equation 2.1) or Reynold number (see equation 3.11) and assume that other scale effects are negligible. Froude similarity is most often applied, especially in models where friction is negligible or in highly turbulent regimes (*Heller, 2011*). All other forces now need an individual judgement about the scaling effects. For example, the compressibility of the water will not suffer from severe scaling effects.

Iverson et al. (2010) describes two kinds of scaling which they assume to be necessary for debris-flow modelling: scaling of the flow itself and for the grain-scale mechanics. In a small experimental setup, fluid yield strength, viscous flow resistance and grain inertia are larger than in reality, while pore pressure of the fluid has a smaller effect. This leads to a dampening effect of most parameters related to fluids (*Heller, 2011*), resulting in an underestimation of that specific parameter. For *Iverson et al. (2010*), this is a reason to experiment on a very large scale, the USGS flume as described in section 2.2.2.

Other ways of dealing with scale problems, is making sure those problems are not dominating. *Heller (2011*) gives some rules of thumb and scale ratios, for which scale effects are moderate. The most relevant ones are summarized in Table 2.1. Secondly, distortion of the geometrical similarity may reduce the influence of scale effects (*Iverson, 1997*). For example, a larger vertical than horizontal scale, causes a larger water depth, increased flow velocities and a hydraulic rough regime. Third, distortion of the grain size. If the grain size is scaled down at the same factor, the sediment characteristics change significantly, changing the interactions with the fluid and sediment transport (*Heller, 2011*). Fourth, correction of the data output. It is for example known that solidary waves decay faster in the model than in real life due to boundary layer effects and fluid viscosity, or wave impacts are less due to air entrainment and impact zone boundaries (*Cuomo et al., 2010*). Finally, dimensionless parameters are used to give a general presentation of the results, since no up-scaling ratios are necessary (*Paola et al., 2009*).

phenomenon	rule of thumb	result for setup	reference
impulse wave by landslide	Re > 300.000, Wb > 5000*	h=0.60 m, 1.7 > Fr < 4.3	*Heller et al., 2008*
water wave	surface tension <1 %	T> 0.35 s, h> 0.02 m	*Hughes, 1993*
2D transformation of waves	-	scale: 1:10 - 1:50	*Hughes, 1993*
3D transformation of waves	-	scale: 1:25 - 1:75	*Hughes, 1993*

Table 2.1. Rules of thumb for which scale effects are moderate. *Re = Reynolds number, equation 3.11; We = Weber number, equation 3.14.

2.4.2 Similarity of process approach

However, the question is if it is necessary to properly follow these scaling rules. According to *Paola et al. (2009*), experiments with imperfect application of the scaling rules, compare very well with natural systems, especially in autogenic and morphodynamic systems. The self-organization in experiments creates spatial patterns and kinematics which are also observed in the field. They call this "unreasonable effectiveness", which arises due to natural scale independence of such systems. They pledge for refocusing away from traditional scaling rules, and toward causes and limits of scale independence. Furthermore, unscaled models can be a source of knowledge about scale (in)dependence. Scaled models are only necessary if the results need to be implemented directly in the field.

As described in section 2.4.1, it is impossible to apply perfect scaling, and this is also not necessary. An experiment needs to include the relevant dynamics to model the natural system. The knowledge derived from this experiments can appear to be untrue in the field, but thinking the other way around, a disproven theory in experiments will not be true in the field. For example, hydroplaning was first observed in experiments, before it became a theoretical explanation for the long outflow lengths of subaerial debris flows in the field.

Paola et al. (2009) define two terms to support this statement. Internal similarity (self-similarity), which means that a small part of a system is similar to the larger system, and external similarity, wherein a small copy of the system is similar to the larger system (*Hooke, 1968*). Internal similarity means external similarity, but this is not necessarily true the other way around. Systems which show internal similarity are showing a scale independence via their own structure. Physical experiments proved the external similarity of morphodynamic systems, also suggesting a natural scale independence. Especially systems in steady state (the topographic elevation remains constant) or autogenic systems (the morphology arises from the internal dynamics) are suitable for experiments. In these systems, the self-organized behavior arises from the fluid-sediment interaction, not from the fluid itself. The fluid is the process which makes things move, but the morphodynamic evolution happens from inside the system and is only dependent on the general properties of the fluid.

2.4.3 Scaling vision in this research

Following *Hooke & Rohrer (1979*) and *Paola et al. (2009*), small scale laboratory experiments can provide important information about the understanding of debris flows and provide quantifiable results (*Kleinhans et al., 2014*). As seen in *de Haas et al. (2016*), the debris flows in their experiments show a perfect down-scaled morphological deposit, including particle distribution and dimensions, despite the violation of scaling rules. Still, attention should be payed to the scaling effects on the wave development. Non-dimensional equations will be reviewed in an attempt to assess this.

2.5 Knowledge gap and research questions

Understanding debris-flow dynamics and the interaction with the water body is crucial for hazard management. Verification and calibration of computer models with detailed and realistic laboratory data is desired. Recent subaqueous experimental studies do include sediment composition (*Ilstad et al., 2004a; Yin & Rui, 2017*), but ignore the more realistic multi-phase composition of the debris flow, consisting of multiple grain sizes and water. The flow is oversaturated, since extra water will be taken up during the flow. Despite the finding that debris-flow composition highly influences the subaerial deposits (*de Haas et al., 2015*), no data is presented about its influence on subaqueous deposits and wave development and evolution. Therefore, there is need for more detailed analyses of the flow dynamics of multi-phase granular debris flows flowing into a water body. This novel research will focus on the debris-flow induced impulse wave rather than the deposits. The master thesis of *Santa (in progress*) will assess the subaqueous deposits.

Besides sediment composition, sediment volume (effective mass, *Miller et al., 2017*), thickness at moment of impact and channel slope are found to be important for wave generation and characteristics (see section 2.3). Therefore, the following main research question will be investigated: ***""How does tsunami wave generation and evolution depend on subaerial topography and debris-flow characteristics?"*** Debris-flow characteristics are studied by changing sediment composition (clay, gravel and water content) and sediment volume. The influence of topography is studied by changing the slope of the debris-flow channel.

The main question is divided in the following sub-questions regarding debris flow characteristics:

- (How) does the debris-flow thickness at the land-water boundary depend on the sediment composition, sediment volume and slope of the subaerial debris-flow channel?
- (How) does the debris-flow velocity depend on the debris-flow composition, sediment volume and slope of the subaerial debris-flow channel?

The following sub-questions regarding wave characteristics:

- (How) is wave amplitude, wave celerity, wavelength, wave shape and wave energy influenced by debris-flow characteristics (composition, sediment volume, debris-flow velocity and debris-flow thickness) and topographic characteristics (slope of the debris-flow channel, initial bed condition)?
- How does wave generation in the impact zone differ under different parameter values?
- To which degree are the simplified equations to predict wave characteristics, derived in previous research, applicable to this novel type of experiments?

I expect that a larger debris-flow volume and a steeper slope will cause a faster debris flow, and therefore a larger exchange of momentum causing larger waves. This larger momentum transfer is also expected by debris flows with a higher gravel content. Dilution of the debris flow will most likely lead to a faster but also thinner debris flow. The effect of thickness of the debris flow will be larger than the debris flow velocity. Therefore, a larger water content will lead to smaller but faster waves. Following de *Haas et al. (2015*), a larger clay content first mobilizes the flow up to a certain ratio. If the cohesion effect takes over, wave amplitude and the wavelength will decrease due to the higher but slower momentum transfer of the thick debris flow until the flow velocity is so low wave development barely occurs. The waves are expected to be of the non-breaking type, due to the relatively small debris-flow volumes. Following existing literature (section 2.3), higher momentum exchange will lead to solidary waves. I expect to observe a larger outflow length by subaqueous flows due to dilution of the flow head rather than hydroplaning, taking into account to the low-cohesion character of the flow. A loose bed will lead to more displacement of debris by the debris flow itself and the waves, reducing the power of the incoming debris flow by dispersing the energy. Finally, simplified formulas for wave prediction will most likely not be exactly applicable to our experiments, due to the different multi-phase composition of the debris flow, and difference in experimental setup. These hypotheses will be tested in chapters 4 and 5.

3. Methods

3.1 Methodology

A series of small scale experiments is conducted, with variations in debris-flow volume, sediment composition and outflow slope. The experimental setup of de *Haas et al. (2015)* is used, extended with a water basin at the end of the outflow channel (see section 3.2).

To account for natural variability, all experiments are done at least in twofold. In total 60 subaqueous experiments are conducted, in which the debris-flow parameters volume, water content, gravel content and clay content are studied methodically (see Table 3.1 and supplementary excel file A1.E1). A reference mixture of 8 kg (0.0042 m^3) is used as reference volume and composition for systematic variations relative to this mixture. Also, the topographic effect of a varying channel slope is studied, since this has a significant influence on runout length and flow velocity (*de Haas et al., 2015*), both being important parameters for tsunami generation. Additionally, runs are performed with a different initial bed of the outflow plane of the wave basin. Instead of a fixed (glued) coarse sand bed, an unconsolidated sand bed of 1 cm thickness is used. Finally, 38 subaerial runs are performed for comparison to the subaqueous runs and existing literature.

During each run, data is collected using video imagery, lasers, a pore-pressure device, a load cell, a shear device, a tilt device, and a 3D scanner. The corresponding data output regarding the debris-flow during subaerial outflow, includes velocity, thickness, weight, pore pressure and shear forces. Furthermore, water level measurements are recorded, from which wave height, wavelength, wave amplitude and wave celerity are subtracted. Finally, a detailed digital elevation model (DEM) of the debris-flow deposit is recorded. It is chosen to focus on the near-field wave characteristics, since in a small experimental setup like this, interference between waves and wave basin boundaries can start to play a role. An overview of the methodology can be seen in Figure 3.1.

parameter	unit	reference mixture	experimental range	nr. of subaqueous experiments	nr. of subaerial experiments
debris-flow composition					
volume (mass)	m^3 (g)	0.0042 (8000)	0.0018-0.092 (3500-18000)	22	8
water fraction	g	1846	1600-2900	8	8
	vol%	44	39.9-60.1		
	wt%	23.08	20.0-36.3		
gravel fraction	g	1107	0-3921	10	6
	vol%	18.00	0-63.7		
	wt%	13.85	0-49.0		
clay fraction	g	123	0-1784	10	6
	vol%	2.00	0-29.0		
	wt%	1.54	0-22.3		
topography					
slope	°	30	20-40	8	8
initial bed	-	fixed	fixed-unconsolidated	2	2

Table 3.1. Overview of performed experiments per studied parameter.

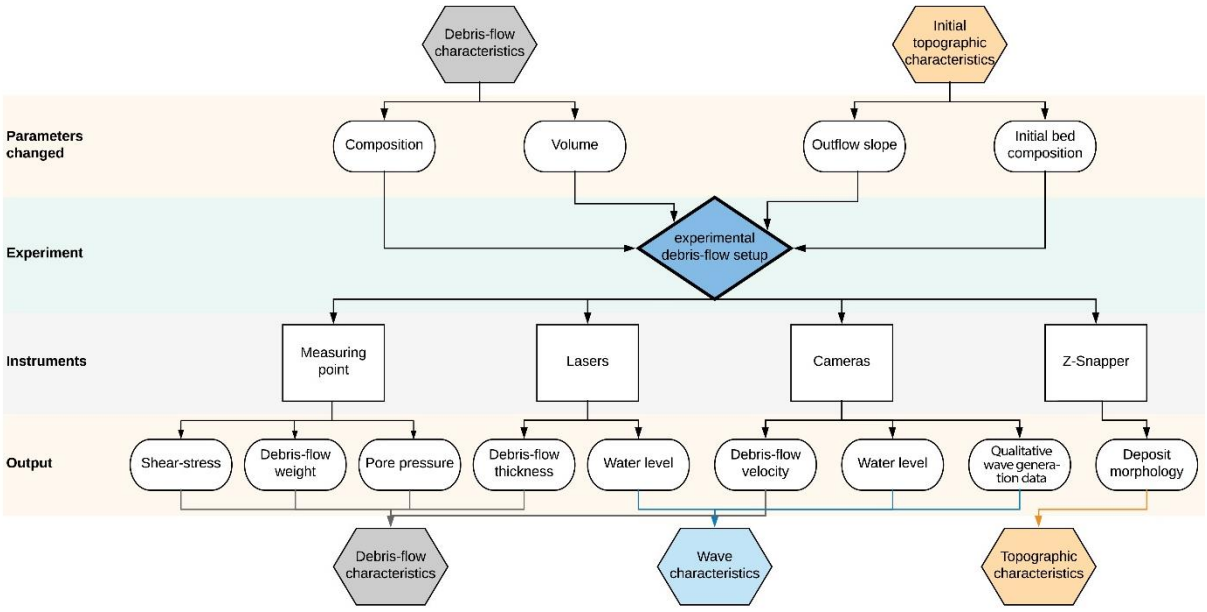

Figure 3.1. Summarizing flow chart of experimental setup and performed experiments.

3.2 Experimental setup

The experimental setup, after de *Haas et al. (2015*), consists of three sections (Figure 3.2): (1) a mixing tank to stir the sediment mixture, (2) a 2.00 m long and 12 cm wide subaerial outflow channel, inclined at α = 20-40°, (3) a 0.90 m wide and 1.85 m long wave basin inclined at θ = 10°.

The outflow channel is rectangularly shaped, and covered with sand paper to create surface roughness. Upstream of the channel a mixing tank is located, in which the sediment mixture is manually mixed for approximately 20 seconds in each experiment. When properly mixed, the sediment is released by opening the gate to the outflow channel. Simultaneously, all electronic devices (section 3.4) start recording for 30 seconds. The gate opens electromagnetically by swinging upwards, so a rapid release is guaranteed. It should be noted that an insignificant amount of water (<10 mL) could leak through the gate during mixing.

The debris flow accelerates under gravity. At the end of the outflow channel, the debris flow enters the wave basin with a constant debris-flow width. The inhibition of developing into wider debris flow is a realistic occurrence in nature, where the debris flow is often confined into a gully or depression in local topography. This means that this research is not representative for rotational slides or debris flows developing from multiple locations. The wave basin has a fixed rough surface (created by gluing coarse sand to a plate) to provide consistent basal friction. The water level of the wave basin exactly matches the height of the outflow channel. The water depth increases with increasing distance from the outflow slope, with a maximum depth of 0.33 m. The total volume of the wave basin is 0.275 m^3. The water in the basin is coloured with blue dye to enhance the visibility of the water level in video imagery.

Pumps are used to drain the wave basin after the experimental run to expose the morphology of the subaqueous debris flow deposit. The pump rate is low enough to ensure that no sediment is remobilized. Clay particles which are still in suspension will be drained as well, but this does not influence the deposit morphology (Figure 3.3E).

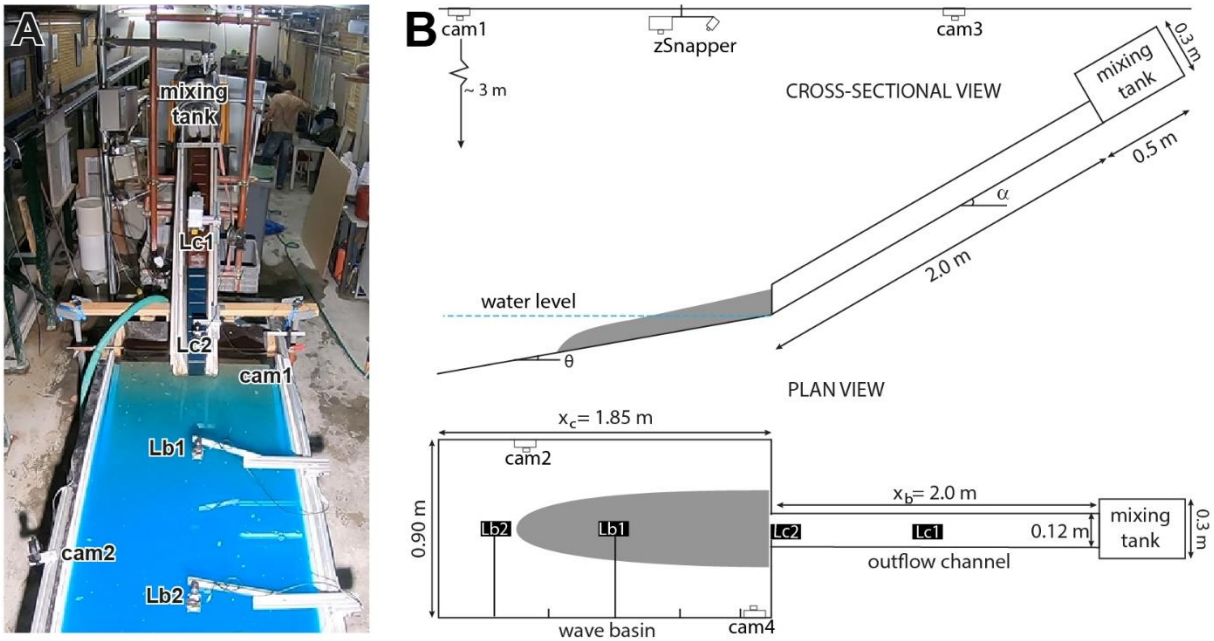

Figure 3.2. Overview of the experimental setup. **A)** photograph. **B)** schematic overview, adapted from *de Haas et al., 2015*.

3.3 Debris-flow composition

Four different types of sediment make up the debris flow: clay (kaolinite), well sorted fine sand, poorly sorted coarse sand, and basaltic gravel (2-5mm) (Figure 3.3). The characteristics of the sediments are indicated in Figure 3.4. The sediment sizes are chosen so that the clay increases the viscosity of the flow, while the gravel behaves as the coarse grained fraction in a natural debris flow (*de Haas et al., 2015*). The gravel is angularly shaped, representing recently eroded material.

The reference mixture of 8.0 kg (0.0041 m^3) consists of 13.85 wt% gravel (18.00 vol%), 45.38 wt% coarse sand (59.00 vol%), 16.15 wt% fine sand (21.00 vol%), 1.54 wt% clay (2.00 vol%) and 23.08 wt% water (0.44 vol%). Mass is converted to volume by using a constant grain density of 2,650 kg/m^3 for coarse sand, fine sand and clay, 3,400 kg/m^3 for basaltic gravel and 1,000 kg/m^3 for water. The volume percentages refer to the volume ratio of solid particles; the mass ratio includes both the solid and the liquid phase. During the experimental runs considering volume changes, the ratio of sediments is constant and similar to the reference mixture. Experimental runs with variations in water, clay or gravel fraction were kept at a constant amount of sediment (8.0 kg). By changing the water content, the volume percentages of solid particles stay the same. When changing the solid particle ratio, the volume percent of water is kept the same.

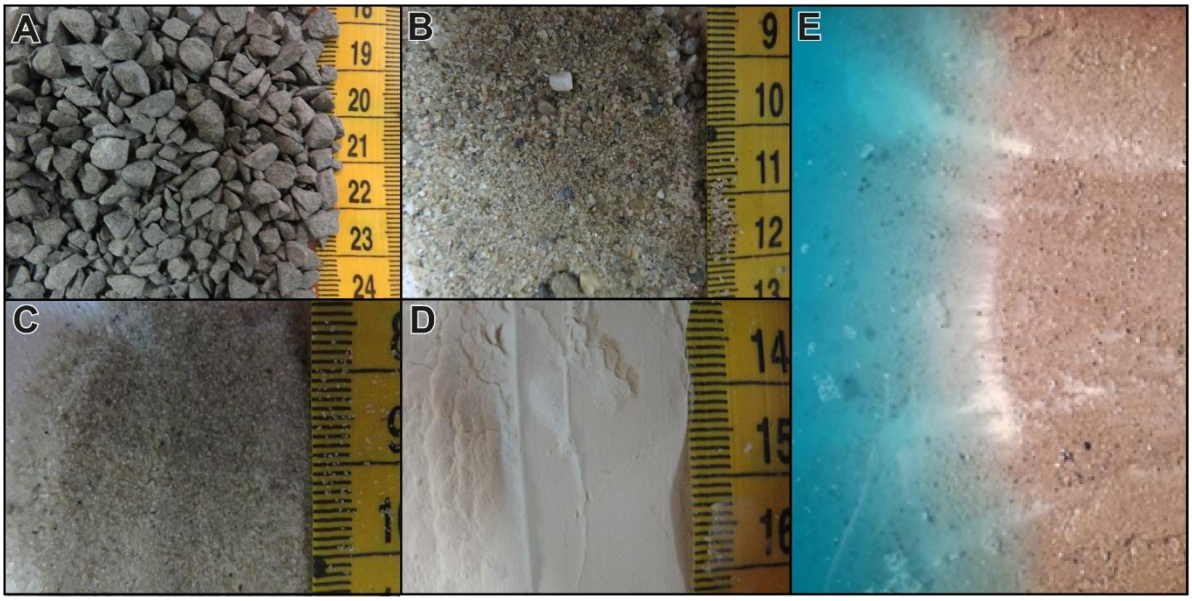

Figure 3.3. Grain sizes used in this study. **A)** Gravel. **B)** Coarse sand. **C)** Fine sand. **D)** Clay. **E)** Clay particles are remobilized during drainage of the basin.

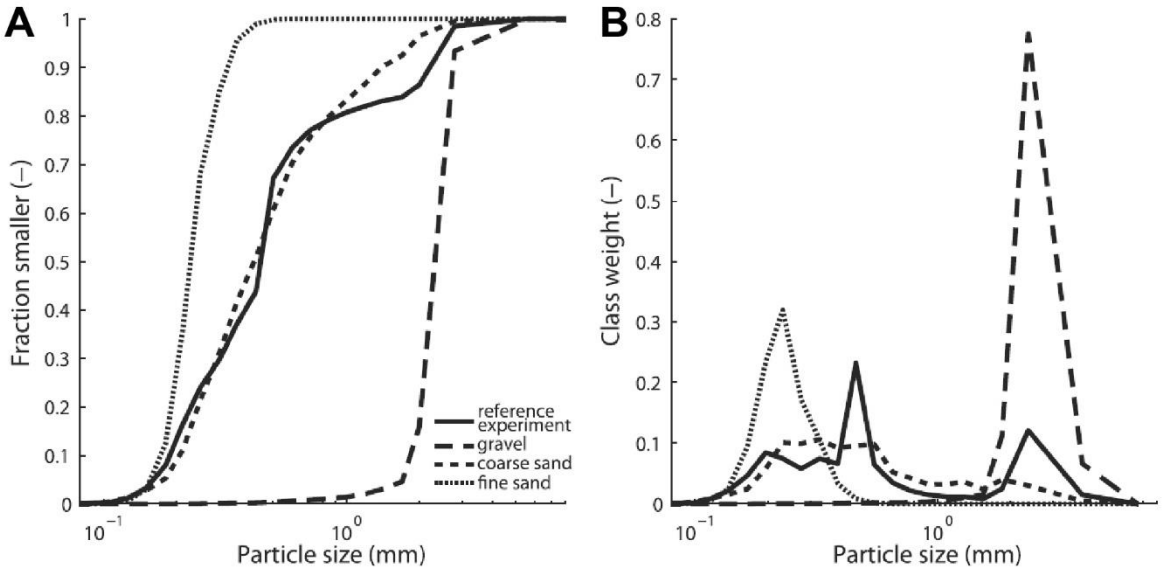

Figure 3.4. Sediment texture (*de Haas et al., 2015*). **A)** Cumulative particle distribution of the four sediment types (clay excluded) and the reference mixture. **B)** Frequency distribution of the sediment types.

3.4 Instrumentation

3.4.1 Data collection

An overview of the used instrumentation is given in Table 3.2. Cameras are used to record the debris-flow movement and the wave development (Figure 3.5A, B, C). Proper lighting on the experimental setup guarantees easy analyses of the imagery. GoPro HERO6 are used to capture a general overview of the experiment (cam1), to film the wave development from the side (cam2, x_b=1.30 m), and to record the debris flow in the outflow channel from above (cam3, x_c=1.20 m). The resolution of the cameras is set at 1440p with a frame rate of 60fps. From these imagery, wave profile (wave height over time) at 5 different locations (x_b = 0.15, 0.5, 0.85, 1.20, 1.55 m) and the debris flow velocity in the outflow channel are extracted. A GoPro HERO4 is used during experiments 3, 4, 19, 20 and ≥37, to record the impact zone and the near-field wave generation (cam4, x_b=0.05 m). It has a resolution of 1080p and a frame rate of 48fps. There is no imagery available from the subaqueous debris flow, since the inclusion of clay in the debris-flow composition, limits the visibility under water.

Two lasers, Lc1 (Baumer OADM 20U2480/S14C) and Lc2 (Baumer FADK14U4470/S14/IO) are used to measure the flow thickness at the middle (x_c = 1.20 m) and the end (x_c = 1.90 m) of the outflow channel. Furthermore, two laser scanners, Lb1 and Lb2 (Baumer FADK14U4470/S14/IO) are used to measure the water movement at x_b = 0.85 m and x_b = 1.55 m in the middle of the wave basin, from which wave evolution can be interpreted. This data can be used additionally to the wave data obtained by the camera. The frequency of both lasers is 100 Hz.

Debris-flow weight, pore pressure and shear forces are measured at a measuring point in the middle of the outflow channel (x_c = 1.20 m) and recorded with a frequency of 100 Hz. The pore-pressure and shear devices did not seem to function satisfactory in these experiments, and additional research should be done to obtain satisfactory data collection at such small scale.

The deposit morphology is measured by a Vialux z-Snapper 3-D scanner, which creates a point cloud from a fringe pattern projector and camera (vertical and horizontal on submillimetre scale) (*Hoefling, 2004; de Haas et al., 2015*). MATLAB (*the Mathworks, version R2017a*) is used to interpolate this point cloud into a gridded DEM (1 mm resolution). To determine the net deposition, the DEM of the initial bed is extracted from the DEM of the deposited debris flow, after draining the water basin (Figure 3.5D). Deposition of the debris flow tail caused by the continuous slow outflow of rest material in the outflow channel, could be interpreted as a next surge on the DEM.

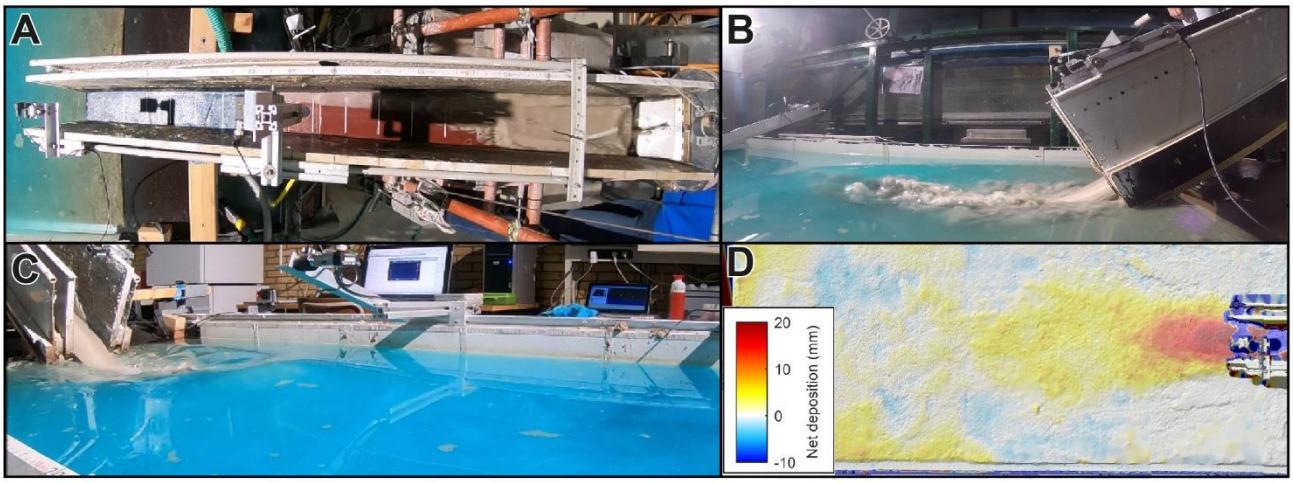

Figure 3.5. Raw output from cameras. **A)** above the outflow channel, cam3. **B)** where the outflow channel enters the basin cam4. **C)** at the side of the wave basin, cam2. **D)** the DEM of a run performed with the reference mixture.

name	device	where	function
Cam1	Camera	Above the basin x_b>2.00 m	Overview of experiments
Cam2	Camera	Side of basin x_b=1.30 m	Water level fluctuations at x_b = 0.15, 0.5, 0.85, 1.20, 1.55 m
Cam3	Camera	Above outflow channel x_c=1.20 m	subaerial debris-flow velocity
Cam4	Camera	Impact zone x_b=0.05 m	Near-field wave generation
Lc1	Laser	Above outflow channel x_c=1.20 m	Debris-flow thickness
Lc2	Laser	Above outflow channel x_c=1.90 m	Debris-flow thickness
Lb1	Laser	Above wave basin x_b=0.85 m	Water level fluctuations
Lb2	Laser	Above wave basin x_b=1.55 m	Water level fluctuations
Wt	Load cell	Above outflow channel x_c=1.20 m	Debris-flow weight in outflow channel
Tilt	Tilt device	Above outflow channel x_c=1.20 m	Exact tilt of outflow channel
zSnapper	3D scanner	Above setup along x_b	Morphology of deposits
-	Pore pressure, shear	Above outflow channel x_c=1.20 m	Did not function

Table 3.2. Overview of instrumentation.

3.4.1 Accuracy

Three factors are influencing the accuracy of the obtained data. First, accuracy influenced by manual labour. Secondly, instrumentation accuracy and finally the limitations of the electrical acquisition (Table 3.3).

(1) The movement of mixing causes the channel slope to vibrate, which in turn leads to the development of small ripples in the water, moving radially away from the channel slope. Those ripples are in the order of <1mm. The vibration of the channel slope will also influence the weight and shear device. Due to the fact that these devices are turned on at the moment of release of the debris flow, the vibration is not recorded and will not influences the measurements significantly. The same is true for all lasers. Laser Lb1 and Lb2 are mounted on a long arm attached to the experimental setup. Possible vibrations of the wave basin during recording therefore influence the measurements slightly. Finally, the moment of release of the debris flow is defined manually. The debris is released directly after the mixing stopped, which has a delay of approximately <1 s.

(2) Having a small setup means having small forces and movements, which are harder to measure than in a bigger setup. This causes limitations to the types of instruments and their accuracy. Laser Lc1 has the highest resolution, with a submillimetre accuracy. The resolution of the other three lasers is also <1 mm. The lasers are placed so that they are in the lower limit of the devices' reach, increasing the accuracy. The influence of temperature change on the lasers' accuracy is negligible. The weight, shear and pore pressure device are all developed for larger forces than exerted in this setup. The recorded values are in the lower limits of the devices' reach and sometimes even in their range of accuracy itself. Therefore, pore pressure and shear are excluded from data analysis. Nevertheless, the load cell seems to function quite well for small values, and will be used with care in the analysis. The used cameras have a resolution of 1440 p (cam1-3) and 1080 p (cam4) and a frame rate of 60 fps (cam1-3) and 48 fps (cam4), respectively. The temporal resolution is therefore limited by the frame rate of one frame per 0.0167-0.0208 s. The spatial resolution is limited by the pixel size, varying between 1.3-1.9 mm.

(3) The electrical acquisition used for the lasers has an accuracy of 16 bits, giving a resolution of 0.305mV. Depending on the span of the laser and the size of the recorded features, the accuracy of the electrical acquisition or the accuracy of the laser is the limiting accuracy.

It is however not necessary to elaborate on this, since the accuracy of the manual setup itself falls far outside this range. Therefore, it can be said that the accuracy of all instruments will be influenced most by the fact that it is manual labour. Small data values (in the order of mm and g) therefore will be handled with care in the analysis.

		accuracy device			accuracy electrical acquisition		
device	**instrument**	**span**	**resolution**	**unit**	**range channel [V]**	**res channel [mV]**	**instrument output [V]**
Lb1	OADM_01	100 - 600	0.015 - 0.67	mm	-10 - 10	0.305175781	0 - 10
Lb2	FADK_01	50 - 400	0.1 - 1	mm	-10 - 10	0.305175781	0 - 10
Lc1	FADK_02	50 - 400	0.1 - 1	mm	-10 - 10	0.305175781	0 - 10
Lc2	FADK_03	50 - 400	0.1 - 1	mm	-10 - 10	0.305175781	0 - 10
Load cell		0 - 3	± 0.003	kg	-10 - 10	0.305175781	0 - 5
Tilt		-67 - 67	± 0.2	°	-5 - 5	0.152587891	0 - 5
Shear		0 - 26.8	± 0.5	N	-5 - 5	0.152587891	0 - 5
Pore pressure		-83 - 83	0.05	mBar	-5 - 5	0.152587891	0 - 5

Table 3.3. Accuracy of used electronic devices (excluded z-Snapper and cameras).

3.5 Data analysis

Data analysis is performed in MATLAB (*the Mathworks, version R2017a*). First, quality control and pre-processing of the data is done, to remove obvious measurement errors. Secondly, data is extracted from video imagery. Finally, the resulting datasets are analysed to find possible correlations between the debris-flow and wave characteristics.

3.5.1 Quality control and pre-processing

The velocity of the debris flow in the outflow channel is derived from video imagery from cam3. By analysing each image from the video, the exact time of arrival of the debris-flow front at the locations x_c = 0, 50, 100, 150 and 200 cm is determined, from which the average velocity between these points can be calculated. The debris flow will have a non-linear velocity profile due to internal shearing, leading to a higher velocity of the top surface than the mean velocity (*Bryant et al., 2015; Miller et al., 2017*). The debris flow moves down as a coherent mass, and the method used in this research results in observation of the velocity of the front propagation. This is the highest velocity of the debris flow, which is also the most relevant for hazard management.

Wave data is extracted from video imagery from cam2 at 5 different locations (Figure 3.6). The blue dye in the water of the wave basin assures easy observation of the exact location of the water level. Based on intensity differences and a certain threshold to distinguish between water and no water, a water level profile can be created, from which wave characteristic can be interpreted. Next, erroneous high or low values are removed by setting a maximum wave amplitude expected. Finally, the analysis is stopped after 8 seconds due to clay dispersal. Clay particles getting suspended in the water, influence the colour of the water by turning it white. The contrast between the water and the background is not clear enough anymore to obtain reliable data. This is however not a problem, since at this time wave dispersal is already in such a far state that only reflection and refraction at the sides of the wave basin are measured. The first crest amplitude (a_{c1}) is determined as the first significant

peak upward, ignoring noise from the movement of the mixing tank. The first trough amplitude (a_{t1}) is determined as the first significant peak downward, lower than the still water level. The analysis is limited by the pixel size of the GoPro (~ 1.5 mm), which makes it not possible to study very small capillary impulse waves. The method does, however, effectively remove the unwanted water fluctuations due to mixing from the dataset.

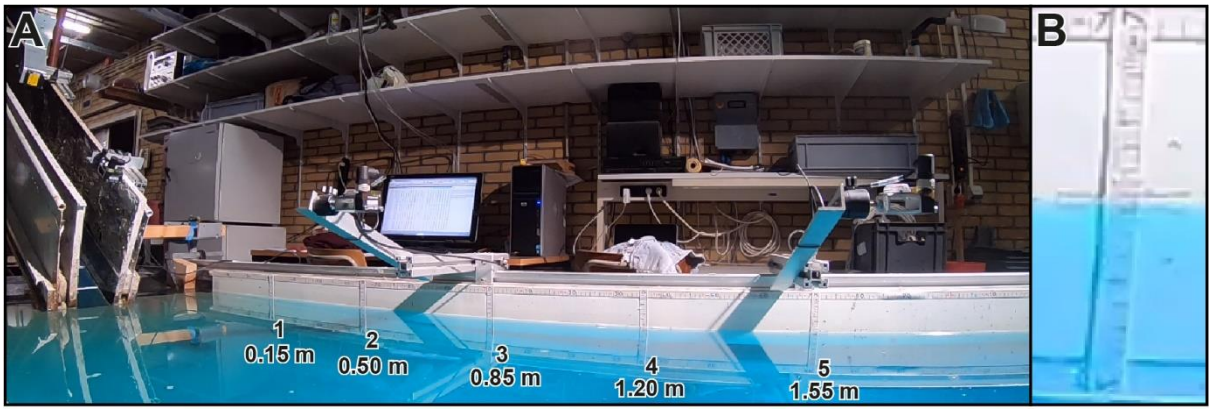

Figure 3.6. Explanation of setup for water level measurements. **A)** The 5 measuring points for water level in in wave basin by cam2, at x_b = 0.15, 0.50, 0.85, 1.20 and 1.55 m. **B)** Enlargement of scale bar on side of wave basin, showing the current water level, used for analyses of video imagery analyses of cam2.

Additional to the wave data from cam2, wave data from Lb1 and Lb2 is extracted. First, the laser data is converted from volt to meters. Next, a maximum wave amplitude is set to account for errors wherein the laser measured the surface instead of the water level. Finally, the initial water level is set at 0 m. The debris-flow thickness derived from Lc1 and Lc2 is slightly adjusted by taking a median filter (the median of 100 measurements) to smoothen the curve and remove erroneous values. However, when comparing laser data to visual observations, the measured wave height is unrealistically large. Furthermore, the wave profiles show a lot of scatter and peaks (appendix A3, Figure A3.1) if the wave heights become larger than 10 mm. The most likely explanation for this, is the reflection of the laser beam on the water surface being under an angle due to the steepness of the wave shape. Therefore, the signal is not reflected (correctly) to the receiver. Consequently, the laser data is not used for analysis and further study will only include the camera data.

The measured values from the weight cell are converted from volt to grams and correction for flume inclination is applied. A correction is done to make the data series start at 0 gram. Debris-flow thickness and weight are used to calculate the flow density. However, the load cell operates at the lower limits or even within the accuracy of its span. The discrepancy between flow weight and flow thickness therefore cause erroneous values of the flow density (Appendix A3, Figure A3.2). I chose to use the theoretical values of flow density by dividing its total mass by its total volume. Its porosity is insignificantly small since all pore space is filled up by water.

3.5.2 Dimensional calculations

The pre-processed data of water level over time, is used to calculate various characterizing wave parameters.

Wave celerity is estimated from the arrival time difference of the first crest or trough at five locations. The travel distance to this measurement location is not simply its x_b-position, but is corrected for the radial wave propagation (Figure 3.7). Celerity is calculated between location x_b = 0-0.50 m, 0.50-0.85 m, 0.85-1.20 m, 1.20-1.55 m and 0-1.55 m.

$$c = \frac{\sqrt{\left(\frac{1}{2}w^2\right) * \Delta x_b^2}}{\Delta t} \tag{3.1}$$

x_b = location along the wave basin [m]
t = time [s]

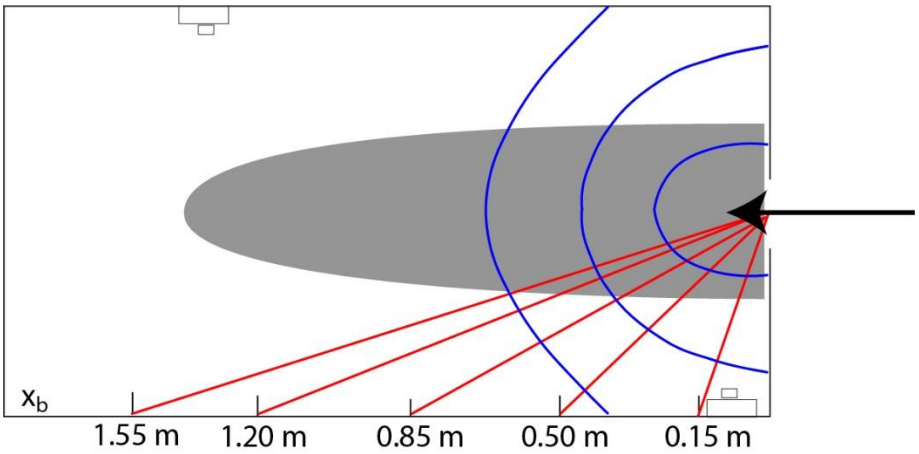

Figure 3.7. Travel distance of wave till the measuring location.

The wave period is calculated in two different ways. The symmetry method assumes wave symmetry, and takes two times the time between the first crest and the first trough as wave period. The peak method takes the time between the maximum peak and the subsequent peak. Due to the irregular waves patterns in different experiments and the difference in wave shape and behavior between the first and following waves, there is no preferable method.

To calculate wavelength, the celerity between the last and current location is multiplied by the period at that location ($\lambda = c * T$). The wavelength is used to calculate the regime (shallow, intermediate or deep water), which determines which general formulas are applicable for calculations and predictions. The regime is calculated with h/L, which will be smaller than 0.05 for shallow water and larger than 0.5 for deep water. The breaking criterion (A_c / h = 0.78) is used to determine if waves could theoretically break in this setup.

The detachment time, or effective time (t_{eff}), is the time to which the debris flow stops "pushing" the wave, and the wave becomes detached from the debris flow. At this moment, the debris-flow velocity will be smaller than the wave celerity. The detachment time is determined via visual inspection of the video imagery of cam2. Visual observation is prone to interpretation, and the values of detachment time should be handled with care.

Momentum is defined as effective mass times velocity (M = m * u [kg*m/s = Ns]). Debris-flow momentum is calculated in the following way. First, the effective mass is determined (following *Miller et al., 2017*) which is the weight flowing into the wave basin during the detachment time. This is done by determining the integral of the weight measured at the load cell from t_0 till t_{eff}, and multiplying this by the travelled distance (velocity * time) during this time. The obtained value is corrected for area of the weight cell. Next, this effective weight in the middle of the outflow slope, is converted to the effective weight at the outlet by assuming a constant ratio between weight and debris-flow thickness in the middle and at the outlet. Finally, the momentum is calculated, in which the debris-flow velocity is corrected for flume inclination.

$$M = m_{eff} * u_s * \cos(\alpha) \quad (3.2)$$

$$m_{eff} = \int_{t_0}^{t_{eff}} m \, dt * (u_s * t_{eff}) * (w / A_{cell}) * (h_{s\ outlet} / h_{s\ middle}) \quad (3.3)$$

M = momentum [Ns]
u_s = slide velocity [m/s]
α = slope of outflow channel [°]
m_{eff} = effective mass [kg]
t_{eff} = effective time [s]
w = width of outflow slope [m]
A_{cell} = area of load cell [m^2]
h_s = thickness of debris flow [m]

Energy is calculated with equations 2.6 and 2.7 for the debris flow and the leading crest, respectively. To calculated debris-flow energy, the average slide velocity and the effective weight are taken. To calculate the wave energy of the leading crest, the near-field wave data of x_b = 0.50 m is used. The volume of the wave is calculated by taking the integral of the water level during the first crest and multiplying this by travel distance (wave celerity times time of the leading crest) and the width of the wave. It is assumed that the width of the radial wave is approximately similar to 0.5 times the circumference of a perfect circle with a radius of 0.5 m.

Possible relations or (non)linear regression will be evaluated using descriptive statistics, and will be tested for statistical significance with the R^2- and p-value (*Motulsky & Ransnas, 1987*). The R^2-value, between 0 and 1, indicates whether the two variables are correlated, and the number shows which part of the variation can be explained by the regression. An R^2-value of 0.55 is chosen as threshold for correlation. This is lower than most literature suggest, however physical experiments are generally prone to a lot of scatter due to natural variability and the relatively small sample size (2 x 30 experiments). Therefore, a relatively low R^2-value can still show a correlation of statistical significance. The p-value, or significance level, shows the strength of the evidence against the null hypothesis. The smaller the p-value, the stronger the evidence against the null hypothesis (*Sterne & Smidth, 2001*). In this research, a confidence level of 95 % is chosen, meaning that the p-value should be smaller than 0.05.

3.5.3 Non-dimensional calculations

Dimensionless parameters make it possible to compare different sized experiments to each other. The dimensionless parameters used in this research are shown in Table 3.4, and are in more depth described in *Iverson, (1997)* and *de Haas et al. (2015)*.

dimensionless parameter	representing ratio	equation		symbols
Bagnold number	collisional forces / viscous forces	$Bg = \frac{v_s \rho_g \delta \gamma}{(1-v_s)\mu}$	3.4	δ = mean grain size of debris flow [m] γ = flow shear rate [1/s] μ =interstitial fluid viscosity [Pa s] (values taken from de *Haas et al. 2015*) v_s = volumetric solid fraction [-] u_s = debris-flow velocity [m/s] h_s = debris-flow thickness [m] h = still water depth [m] ρ_g = density of solids [kg/m³] ϕ = internal angle of friction [°] (assumed 42°, *Parson et al., 2001*) k = permeability [m²] L = maximum length of flow mass [m], which is assumed to be equal to the outflow slope λ = wavelength [m] u_w = orbital velocity [m/s] (estimated 0.1m/s, *Wiberg & Sherwood, 2008*) σ = surface tension coefficient [N/m] (0.07 N/m for water at T = 293 K)
		$\gamma = \frac{u_s}{h_s}$	3.5	
Savage number	collisional forces / frictional forces	$Sv = \frac{\rho_g \delta^2 \gamma}{(\rho_g - \rho) g h_s \tan(\varphi)}$	3.6	
friction number	frictional forces / viscous forces	$Fn = \frac{v_s (\rho_g - \rho) g h_s \tan\varphi}{(1-v_s)\gamma \mu}$	3.7	
Mass number	solid inertia / fluid inertia	$Mn = \frac{v_s \rho_g}{(1-v_s)\rho}$	3.8	
Darcy number	tendency for pore fluid pressure to buffer grain interactions	$Dc = \frac{\mu}{v_s \rho_s \gamma k}$	3.9	
grain Reynolds number	ratio of the effect of particle collision and pore fluid viscosity	$Re_g = \frac{Bg}{Mn} = \frac{\rho \gamma \delta^2}{\mu}$	3.10	
Reynolds number	the influence of viscous effects relative to the size of the flow in a down-scaled setup	$Re = \frac{\rho_s h_s \sqrt{g L}}{\mu}$	3.11	
slide Froude number	dimensionless form of the of impact velocity of the slide	$Fr = \frac{u_s}{\sqrt{g * h_s}}$	3.12	
densimetric Froude number	landslide velocity / wave celerity	$Fr = \frac{u_s}{\sqrt{g * h}}$	3.13	
Weber number	inertial force / surface tension	$Wb = \frac{\rho u_w^2 \lambda}{\sigma}$	3.14	

Table 3.4. Dimensionless parameters representing various force balances within the debris flow.

4. Results and interpretation

The raw debris-flow and wave height data can be found in supplementary excel files A1.E2 and A1.E3. First, I will shortly point out the natural variability dealt with in this research (4.1). Then in the next sections, I will elaborate on the debris-flow characteristics (4.2), the wave characteristics (4.3) and the relation between those two (4.4). In these sections, first a general description and statistics are given, followed by a more in depth analysis on the influence of the tested variables on the debris-flow and/or wave features.

4.1 Natural variability

All experiments are done in twofold to account for natural variability. Figure 4.1 shows the natural variability of the experiments, by plotting the two similar experiments against each other. It is clear that both the debris-flow characteristics (R^2 = 0.30 - 0.79) and wave parameter values (R^2 = 0.49 - 0.77) show a significant amount of variability, although >98 % of the data points fall within the 1:2 lines. This gives an indication for the expected variability within the data. The values averaged over distance (e.g. average debris-flow velocity or average crest or trough celerity, R^2 = 0.79, 0.70, 0.77, respectively) show much less variability. It is therefore preferred to use the space-averaged data.

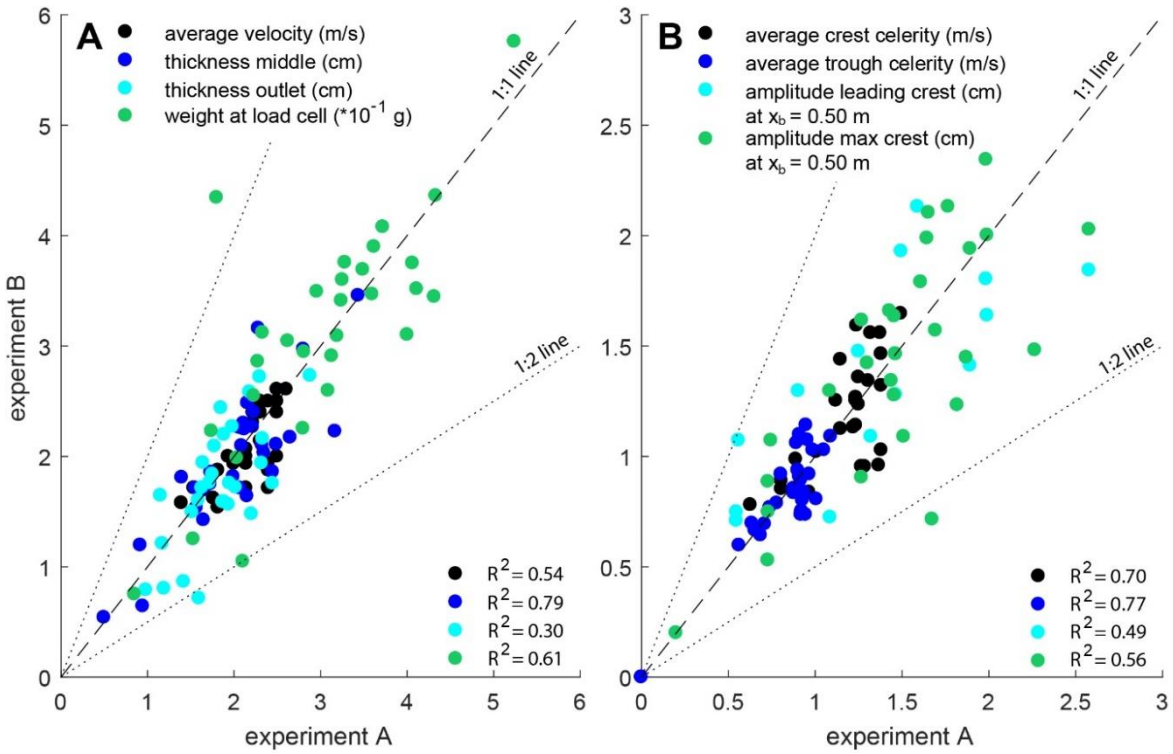

Figure 4.1. Natural variability of **A)** debris flows and **B)** the corresponding impulse waves. The numbers on the axis correspond with the actual value of the plotted variables.

4.2 Debris flow

Variations in debris-flow volume, composition, and the slope of the outflow channel influence the debris-flow thickness, weight and velocity. An example of the thickness and weight profile of a debris flow moving downslope, is shown in Figure 4.2. In approximately 1.5 seconds the whole debris flow passed by the measuring point, with its optimum in the first 0.5 seconds. A certain amount of material stays behind forming the tail of the graph. The thickness optimum and the weight optimum in the measuring point coincide, and the two variables are linearly related (R^2 = 0.66 and 0.67, p = $7.0*10^{-15}$ and $2.4*10^{-15}$ for middle and outlet thickness, respectively; Figure 4.3A). The correlation between thickness and weight shows that the less reliable weight data can still be used. The thickness of the debris flow is on average larger in the middle than at the outlet (2.04 cm and 1.81 cm, respectively), presumably due to the time needed for the debris flow to spread out.

The debris-flow velocity over the whole outflow slope (2.0 m) is on average 2.12m/s with a standard deviation (std) of 0.32. In the first 0.50 m of the slope the debris flow shows a highly variable velocity in between the runs (average 2.34 m/s, std 0.59), presumably due to the manual labour of mixing before release of the debris flow. In next 50 cm (50-100 cm) the velocity is consequent lower than average (1.75 m/s, std 0.32). The velocities in the last 100 cm of the outflow slope are more comparable to the average velocity, although the variability is larger (average 2.38 m/s, std 0.49). The relation between flow thickness and flow velocity shows too much scatter to draw a statistical significant relation, although one could recognize a counterintuitive increase in thickness with an increase in velocity (Figure 4.3B).

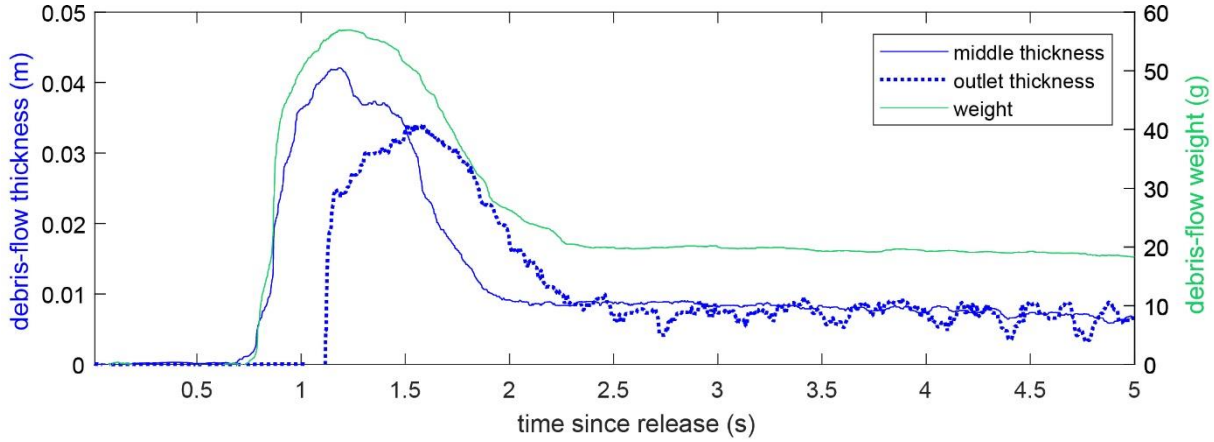

Figure 4.2. Example of a profile of debris-flow thickness and weight (exp022).

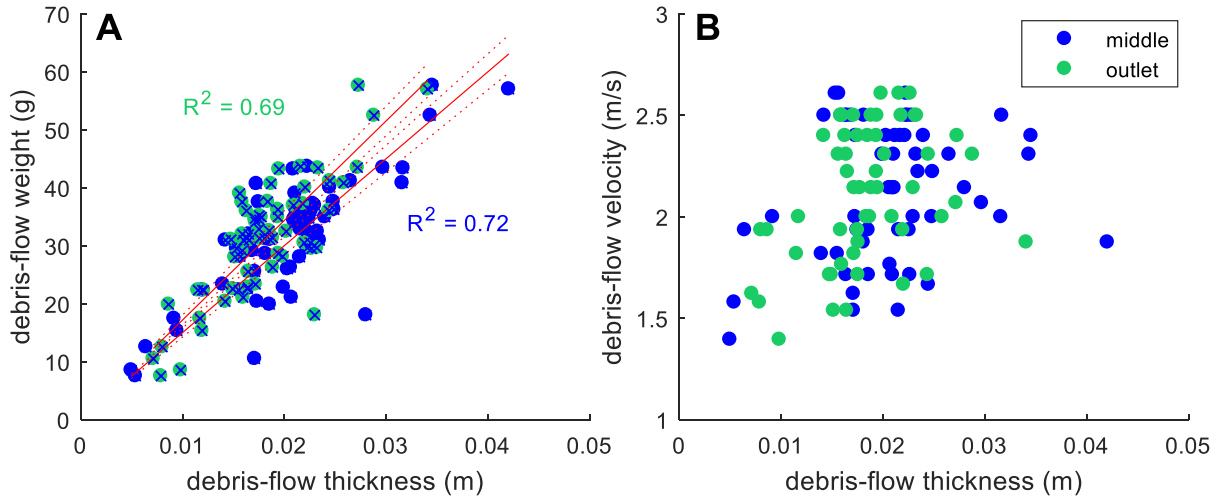

Figure 4.3. The relation between middle and outlet debris flow thickness against: **A)** flow weight, linear trend line forced through 0.0. **B)** flow velocity.

4.2.1 Debris-flow volume

The fixed width of the outflow slope limits the dimensions of the debris flow, and with an increasing volume both thickness and velocity will increase (Figure 4.4). Especially in the middle, where the flow is less spread out, those two parameters are highly related (R^2 = 0.93). Hence, the maximum weight follows a similar lineair regression (R^2 = 0.70). Debris-flow velocity increases with increasing mass, but this relation shows a lot of scatter (R^2 = 0.44).

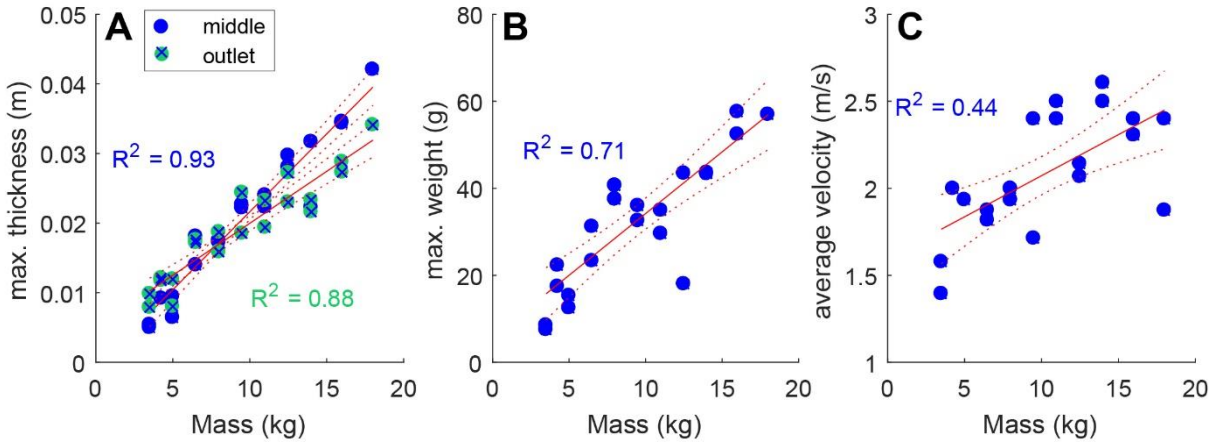

Figure 4.4. Relation between mass and debris-flow characteristics. **A)** maximum thickness in middle and outlet. **B)** maximum weight at load cell. **C)** average debris flow velocity. The P-values of the linear regression lines are 2.65 * 10^{-3}, 5.12 * 10^{-11}, 2.65 * 10^{-3} and 7.75 * 10^{-4}, respectively

4.2.2 Debris-flow composition

With an increasing water content (Figure 4.5A, B, C) the average velocity of the debris flow increases (R^2 = 0.90). Counterintuitive, the maximum thickness also increases with water content (R^2 = 0.56). Weight does not seem to have a significant relation with water content, despite the decrease in theoretical density of the flow.

An increasing gravel content (Figure 4.5D, E, F) does not show any relation with the measured debris flow characteristics.

An increase in clay content (Figure 4.5G, H, I) leads to a decrease in debris flow weight (R^2 = 0.69). The relation with thickness and velocity is however a bit more complex. An increase in clay content has a lubricating effect, resulting in a larger flow velocity. However, when the clay content becomes larger than 21 vol%, the flow becomes very viscous and the velocity decreases. The same effect is visible in debris-flow thickness in the middle of the outflow slope. However, the outflow thickness is not influenced by this.

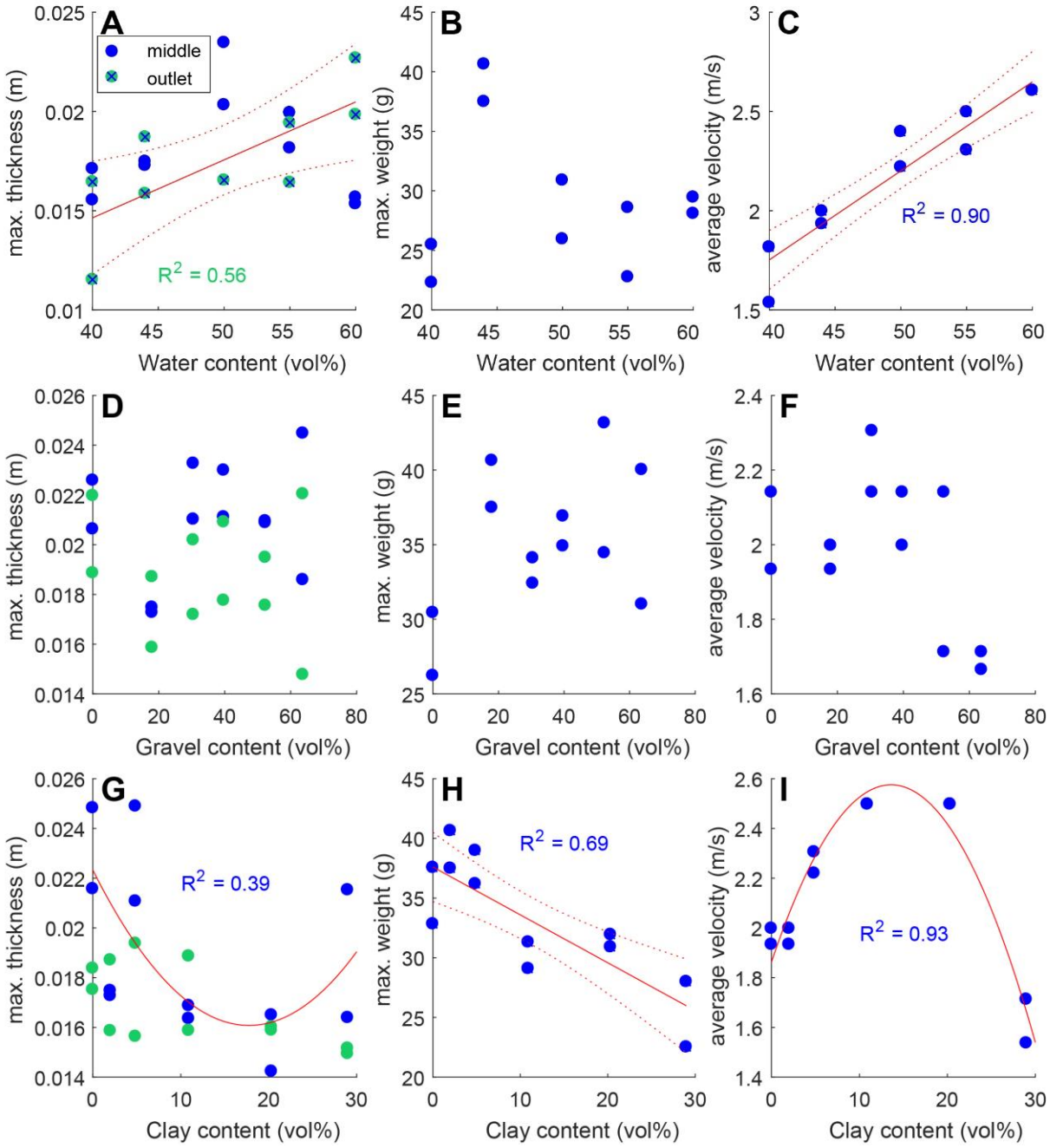

Figure 4.5. Relation between debris-flow composition and debris-flow characteristics. **A), B), C)** water content. **D), E), F)** gravel. **G), H), I)** clay. The P-values of the linear regression lines are A: p = 0.02, C: p = $2.91*10^{-5}$. H: p = $8.35* 10^{-4}$.

4.2.3 Outflow slope

With an increasing slope, debris-flow thickness, weight and velocity increase (Figure 4.6). This relation is the strongest for debris flow weight (R = 0.72) and outflow thickness (R = 0.65). The other two relations are not significant (R<0.5, P>0.05).

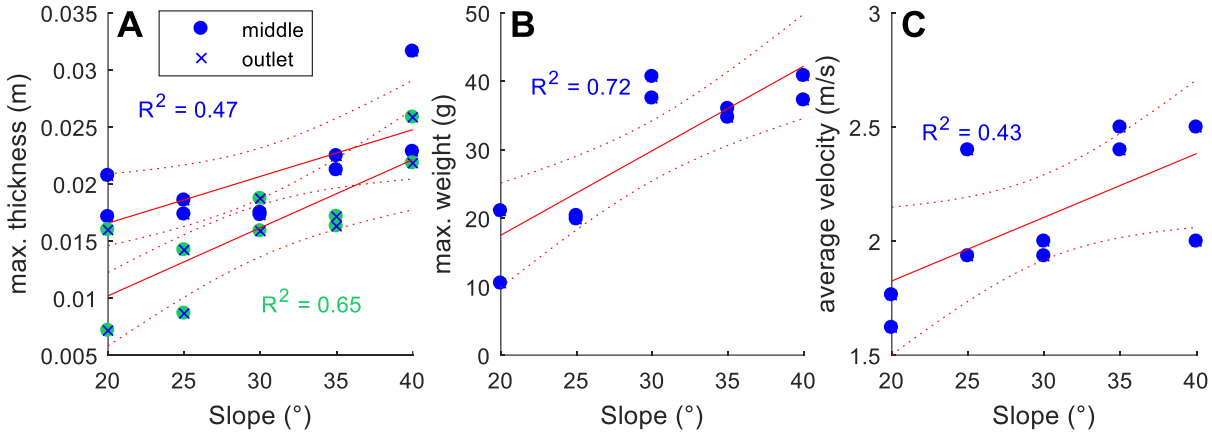

Figure 4.6. Relation between outflow slope and debris-flow characteristics. **A)** Maximum thickness in middle and outlet. **B)** maximum weight at load cell. **C)** average debris flow velocity. The P-values of the linear regression lines are 0.028, $4.98 * 10^{-3}$, $1.82 * 10^{-3}$, 0.041, respectively.

4.2.4 Debris-flow energy and momentum

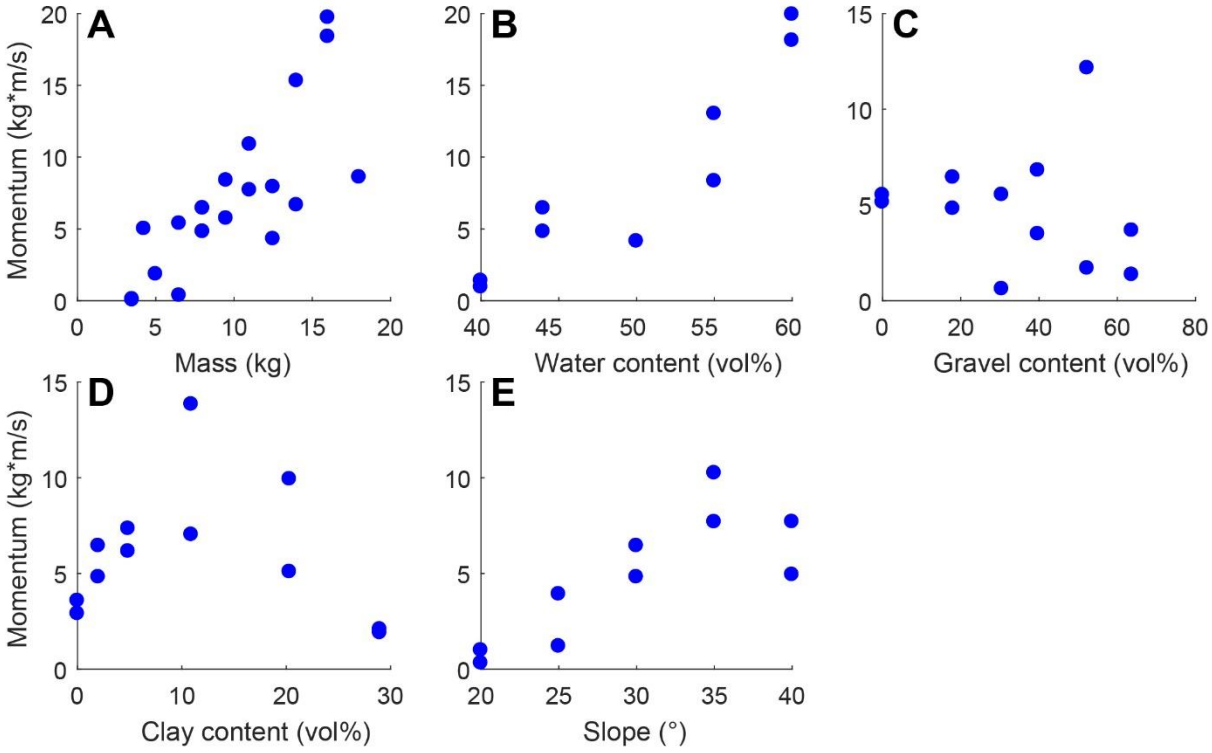

Figure 4.7. Debris-flow momentum per varied parameter.

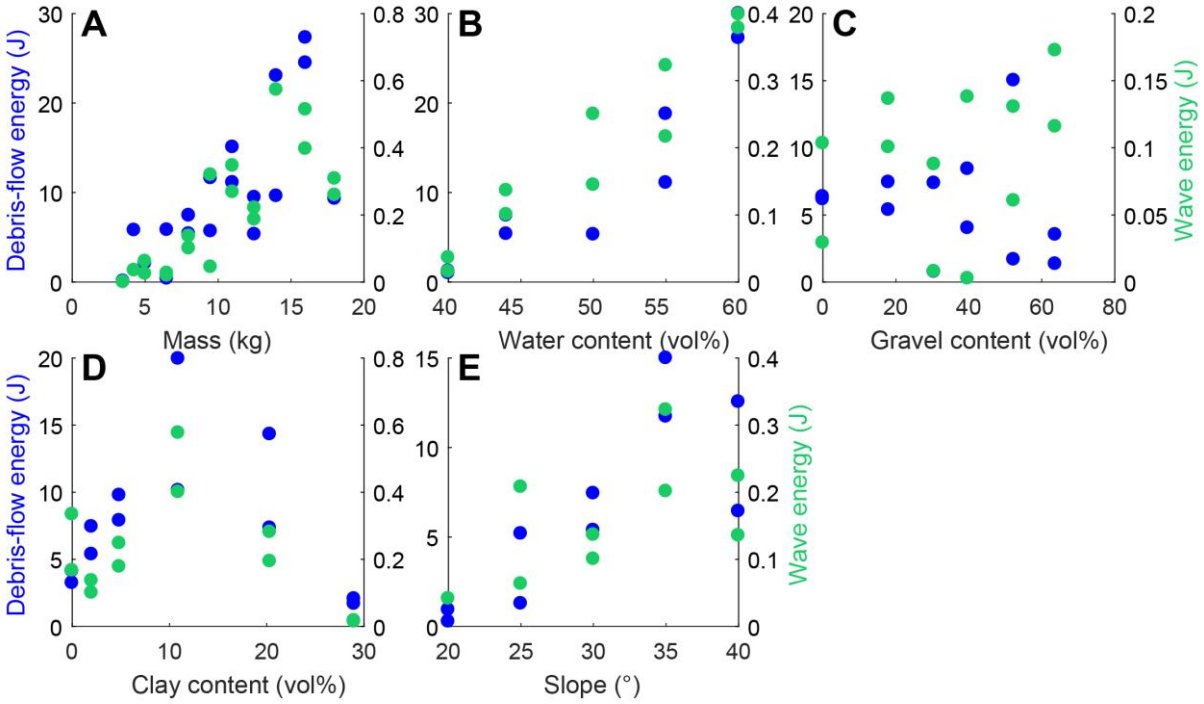

Figure 4.8. Debris-flow kinetic energy and wave energy per changed parameter.

Debris-flow energy and momentum are an expression of debris-flow mass and velocity (equation 2.6 and 3.2), and show a similar trend with debris-flow mass, composition and slope as the debris-flow characteristics described in the previous sections (Figure 4.7 and 4.8). An increasing mass and water content lead to a larger momentum and energy, while there is an optimum in energy and momentum due to varying clay content. The relation with slope also seems to show an optimum, but more runs are needed to verify this apparent trend. There is no relation with gravel content.

4.2.5 Summary debris flow characteristics

The strength of the relation between debris-flow volume, composition and slope, and its flow characteristics, is described by the R^2-value (Table 4.1). Volume seems to have the largest influence on debris flow thickness in case of a fixed debris-flow width. The lubrication of the flow, either by water or by clay, influences the outflow velocity. Weight is mostly determined by slope and volume, and is related to the debris flow thickness and the density of the flow. The characteristics of the debris flow are summarized in the parameters energy and momentum, which show the same correlations as the parameters they are derived from. The energy and momentum of the debris flow are mostly determined by water and clay content, however both volume and slope are also important indicators.

	volume	**water content**	**gravel content**	**clay content**	**slope**
thickness (outlet)	0.88	0.56	-	0.39*	0.65
weight	0.71	-	-	0.69	0.72
velocity (mean)	0.44	0.90	-	0.93*	0.43
energy	0.57	0.84	-	0.73*	0.66
momentum	0.61	0.85	-	0.68*	0.65
average strength	0.64	0.79	0	0.69	0.62

Table 4.1. R^2 values (indicating linear regression) of debris-flow parameters and the corresponding thickness, weight and velocity. The darker the green color, the stronger the correlation. No value means an insignificant relation. * indicates a polynomial regression (quadratic relation). The slope of the linear regression lines can be found in Appendix A2, Table A2.1.

4.3 Impulse waves

The general wave development and evolution can be described as follows. At t=0 s the debris flow impacts the water and wave generation starts. The debris flow pushes the water forward, until the wave celerity exceeds the debris flow velocity and the wave is detached. The wave travels away radially from its point source, its radial shape being independent of the debris-flow characteristics. The wave crest is the highest in the direction of the debris flow. The wave develops from the location where the debris flow enters the water, which is, due to the high velocity of the debris flow, in between 0.15-0.50 m. The water level measured at x_b = 0.15 m is therefore a product of volume increase and radial (back and sideward) dispersion of the generated wave. The wave travels out of the near-field region (x_b < 1 m) into the far-field region (x_b > 1 m). Here, the wave is relatively stable in amplitude and wavelength compared to the impact region. Meanwhile, as the debris flow enters the water, separation of material occurs. The fines (clay) behave as a turbidity current, while the larger grains behave as a debris flow. By displacing the water, the debris flow transfers its momentum and energy, slows down and ultimately deposits.

The initial bed of the wave basin influences the way the debris flow interacts with the basin floor, which in turns affects the wave development. When performing runs with a layer of 10 mm unconsolidated material on top of the wave basin floor, this leads among other things, to a larger detachment time and thus a larger total momentum transfer. This in turn causes a larger leading amplitude, a higher crest celerity and less time needed for the first crest to pass by x_b = 0.50 m (see appendix A2, Figure A2.5). Finally, the runout length of the deposit is longer. Presumably, the incoming debris flow stirs the loose bed, which gives an extra impulse in the direction of wave propagation. It shows the importance of the chosen boundary condition of a fixed bed. All experiments described below are conducted with an initial fixed bed.

Water level profiles at 5 near and far-field locations, recorded by cam2, are shown in Figure 4.9. The camera recording shows sinusoidal or cnoidal waves. Fluctuations smaller than 2mm are not recorded or show a spiky pattern (Figure 4.9A, t=0-1 s) as result of the camera resolution. The leading crest is typically at its maximum between x_b = 0.50-0.85 m (Figure 4.10). At this location, the wave has been pushed by the debris flow, but is not dissipated yet. The largest dissipation occurs between x_b = 0.85-1.55 m. The wave amplitude decreases and the wavelength increases. The leading wave amplitude is also the maximum wave amplitude for 17-67 % of the time in all five locations. For all locations, maximum and first amplitude show a significant linear correlation (R^2 = 0.65-0.96). However, the larger the maximum amplitude, the more often this is not the leading wave. At locations x_b = 0.50-0.85 m, the wave with the maximum amplitude at that location is most frequently the leading wave. The maximum crest amplitude is on average 1.33 times larger than the leading crest amplitude. Although the leading crest is apparently not always the highest crest, its characteristics are still very important for hazard management since it will arrive at the land first.

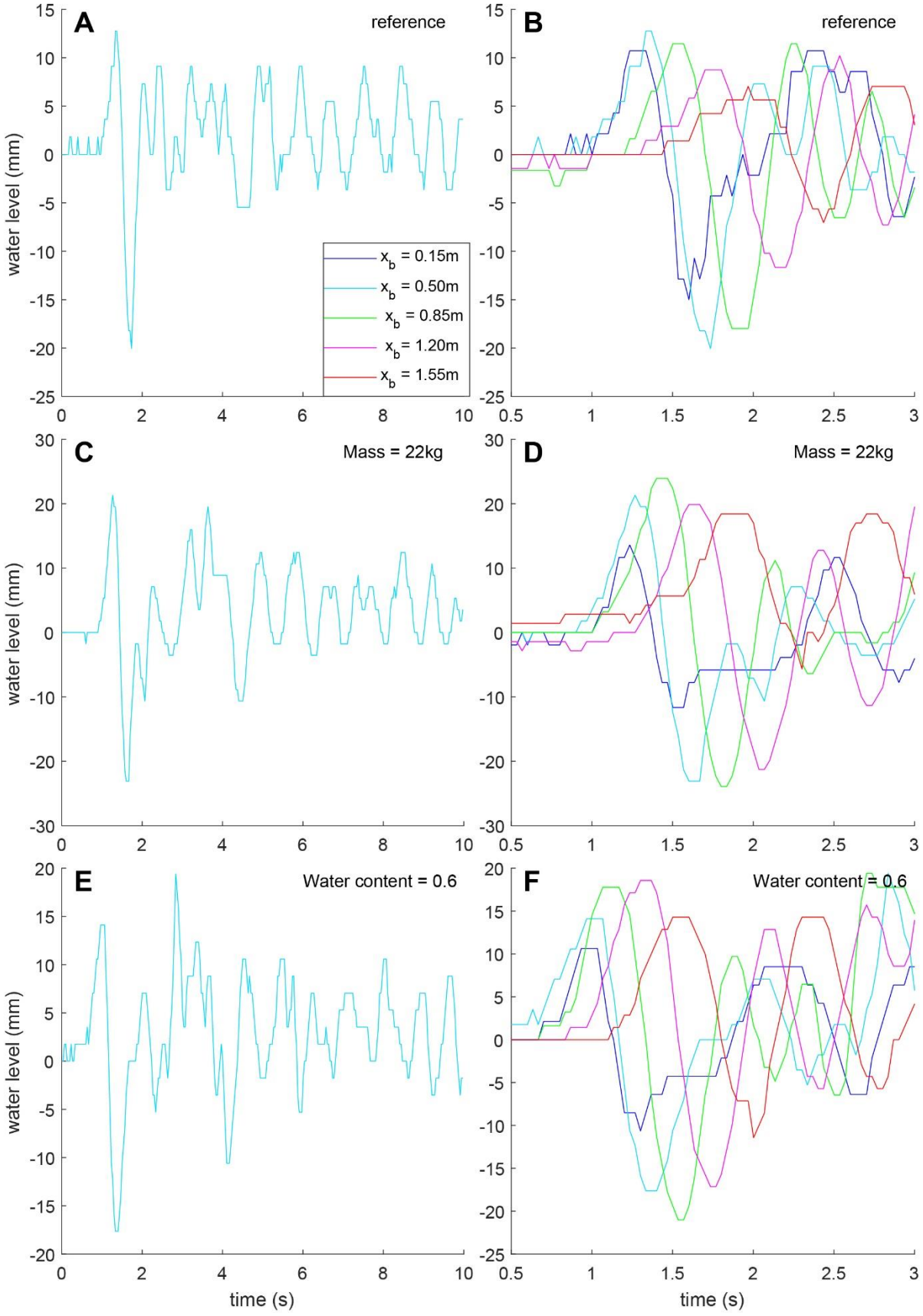
A
reference
B
reference
C
Mass = 22kg
D
Mass = 22kg
E
Water content = 0.6
F
Water content = 0.6
water level (mm)
time (s)
x_b = 0.15m
x_b = 0.50m
x_b = 0.85m
x_b = 1.20m
x_b = 1.55m

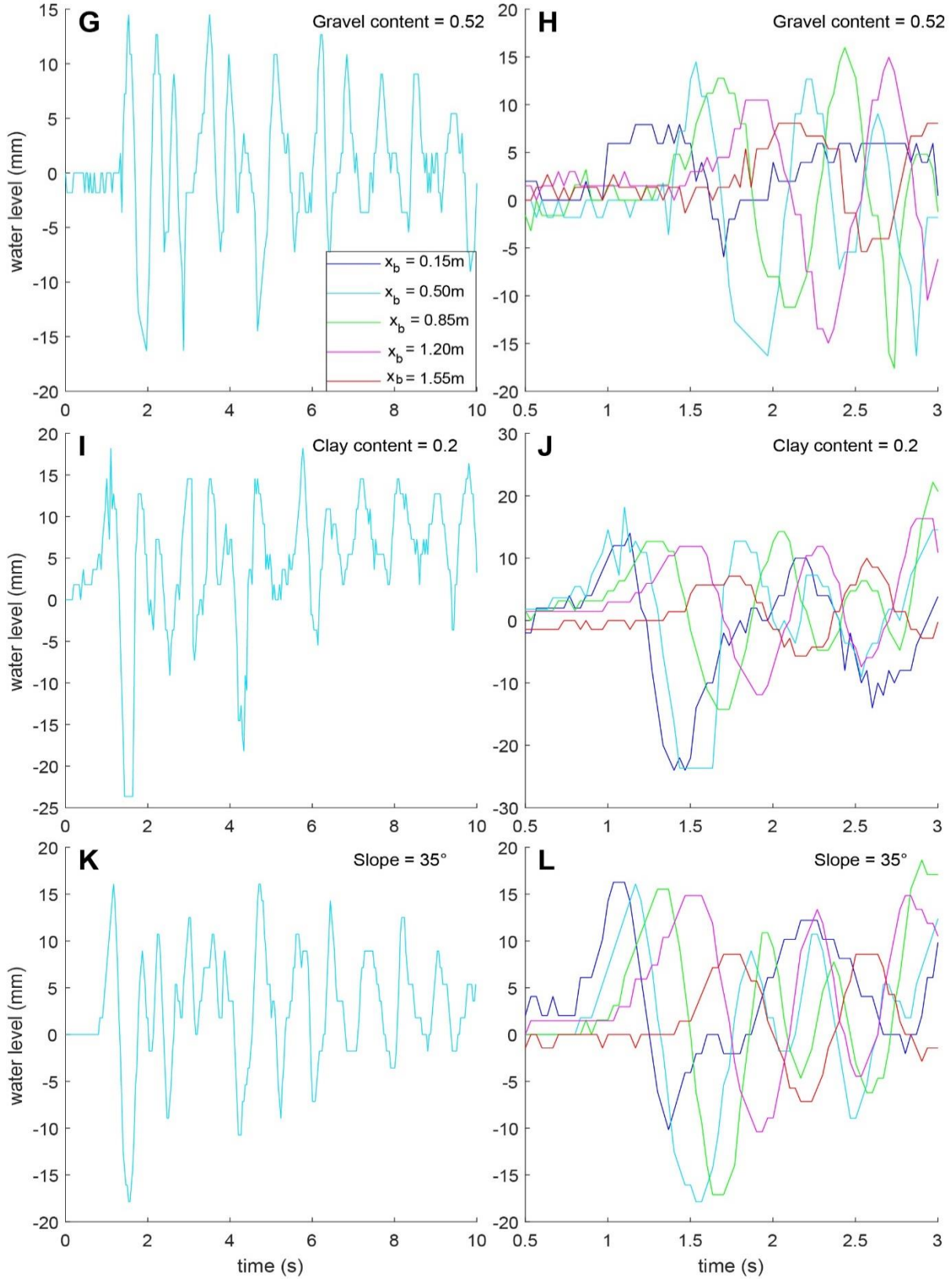

Figure 4.9. Wave profile for 6 different experiments. Left column is the wave profile at x_b = 0.50 m over the first 10 seconds after debris flow release. Right column is the leading crest and trough at x_b = 0.15, 0.50, 0.85, 1.20 and 1.55 m. **A)** and **B)** reference experiment 010. **C)** and **D)** high volume experiment 022. **E)** and **F)** high water content experiment 030. **G)** and **H)** high gravel experiment 038. **I)** and **J)** high clay content experiment 047. **K)** and **L)** high slope experiment 055.

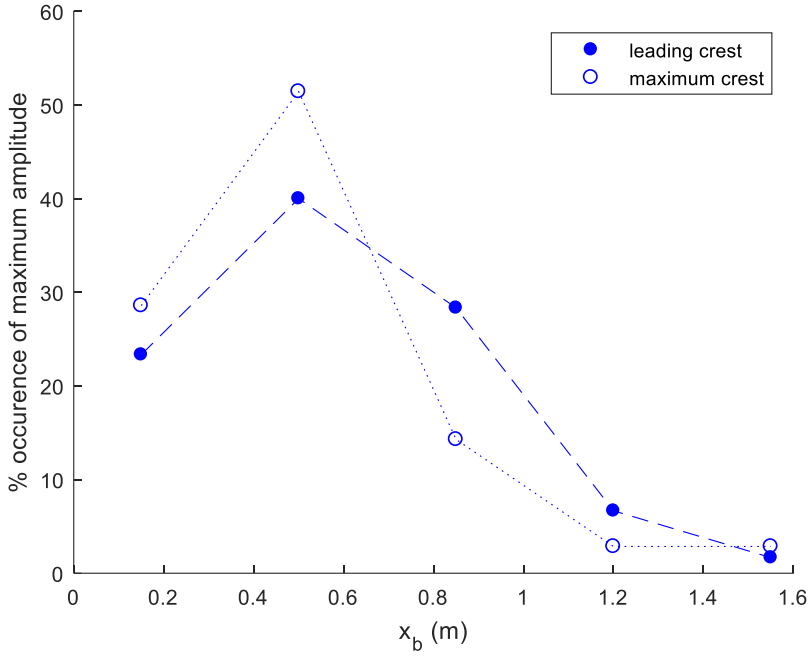

Figure 4.10. Percentage of maximum amplitude occurrence at each location. For example: almost 40 % of the leading waves has its maximum amplitude at x_b = 0.50 m.

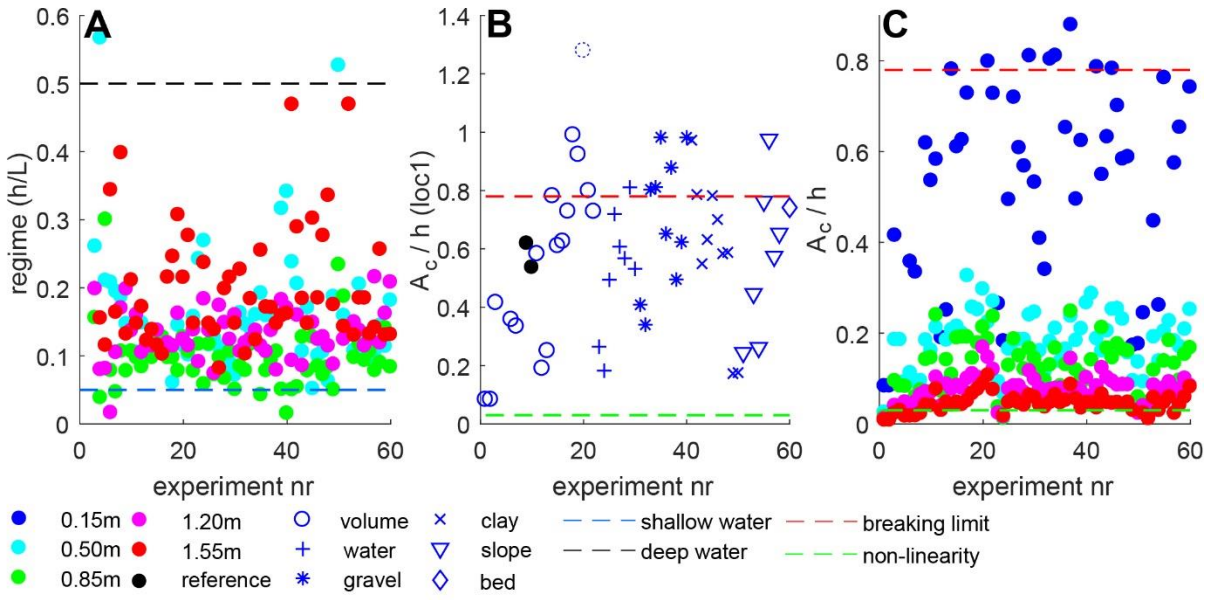

Figure 4.11. Wave regime (A) and measures of non-linearity and the breaking limit (B and C). If $A_c/h < 0.003$, waves are linear and the breaking limit (if $A_c/h < 0.78$, waves do not break). **A)** wave-regime. Almost all experiments are in the intermediate water regime (0.05<h/L<0.5) **B)** Waves are non-linear and a few are above the breaking limit at x_b = 0.15 m. The dotted blue circle is assumed to be an erroneous value. **C)** Waves become more non-linear with increasing propagation distance.

All experiments take place in the intermediate water regime (0.05<h/L<0.5) (Figure 4.11A) and no breaking occurs. Although theoretically breaking could occur at x_b= 0.15 m (Figure 4.11B, equation $a_c/h > 0.78$) this does not happen due to the down sloping wave basin. The data point which shows $a_c > h$, is excluded from the analyses (shown as dotted circle). In this experiment, the wave height was determined with the dynamical threshold and is assumed to be erroneous, since visual inspection of the video imagery did not show such extreme waves. At x_b = >0.50 m, all waves are far below the theoretical breaking limit (Figure 4.11C). Breaking is therefore no factor in suppressing the maximum crest amplitude. All waves are non-linear following equation 2.4, except for a few runs at location $x_b \geq$ 1.55 m.

On average, the celerity and the crest amplitude of the waves increases until x_b = 0.85m, due to the "pushing" of the debris flow (Figure 4.12A and D) The wave over steepens and accelerates. Further away from the debris-flow outlet, the wave celerity decreases due to friction and slowly returns to its value predicted by linear wave theory (Figure 4.12A). The period of the waves increases while traveling (Figure 4.12B). The small period near the outlet zone is caused by the over steepening of the wave, which gradually flattens out and eventually could reach a constant value. The wavelength of the waves (the product of period and celerity) increases until x_b = 0.85 m, due to the increasing period and celerity (Figure 4.12C). However, at x_b > 1.20 m the influence of the celerity takes over, and the wavelength decreases again. There is no relation between period and debris-flow volume, composition of outflow slope, neither there is for wavelength. Figure 4.12D indicates that

As expected, the crest celerity is larger than the trough celerity due to the larger water depth under the crest than under the trough ($c = \sqrt{g(h + a_{C/T})}$). The crest celerity is 1.2-1.6 larger than the trough celerity (Figure 4.13). This relation is most clear in the near-field (x_b = 0-0.50 m) and is reflected in the average celerity. The relation between wave and trough celerity shows a lot of scatter in all other locations, possibly due to dispersion and dissipation. A larger average celerity is correlated with a larger amplitude (Figure 4.14). For the crest celerity and amplitude, this relation gets stronger further away from the impact zone where the waves are less over-steepened and possibly approaching a constant value. This does not affect the trough, since this is not directly formed by the debris flow.

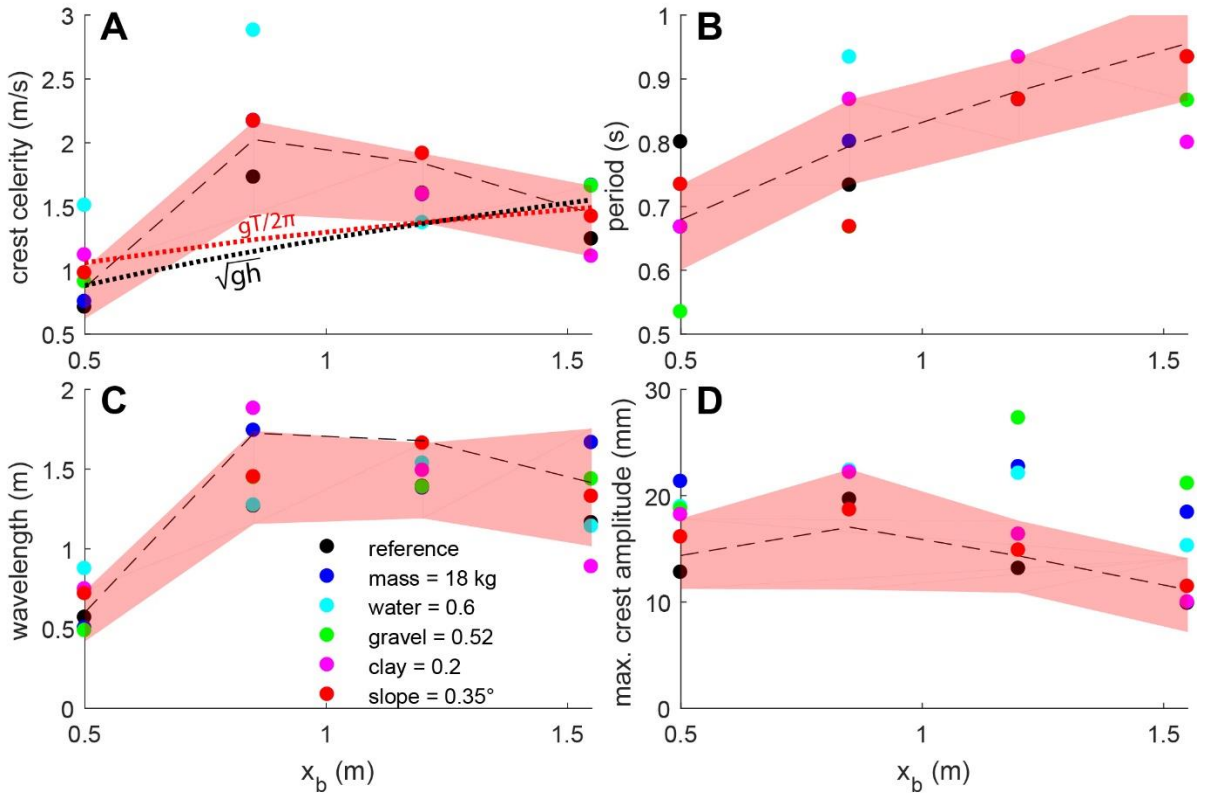

Figure 4.12. Development of wave characteristics over distance with 6 example runs shown. The mean value of all experimental runs at these locations, is indicated with a dotted line, the shaded area indicates the 25 and 75 percentile. T and λ are calculated with the symmetry method. **A)** crest celerity. The red dotted line is the predicted value according to the deep water equation, the black dotted line is the shallow water equation. **B)** period **C)** wavelength **D)** maximum crest amplitude.

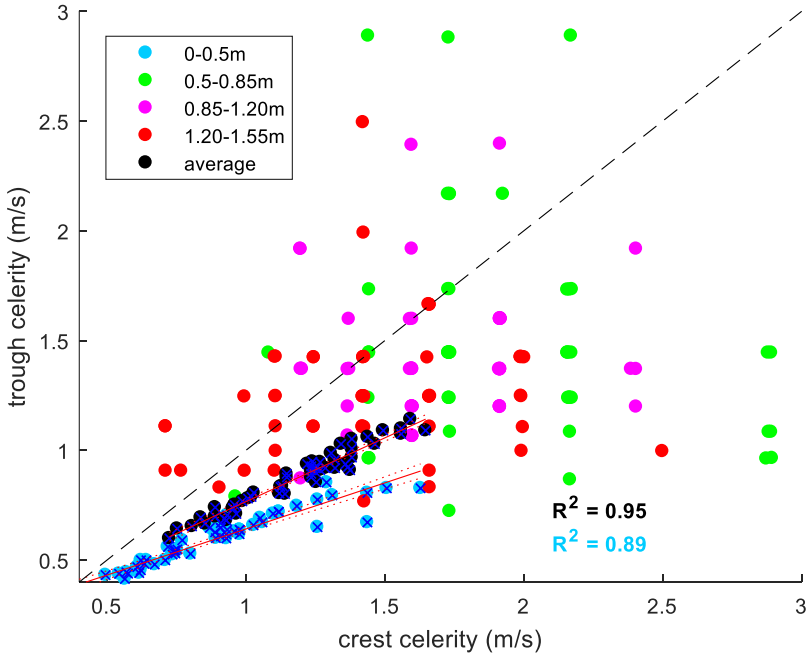

Figure 4.13. Crest celerity against trough celerity. Linear relation for the celerity between x_b = 0-0.50 m and average is indicated (p = $8.73*10^{-27}$ and $6.93 * 10^{-34}$, respectively).

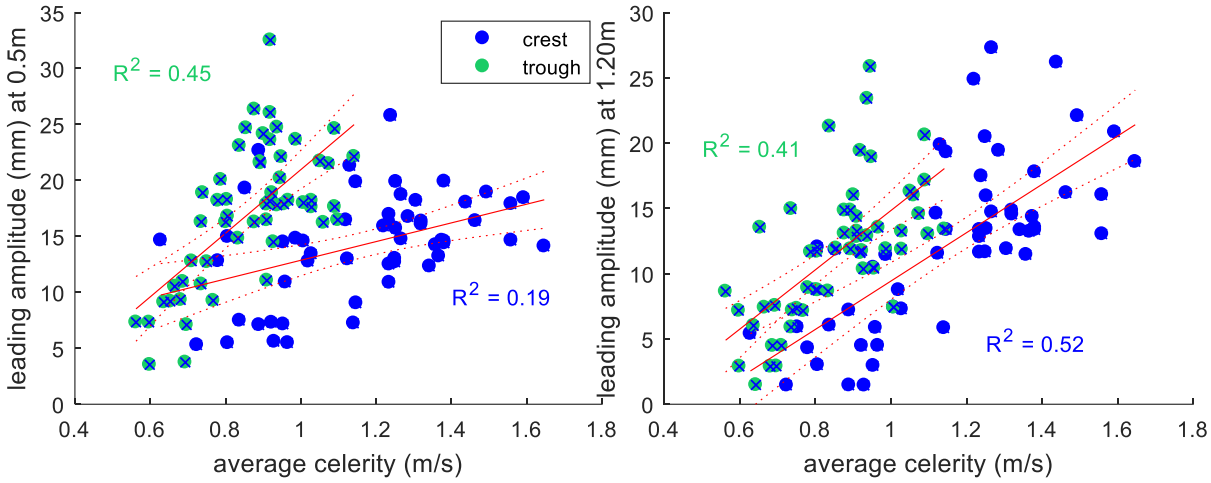

Figure 4.14. Crest celerity against leading amplitude for location x_b = 0.50 m (**A**) and x_b = 1.20 m (**B**). The corresponding P-values are p = $9.09*10^{-4}$, $2.3*10^{-8}$ for A (crest and trough) and p = $4.45*10^{-10}$, $9.52*10^{-8}$ for B (crest and trough).

4.3.1 Debris-flow volume

Wave generation is influenced by debris-flow volume (Figure 4.15 and supplementary movies S1 and S2). The runs with a low volume show a relatively small amount of air entrainment, a quick release of the wave and therefore the development of more, smaller waves following the leading crest. Very low debris-flow volumes cause waves with such a low amplitude (<2 mm) that surface tension can start to play a role and scale effects become more important (see section 5.3.2).
For a mass of 4.25 kg, the wave is already detached at t = 0.4 s. If the volume increases, some water drops and grains jump out of the water due to debris-flow impact, which can travel distances of 30cm through the air. From 8.0 kg onwards, a splash is heard when the debris flow impacts the water, indicating an impact crater, which can be seen at t=0.1 s for 16 kg in Figure 4.15. The highest volumes show indeed a forward collapsing impact crater and a lot of turbulence. Large grains (basaltic gravel) jump out of the water or follow the turbulent upper layer of the water. For a volume of 16 kg, detachment of the leading wave occurs at t = 1.2 s, outside of the time span of the shown figure.

As the debris-flow volume increases, the crest and trough amplitude (both leading and maximum) increase as well (Figure 4.16A). This relation is significant for all locations for the crest amplitude (R>0.6, p<0.001), and also for the trough amplitude excluding the very near wave field (x_b = 0.15 m) and far-field (x_b = 1.55 m). The travel time between the moment the debris flow impacts the water and the passing by of the leading crest or trough at x_b = 0.50 m (indicating the initial celerity), decreases with debris-flow mass (Figure 4.16B). This is explained by the increasing average celerity with increasing mass (Figure 4.16C).

All waves are highly non-linear near the landslide source and become less non-linear with increasing propagation distance. Only for the smallest debris-flow volumes, the waves become ultimately linear in the far-field (Figure 4.17).

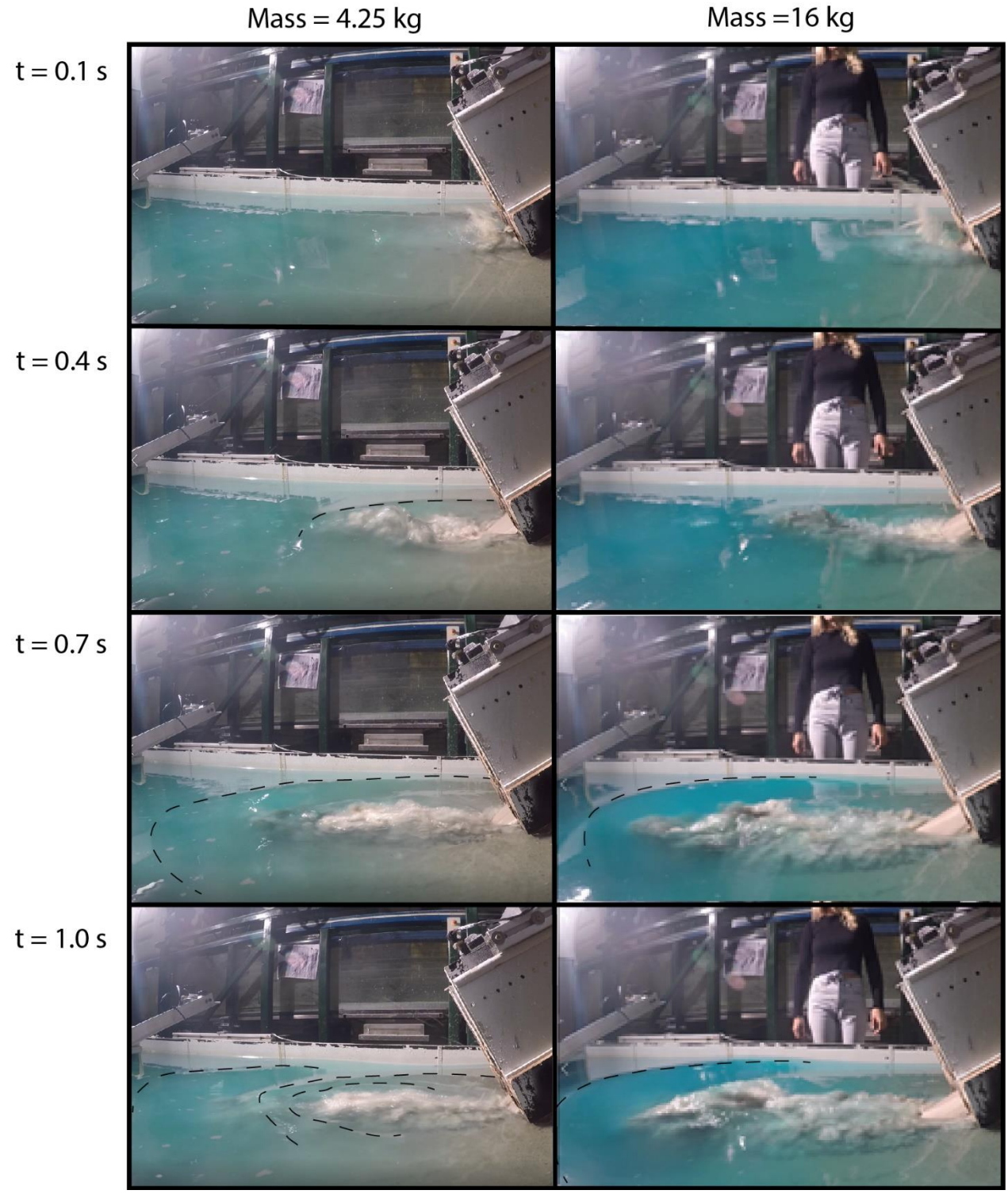

Figure 4.15. Wave generation and propagation in the first second after impact, for a large and small debris-flow mass.

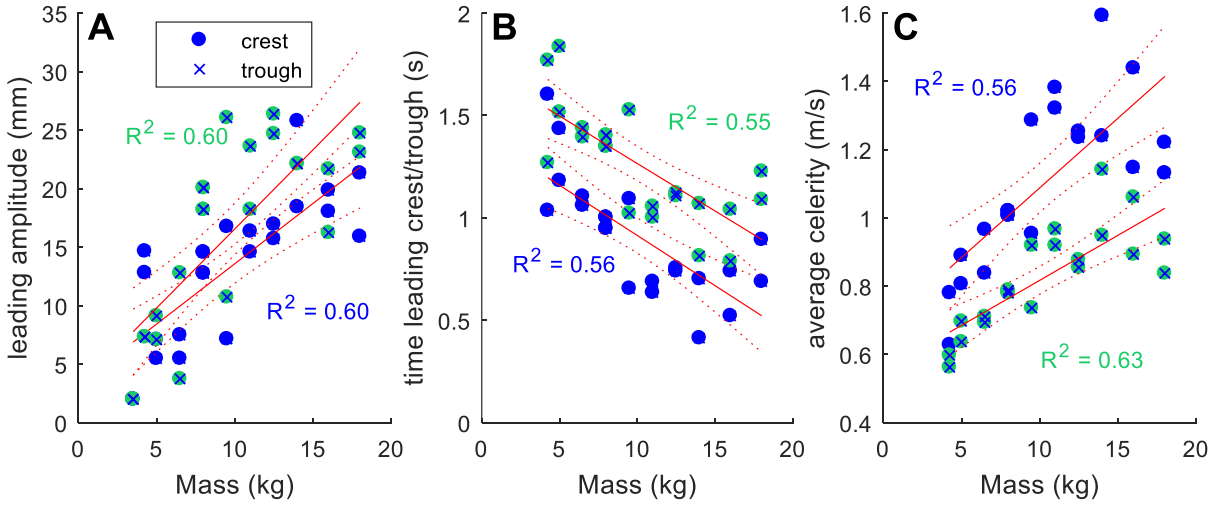

Figure 4.16. Debris-flow volume against various wave characteristics. **A)** leading amplitude at x_b =0.50 m p = 7.91^{-6}, 8.85^{-6} for crest and trough. **B)** time when leading crest/trough passes by x_b = 0.50 m, p = 5.87^{-5}, 8.07^{-5} for crest and trough. **C)** average celerity p = 3.84^{-5}, 5.95^{-5}

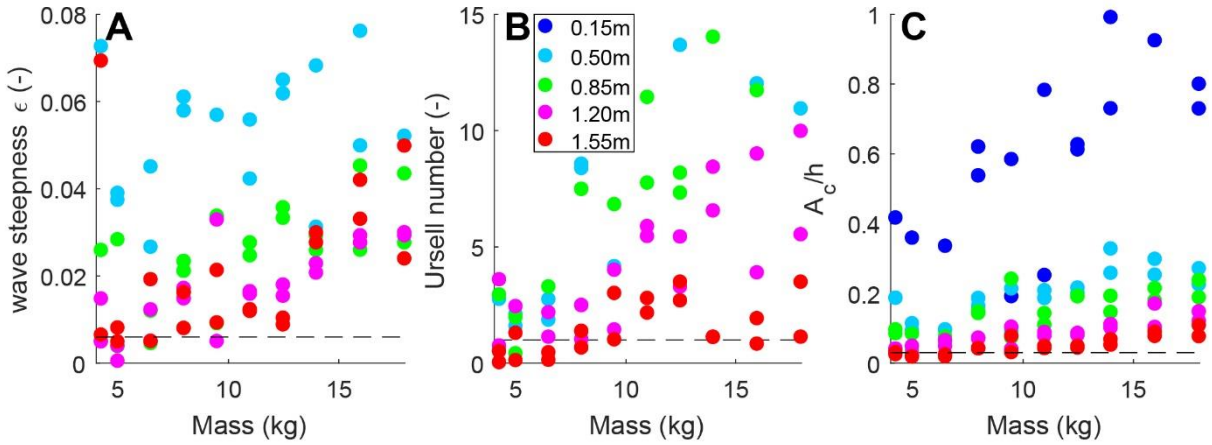

Figure 4.17. The non-linearity of waves against debris-flow mass on five different locations of x_b. All data points under the dotted threshold are linear waves. Non-linearity is expressed in: **A)** ϵ (equation 2.3), **B)** U (equation 2.5) and **C)** ϵ_c (equation 2.4).

4.3.2 Debris-flow composition

The wave evolution caused by debris flows with a low water content is characterized by a quick dispersion of waves (supplementary movie S3). With a water content of 0.4, only capillary waves travel further than x_b = 0.85 m. At t = 1.0 s, the wave is already fully dissipated (Figure 4.18). Many small ripples develop when the debris flow keeps moving into the water after the first impact. With an intermediate water content of 0.5, the waves develop a steeper front (t = 0.4 s). At t = 1.0 s, the leading wave already traveled out of the near-field zone and low water level can be seen at x_b = 0.50 m, indicating the trough passing by. When increasing the water content, a forward collapsing impact crater is visible (content = 0.6, t = 0.1 s). Furthermore, the radius of propagation decreases, which causes a longer travel time to reach x_b = 0.15 m. The detachment time is longer, and at t = 1.0 s the wave is still being pushed by the debris flow (supplementary movie S4).

Figure 4.19 shows the wave generation for two runs with a relatively high gravel content. Unfortunately, there is no comparable imagery for runs with a low gravel content. When increasing the gravel content of the debris flow, a steeper wave front is observed (gravel content 0.52, t = 0.7 s). With a gravel content of 0.52, there is no impact crater (t = 0.1 s), however it is very clear how gravel is pushed upwards, and even rises above the water (Figure 4.20 t = 0.4 s, Figure 4.20 and supplementary movie S5). The steep wave front is detached at 1.0 s. With an even larger gravel content, even more turbulence is observed, and water droplets are ejected into the air (gravel content = 0.64, t = 0.4 s). At t = 1 s, the leading wave is already detached and a secondary wave is formed.

Debris flows with a high clay content show more turbulence and jumping particles than flows with less clay (Figure 4.21, clay content = 0.2, t = 0.4 s). Dispersal of a clay cloud in all directions can be observed by all runs (except with a clay content of 0). The clay cloud continues dispersing in the wave propagation direction even if the debris flow stopped pushing, which can be perfectly seen in Figure 4.21, clay content = 0.05 at t = 0.7 s. At this time, the wave is already detached from the pushing of the debris flow, but the clay cloud keeps expanding. At t = 1.0 s, a second wave is formed. Debris flows with an even higher clay content (in our case, a clay content of 0.29) are more visous, and outflow in muliple surges occurs. At t = 0.7 s, the second outflow surge is captured, which is large enough to cause a significant wave. The debris flow deposits quickly, and the impulse wave is released relatively quick with at a low celerity (t = 1.0 s). See also supplementary movies S6 and S7.

An increase in water content results in a higher and faster wave (Figure 4.22A, B, C). Especially the relation between water content and wave celerity is strong (R^2 = 0.88 and 0.91 for crest and trough), in contrast to the relation with amplitude. All waves are non-linear, and the non-linearity is increasing with increasing water content (Figure 4.23A, B, C).

The gravel content of the debris flow does not seem to have a relation with the wave characteristics (Figure 4.22D, E, F). One could see a decreasing celerity with increasing gravel content, but there is too much scatter to say anything decisive about this. The same is true for measures of wave non-linearity (Figure 4.23D, E, F). Although there are clearly visual differences of the wave characteristic as described above, it does not show any trend. The parameter values are similar, indicating that gravel content has a less differentiating effect on these parameters.

The response of the waves on clay content, reflects the behavior of the debris flow as described in section 4.2.2. An increasing clay content lubricates the debris flow, resulting in a higher wave celerity, up till a certain point where the flow becomes too viscous and the wave celerity decreases (Figure 4.22G, H, I). The results of this behavior are poorly reflected in the wave amplitude. The cloud of clay diffusing into the water body can locally increase the water density and might suppress the wave amplitude. The wave non-linearity follows this optimum, with the largest non-linearity at a relatively high clay content, and the most linear waves at the highest clay content (Figure 4.23G, H, I).

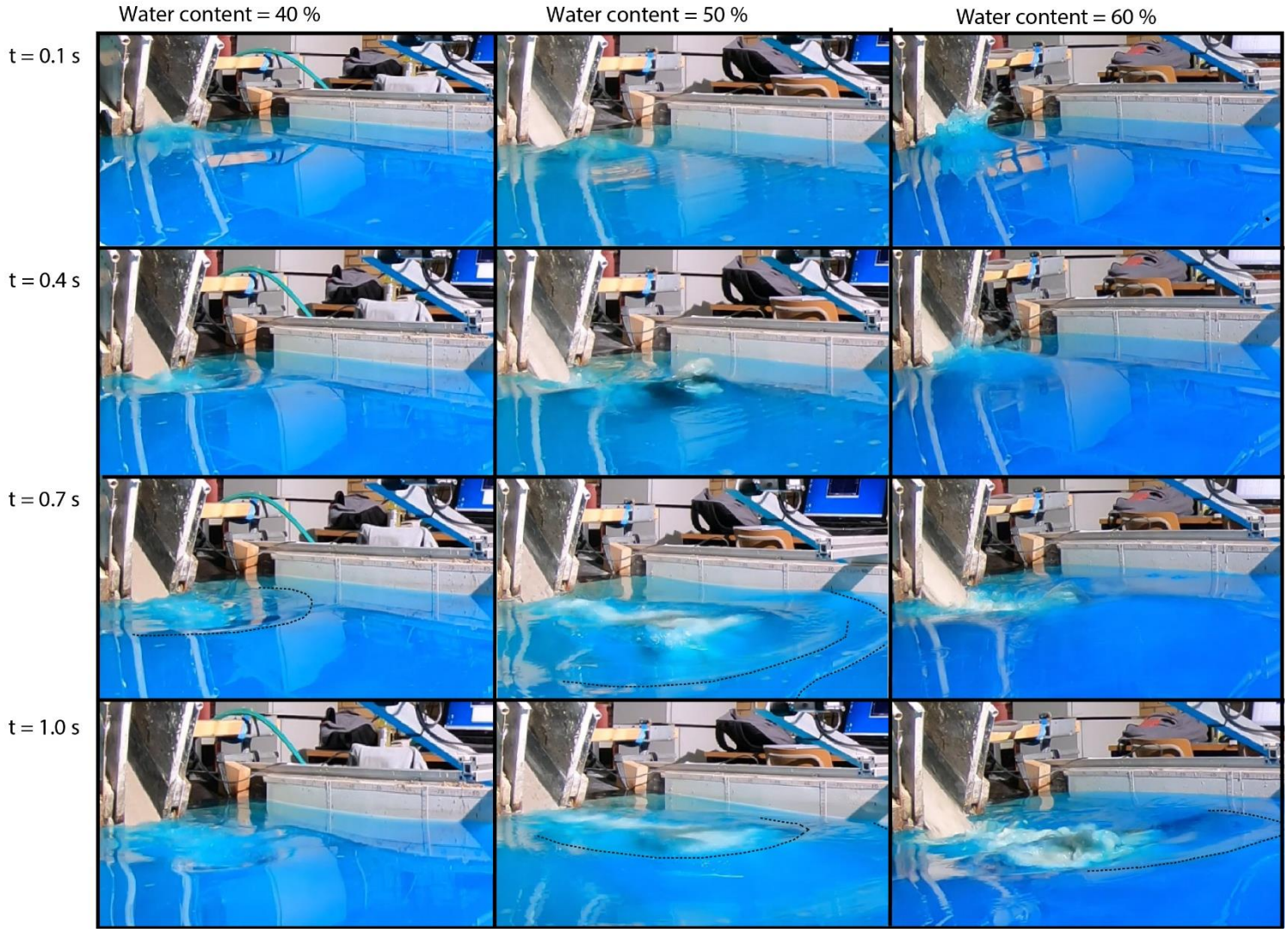

Figure 4.18. Wave generation and propagation in the first second after impact, for different a low, intermediate and high water content (vol%).

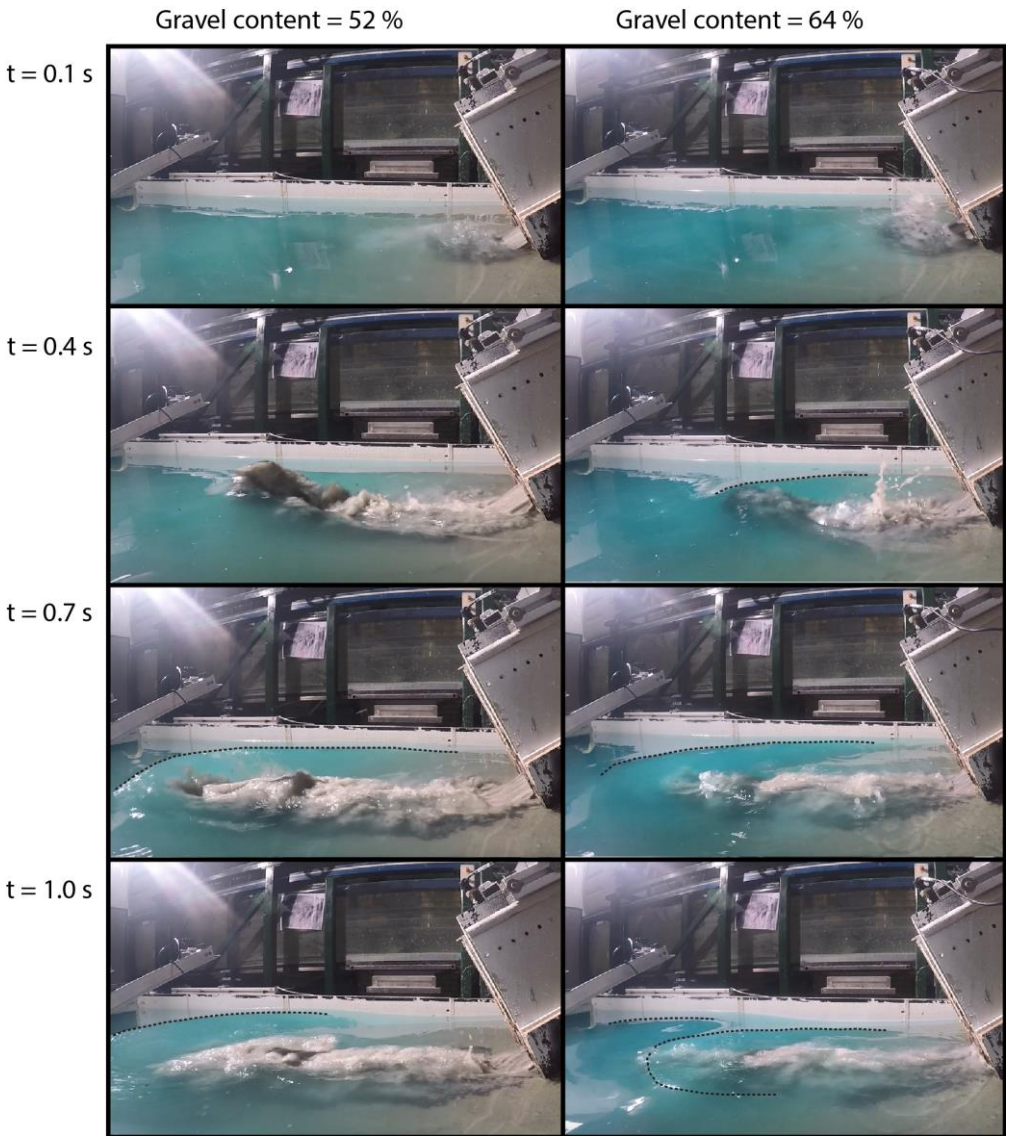

Figure 4.19. Wave generation and propagation in the first second after impact, for an intermediate and high gravel content (vol%).

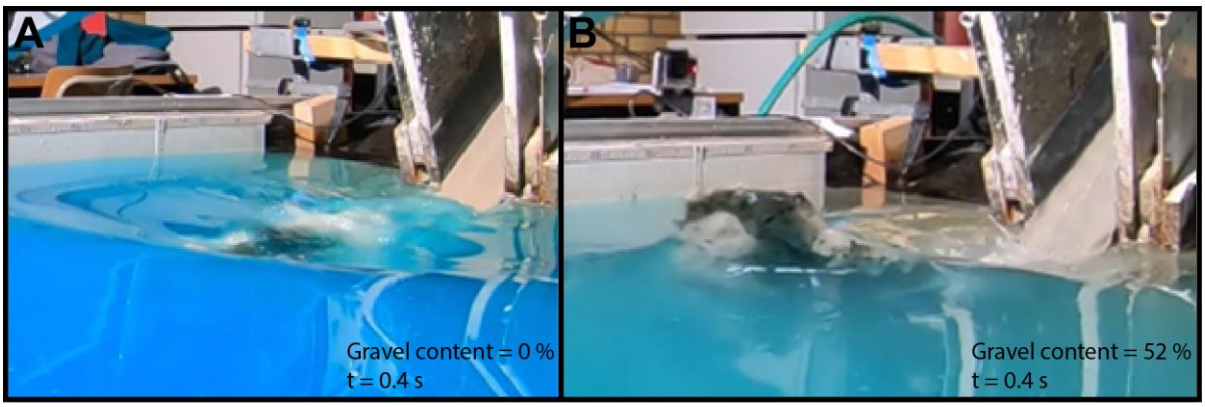

Figure 4.20. Wave generation recorded with cam 2, during the gravel variation experiments at t = 0.4 s. **A)** gravel content = 0 vol%. The debris flow smoothly flows into the water and creates a relatively gentle wave. **B)** gravel content = 52 vol%. A lot of turbulence pushes the gravel particles out of the water.

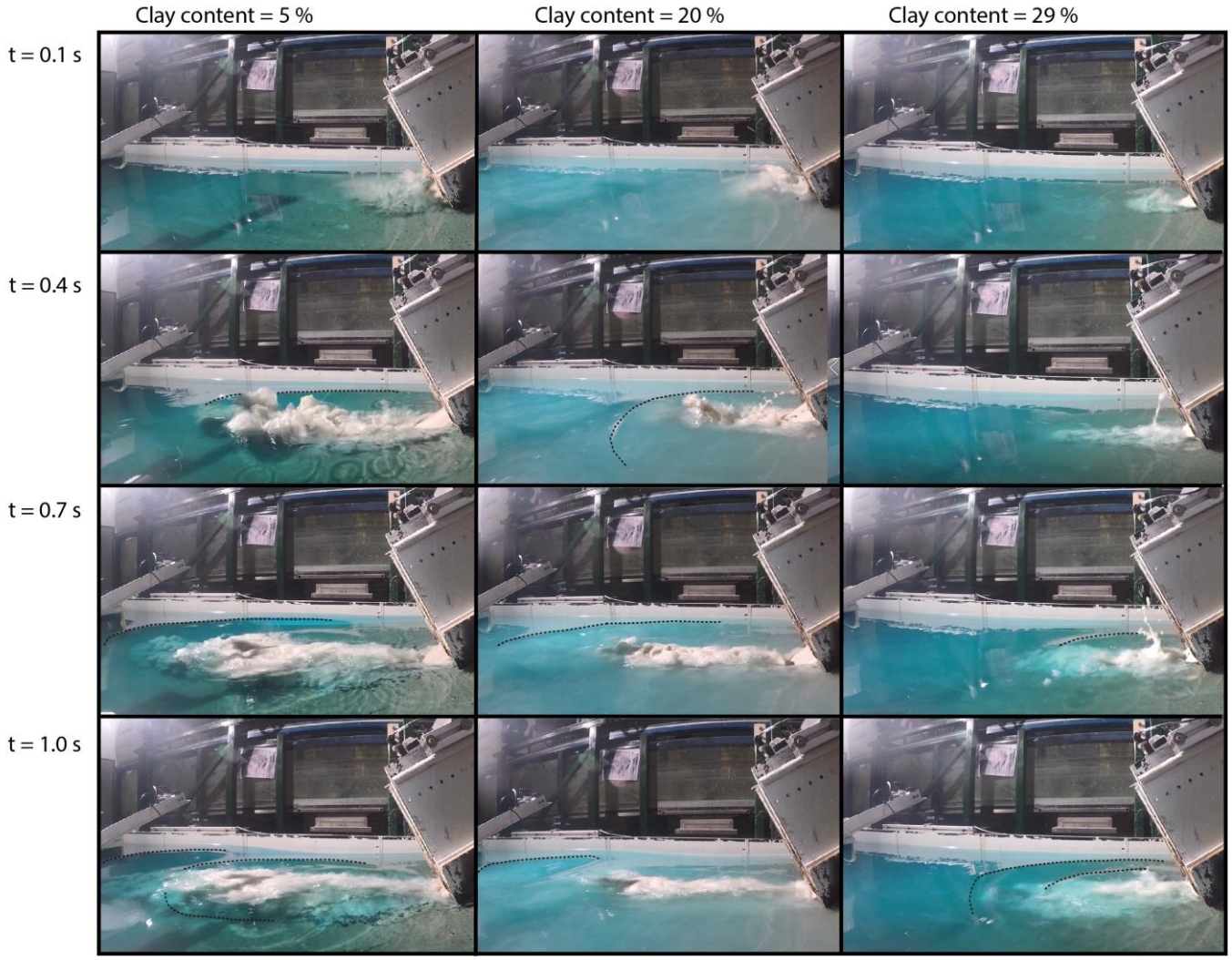

Figure 4.21. Wave generation and propagation in the first second after impact, for different a low, intermediate and high clay content (vol%).

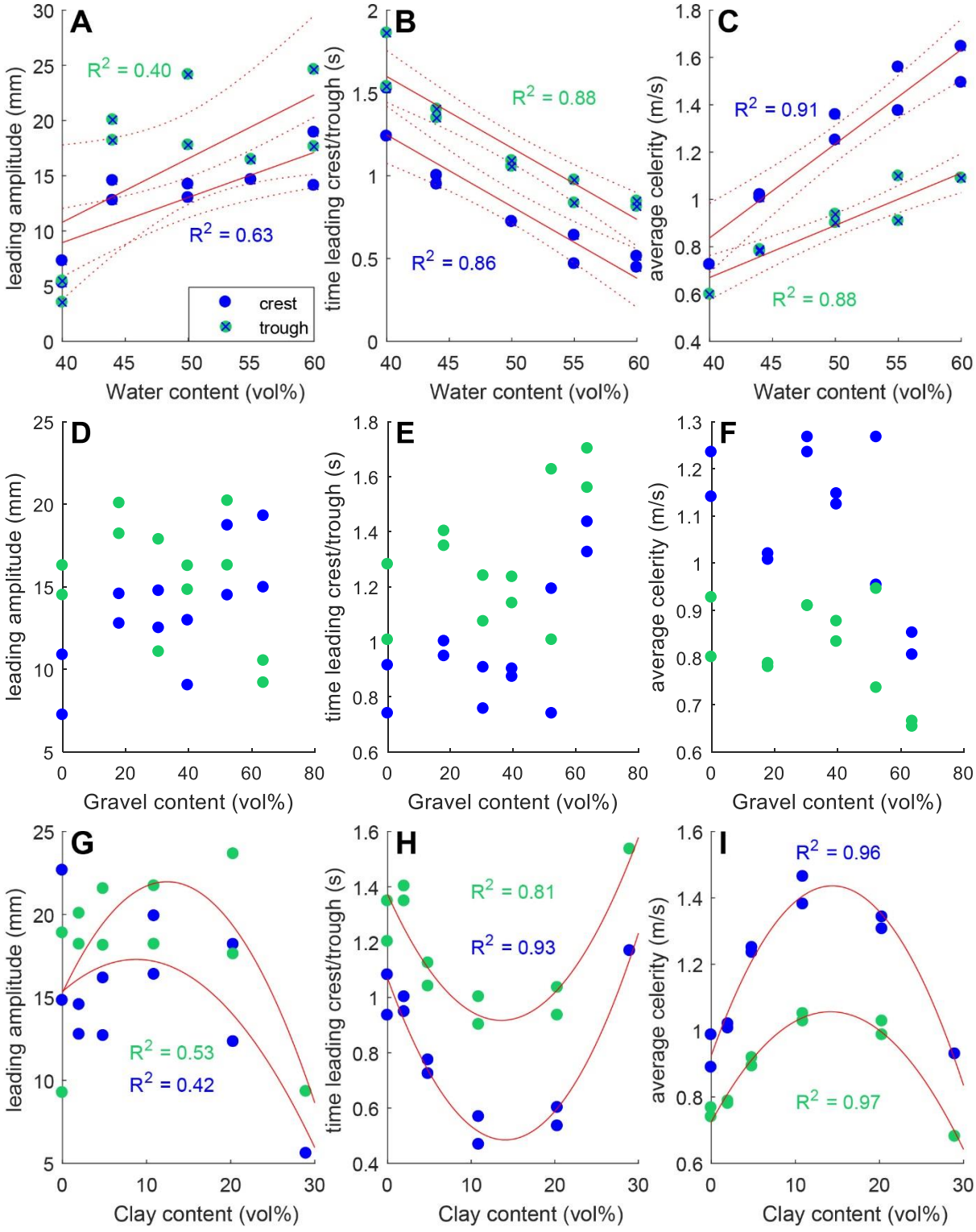

Figure 4.22. Relation between debris-flow composition and wave characteristics. B, E and H show the travel time of the leading crest to pass by x_b = 0.50 m. **A), B), C)** water content. **D), E), F)** gravel. **G), H), I)** clay. The P-values of the linear regression lines are A: p = 0.006 (crest) 0.050 (trough), B: 1.1^{-4} (crest) 5.58^{-5} (trough), C: 7.44^{-5} (crest) 1.8^{-4} (trough)

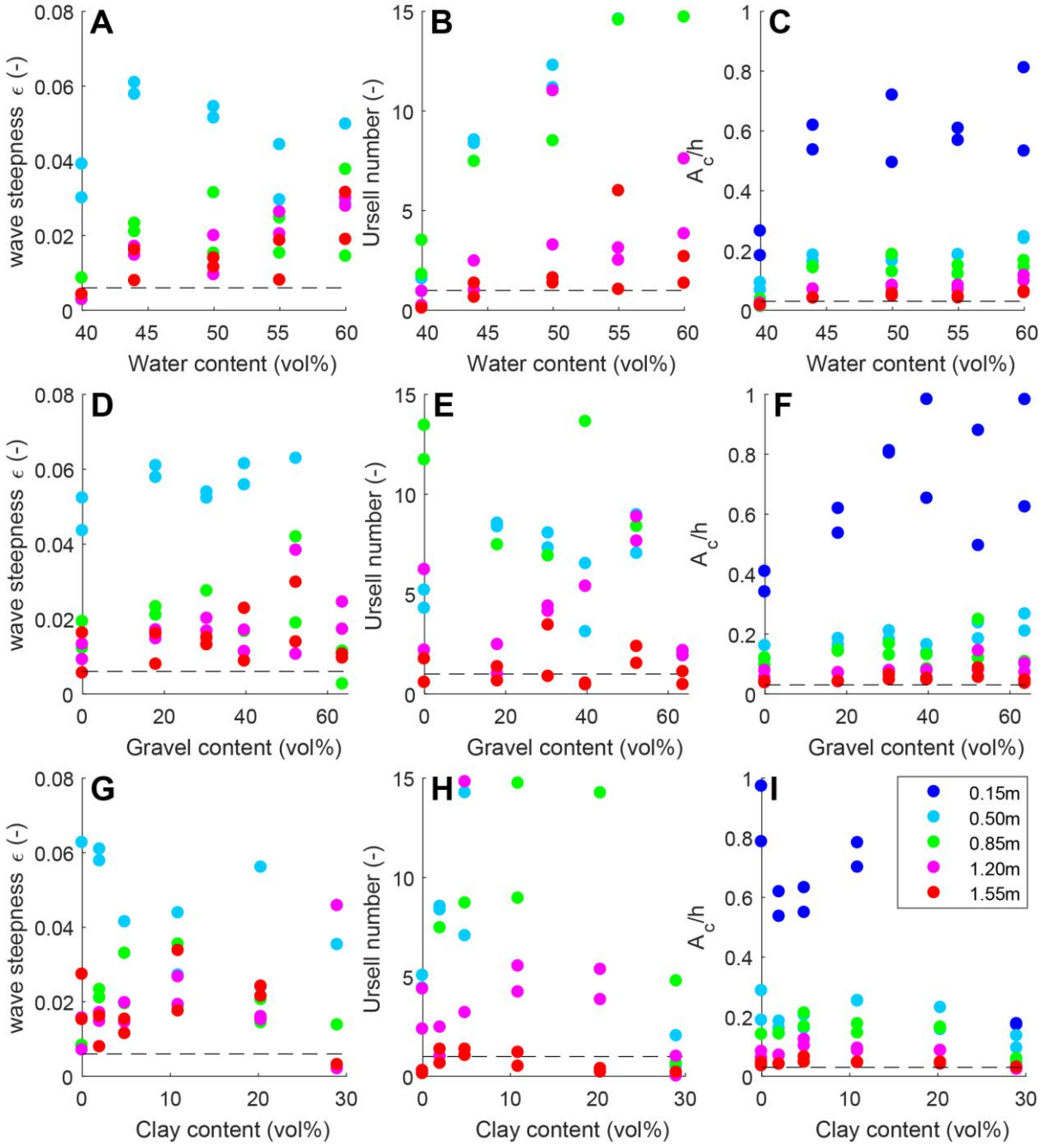

Figure 4.23. The non-linearity of waves against debris-flow composition on five different locations of x_b. All data points under the dotted threshold are linear waves. Non-linearity is expressed in: A) ϵ (equation 2.3), B) U (equation 2.5) and C) ϵc (equation 2.4).

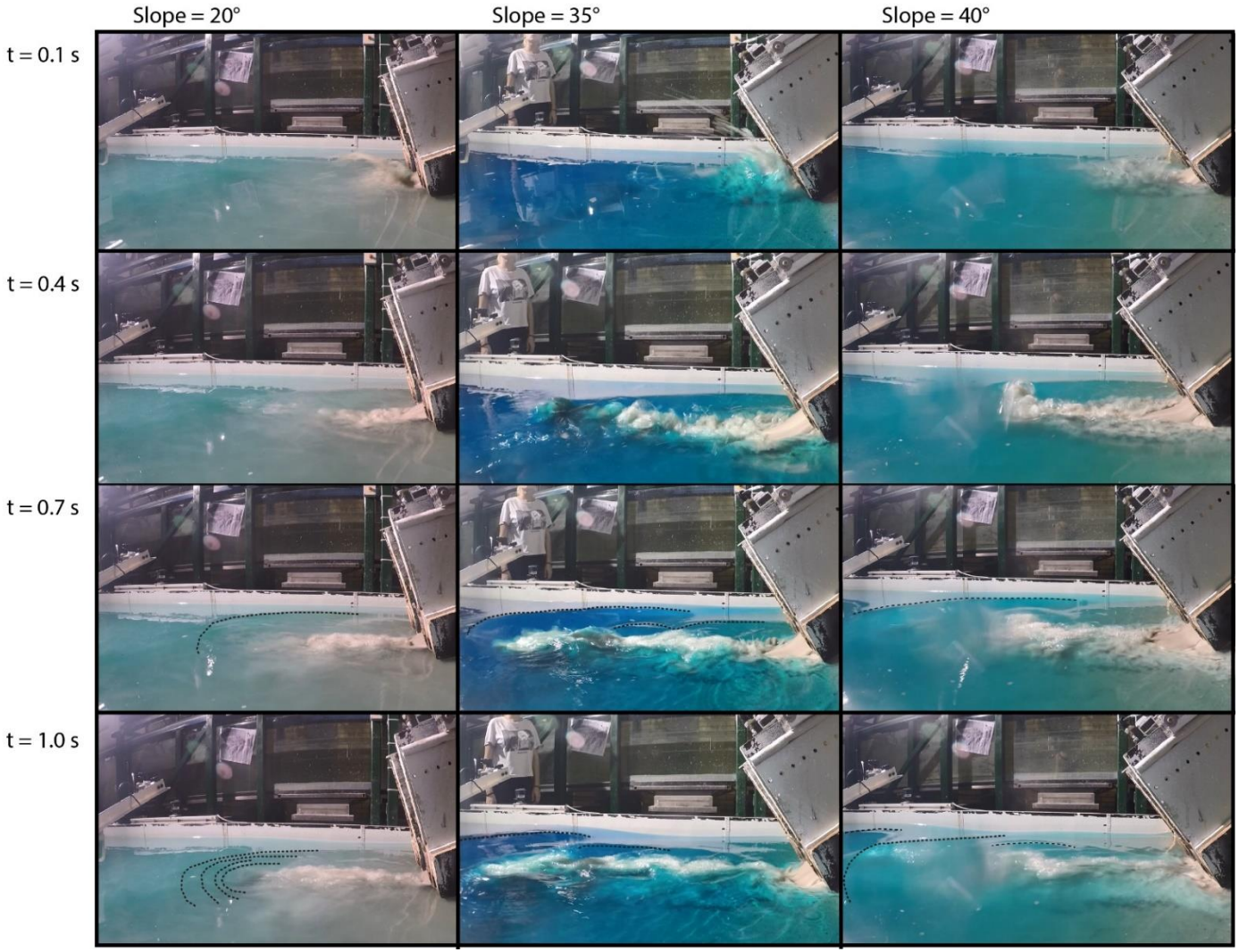

Figure 4.24. Wave generation and propagation in the first second after impact, for different a low, intermediate and high outflow slope.

4.3.3 Outflow slope

With a low outlet slope (20°) the debris flow flows smoothly into the water, and no impact crater or much turbulence occurs (Figure 4.24, t = 0.1 -0.4 s and supplementary movie S8). The wave detaches relatively quickly from the debris flow, and many small waves or ripples are formed (t = 1.0 s). When increasing the slope to 35°, more turbulence occurs, and water droplets are ejected into the air and come down up till 50cm further (causing small circular ripples in the water, see t= 0.7 s and supplementary movie S9). Gravel particles on top of the upper turbulence layer are observed. Due to the higher debris-flow velocity, it flows out farther into the water, supplanting the water and thereby moving the starting point for wave generation further away from the outlet (t = 0.4 s). An even larger outflow slope (40°) shows much less turbulence during wave generation, resulting in less steep waves with a lower celerity.

Intuitively, an increase in slope would cause higher and faster waves. This trend is shown in Figure 4.25A. There is indeed an increase in celerity with an increasing slope, but the largest outflow slope results into lower and slower waves (Figure 4.25B, C). Waves show the most linear behavior at x_b = 1.55 m, for the smallest and the largest outflow slope (Figure 4.26).

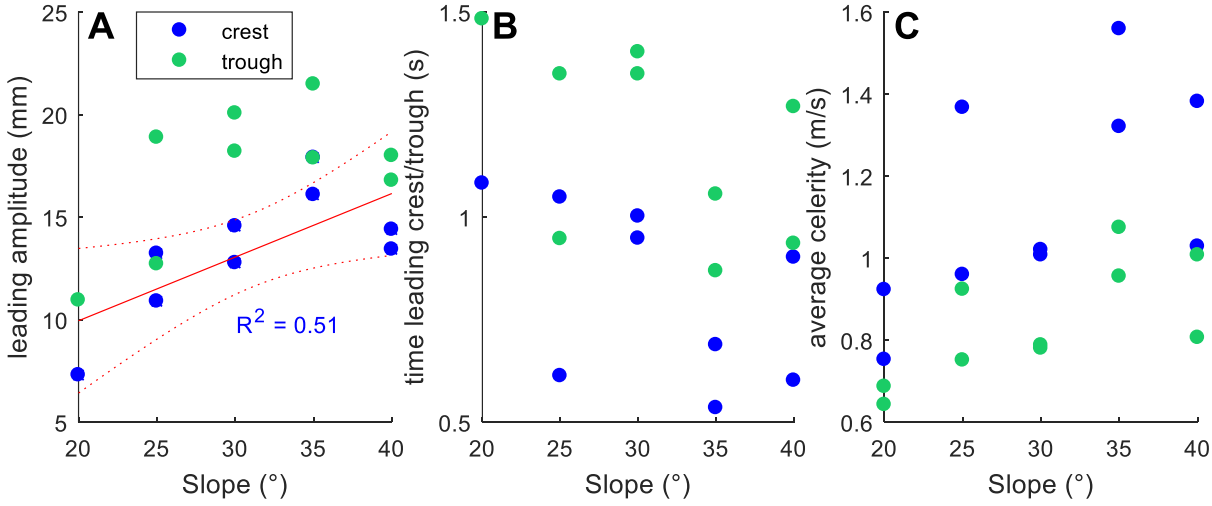

Figure 4.25. Relation between outflow slope and wave characteristics. **A)** leading amplitude at x_b = 0.50 m p = 0.03. **B)** travel time of leading crest/trough to pass by x_b = 0.50 m. **C)** average celerity.

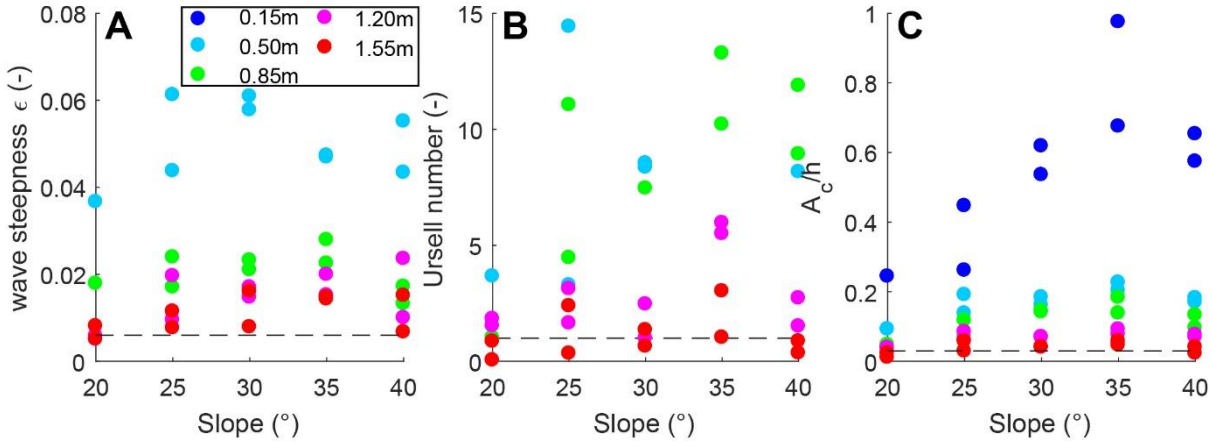

Figure 4.26. The non-linearity of waves against outflow slope on five different locations of x_b. All data points under the dotted threshold are linear waves. Non-linearity is expressed in: **A)** ϵ (equation 2.3), **B)** U (equation 2.5) and **C)** ϵ_c (equation 2.4).

4.3.4 Summary of wave characteristics

Wave generation differs significantly for different experimental runs. A high volume, water content, gravel content and slope and an intermediate clay content, result in the formation of an impact crater and a lot of turbulence when the debris flow impacts the water.

The strength of the linear relations studied above is reflected by the R^2-value (Table 4.2). Debris-flow water content is the parameter which is the strongest related to wave characteristics. Volume has a large influence on leading amplitude and is also linked to celerity. Clay content shows optima and is therefore not linear relatable to wave characteristics. However, the quadratic relations show that clay content is highly correlated with average wave celerity. The outflow slope seems to show an optimum at 35°, but more research is needed to verify this. Generally, a larger slope enhances the relations described above. Waves are always non-linear, except in the far-field. A larger amplitude and celerity results in more non-linear waves.

The best predictable data output so far, is in the region of x_b = 0.50 - 0.85 m. Here, the waves are detached but not yet dispersed. The space-average data of wave celerity is the best related to debris-flow characteristic. The data from the leading crest is the most important for hazard management purposes. Therefore, I chose to focus on this data-output for further analyses in section 4.4.

	volume	water content	gravel content	clay content	slope
leading crest amplitude	0.60	0.63	-	0.44*	0.51
time leading crest to x_b = 0.50	0.56	0.86	-	0.75*	0.27
average crest celerity	0.56	0.91	-	0.96*	0.35
wave energy	0.65	0.92	-	0.58*	0.33
average strength	0.59	0.83		0.68	0.37

Table 4.2. R^2 values (indicating linear correlation) of debris-flow parameters and the corresponding wave amplitude, travel time and velocity. The darker the green color, the stronger the correlation. No value means an insignificant relation. * indicates a polynomial regression (quadratic relation). The slope of the linear regression lines can be found in Appendix 2, Table A2.2.

4.4 Influence of debris flow on impulse wave

First, statistical relations are explored to explain wave behavior. Next, energy and momentum calculations are implemented in an attempt to generalize an explanation for wave behavior.

4.4.1 Relation between debris-flow and wave characteristics

As the debris-flow velocity increases, the leading crest amplitude increases as well (Figure 4.27A). The strength of this relation increases with increasing distance from the impact area, except at x_b = 1.55 m, where dispersion and diffraction have a larger influence on the wave amplitude (R^2 = 0.24, 0.30, 0.41, 0.50, 0.34 for x_b = 0.15, 0.50, 0.85, 1.20 and 1.55 m, respectively). The larger the debris-flow velocity, the earlier the leading crest or trough passes by x_b = 0.50 m (Figure 4.27B). This is related to the increase in average wave celerity with increasing debris-flow velocity (Figure 4.27C). The outliers with a longer travel time refer to experiment 50 with the highest clay content. In this experiment, the debris flow was very viscous and the outflow of the debris occurred in two phases where only the second phase caused significant wave formation. The relation described in Figure 4.27B and C is significant for all locations, although the strength of this relation decreases with increasing distance from the impact area. This indicates a direct influence of debris-flow velocity on wave celerity during wave generation. The same trends are found between wave characteristic and effective mass (Figure

4.27D, E, F). The relations are equally strong for amplitude, and clearly effective mass is less correlated with celerity than debris-flow velocity. Effective mass is a variable which is not only dependent on debris-flow behavior, but also on the wave generation and development since the detachment time determines partly the effective mass. It is therefore a less suitable variable for potential wave characteristic predictors.

There is no significant relation between debris-flow thickness (outlet or middle) and weight with wave amplitude, time or celerity (see appendix A2, Figure A2.6 An increase in debris-flow thickness or weight leads to larger crest and trough celerity, but this relation is not strong (R^2 <0.4). The R^2 value increases with increasing distance from the impact area. This again reflects the over steepening and acceleration caused by the debris flow, gradually returning to a natural balance.

The detachment time (or effective time) is especially low for debris flows with a low velocity and low flow thickness. After a certain threshold of debris-flow velocity, the amount of scatter in this relation increases (Figure 4.28A and B). An increased debris-flow velocity means that there is more time needed for the wave celerity to exceed the debris flow velocity and detachment occurs. An increase in detachment time correlates relatively well with an increase in leading crest amplitude (Figure 4.28C), especially for x_b = 0.85-1.55 m (R^2 = 0.43-0.45), where the wave is already detached. There is no relation between detachment time and debris-flow thickness, wave celerity, wave period or wavelength.

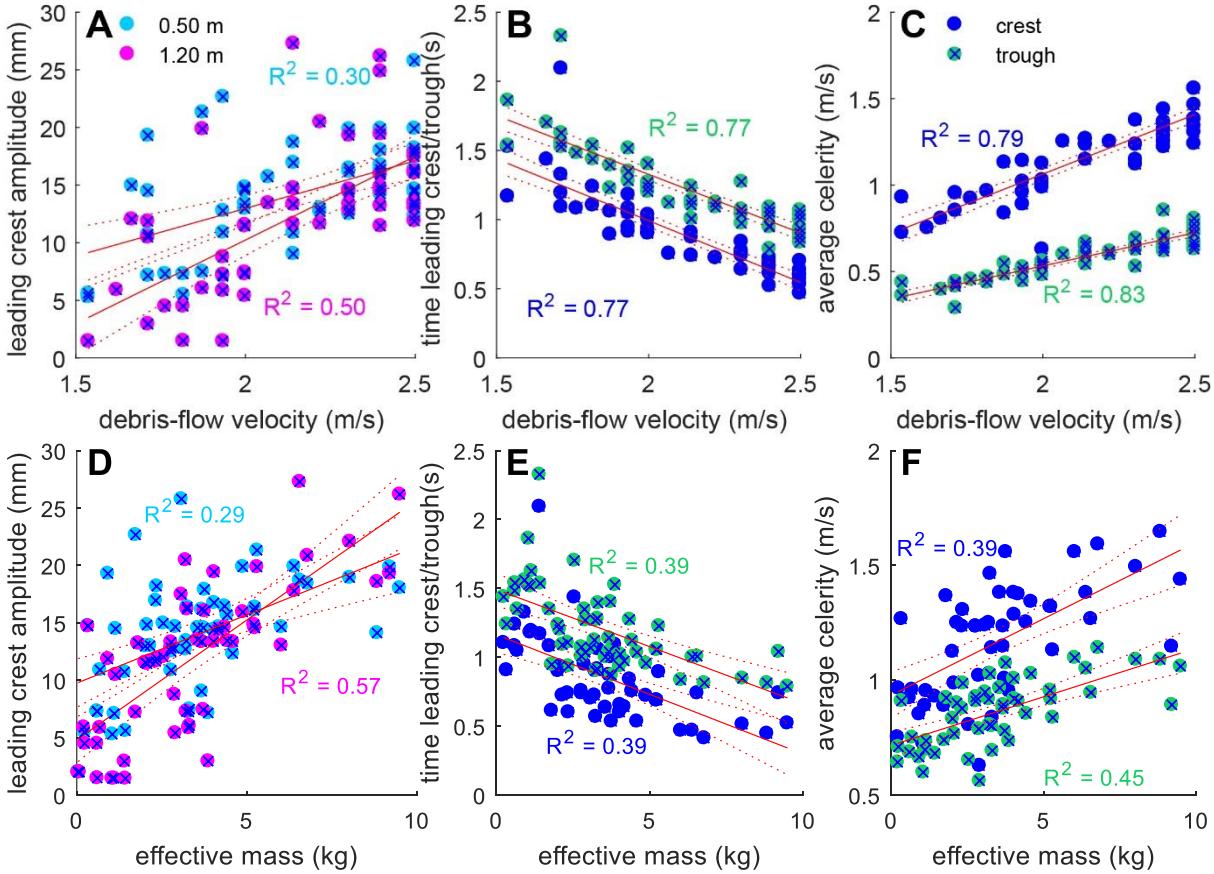

Figure 4.27. Debris-flow characteristics (velocity A, B, C) and effective mass (D, E, F) against various wave characteristics. **A)** and **D)** leading amplitude at x_b = 0.50 and 1.20 m (A: P = $1.33*10^{-5}$ and $1.12*10^{-9}$ for x_b = 0.50 and 1.20 m, respectively. D: P = $2.4*10^{-5}$ and $1.41*10^{-13}$). **B)** and **E)** time when leading crest/trough passes by x_b = 0.50 m (B: P=$1.7*10^{-18}$ and $1.59*10^{-18}$. E: P=$6.68*10^{-7}$ and $5.45*10^{-7}$ for crest and trough, respectively). **C)** and **F)** average celerity (C: P = 3.82^{-19} and 4.96^{-22}. F: P = 1.18^{-8} and 1.05^{-7} for crest and trough, respectively).

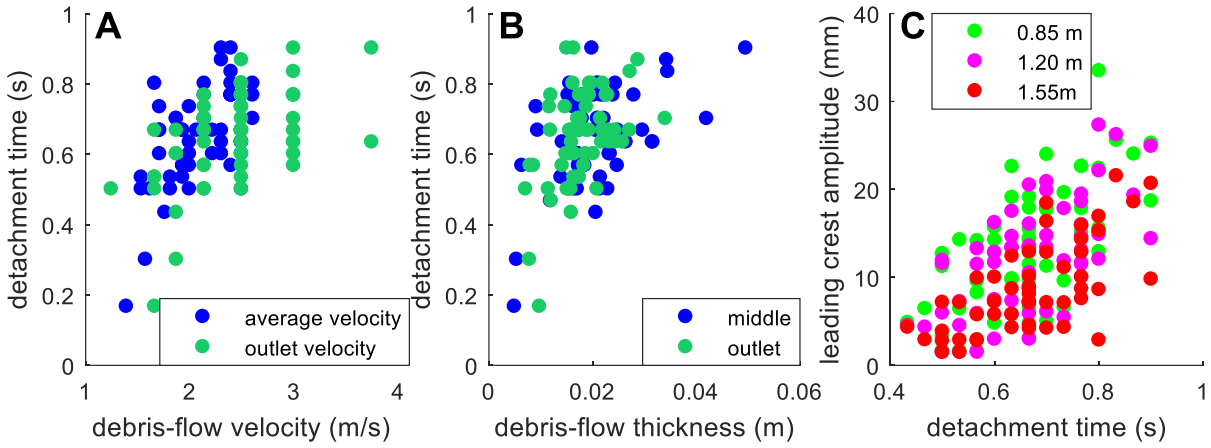

Figure 4.28. Relation between debris-flow and wave characteristics, and detachment time. **A)** detachment time against debris-flow velocity **B)** debris-flow thickness. **C)** first crest amplitude.

4.4.2 Debris-flow and wave energy

An increase in debris-flow energy leads to an increase in wave energy at x_b = 0.50 m (Figure 4.29A). On average, the wave energy is about 1-10 % of the debris-flow energy, and the efficiency of energy transfer decreases with increasing debris-flow energy (Figure 4.29B). Two outliers in this figure with a remarkably high wave energy, represent the run with the highest amount of gravel (64 vol%) and the lowest amount of clay (0 vol%). Both runs have a low outflow thickness and therefore a relatively low debris-flow energy. When the debris flows hit the water surface, no splash was heard. This indicates less turbulence and water entrainment, hence a more efficient energy transfer. The runs with a very high debris-flow energy represent the runs with the most amount of water (0.6 vol%) and the highest volume (16, 18 kg). Finally, the gravel run (40 vol%) with a debris-flow energy of 8.4 J has a very low corresponding wave energy. There is no physical explanation found for this, but as stated earlier, the gravel runs show a lot of unclarified scatter.

An increase in debris-flow energy leads to an increase in leading crest amplitude, initial celerity and average crest celerity (Figure 4.29). Wave energy is calculated using wave amplitude and displaced water mass (depended on its celerity) and its relation with debris-flow volume, composition and outflow slope is shown in Figure 4.8.

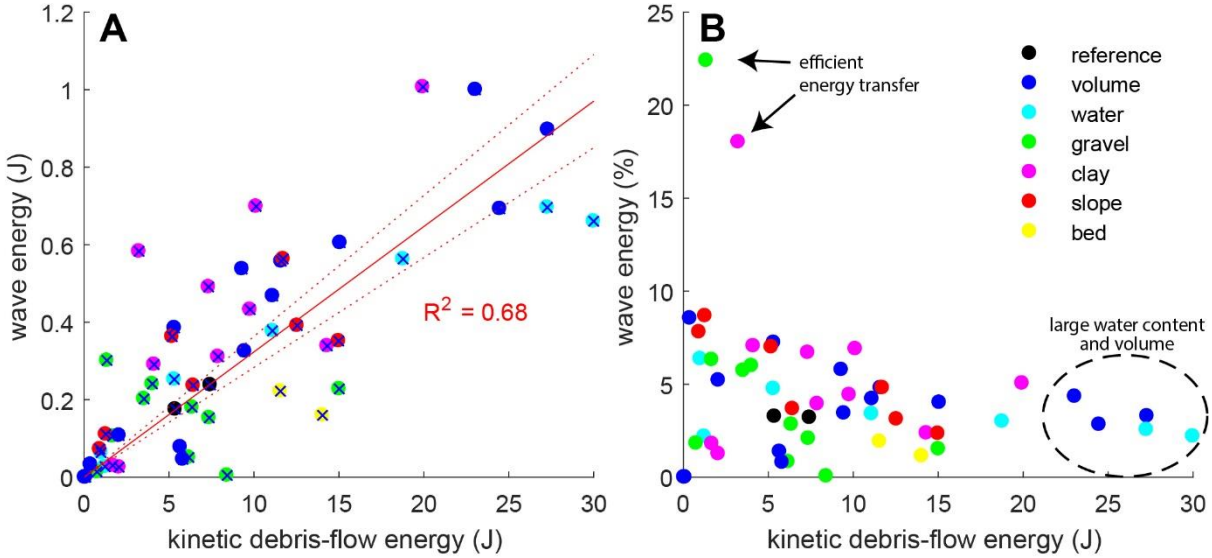

Figure 4.29. Debris-flow energy against wave energy in J (**A**) and % (**B**). The P-value of the linear relation in A is = $2.7*10^{-12}$.

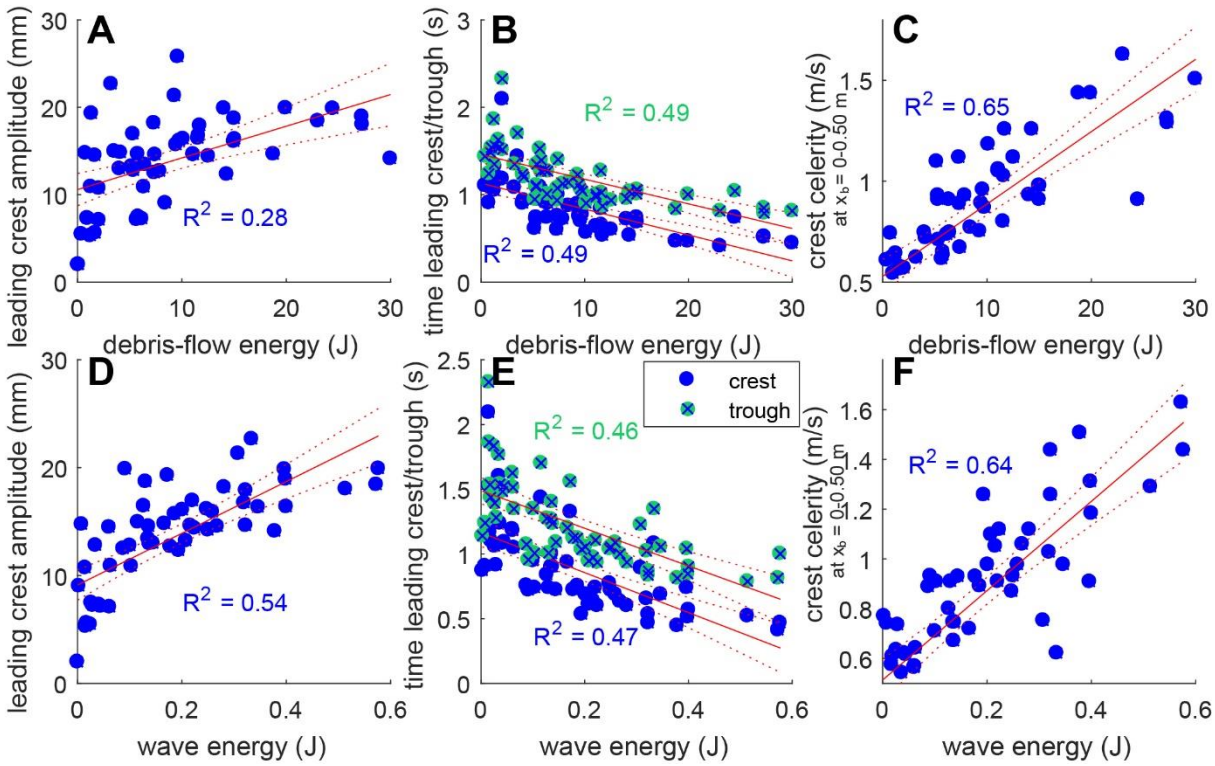

Figure 4.30. Wave and debris-flow energy against wave characteristics. Leading amplitude at x_b = 0.50 m (**A, D**), time of first crest/trough to pass by x_b = 0.50 m (**B, E**) celerity between x_b = 0-0.50 m (**C, F**). The P-values of the linear regression lines are A: p =2.69^{-5}, B: p = 7.57^{-9}, 1.02^{-8} (crest, trough), C: p = 7.45^{-14}, D: p = 9.58 $^{-11}$, E: p = 5.1^{-9}, 5.31^{-9} (crest, trough), F: p = 8.19^{-14}.

4.4.3 Debris-flow momentum

Debris-flow energy and momentum are calculated with the same input parameters, hence they are highly related (Figure 4.31). A larger debris-flow momentum results in a larger leading crest amplitude (Figure 4.32). This is especially true for x_b = 0.85-1.20 m, where the wave is fully developed and detached, and not yet dissipated or influenced by boundary effects such as reflection and refraction. The near-field crest and trough celerity are also related to momentum, just as wave energy, detachment time and wavelength. There is no relation with momentum and wave period. The momentum of the wave itself could not be determined such as was done with the wave energy, because the estimation of the wave mass is too inaccurate hence it does not give sensible results.

Forcing the relations in Figure 4.32 through the origin would be reasonable, however this does not match the relations found. Apparently, certain starting values or thresholds of the wave characteristic are present. For example, a small momentum input results in a wave celerity of 0.4 m/s, or the detachment time is always larger than 0.4 s (excluding the experimental runs for the lowest volume).

The majority of momentum is transferred almost immediately at impact (*Heller et al., 2016*). A higher momentum leads to a longer time till detachment, creating more powerful waves in terms of wavelength and amplitude (Figure 4.32), and a larger near-field non-linearity (not shown). A lower momentum results in more, smaller waves, because the debris flow does not have enough momentum to keep pushing the waves and detachment occurs. Especially for the runs with the lowest mass (3.5 kg), only small capillary ripples formed and there was not such a thing as detachment. These runs are indicated with an open circle in Figure 4.32E.

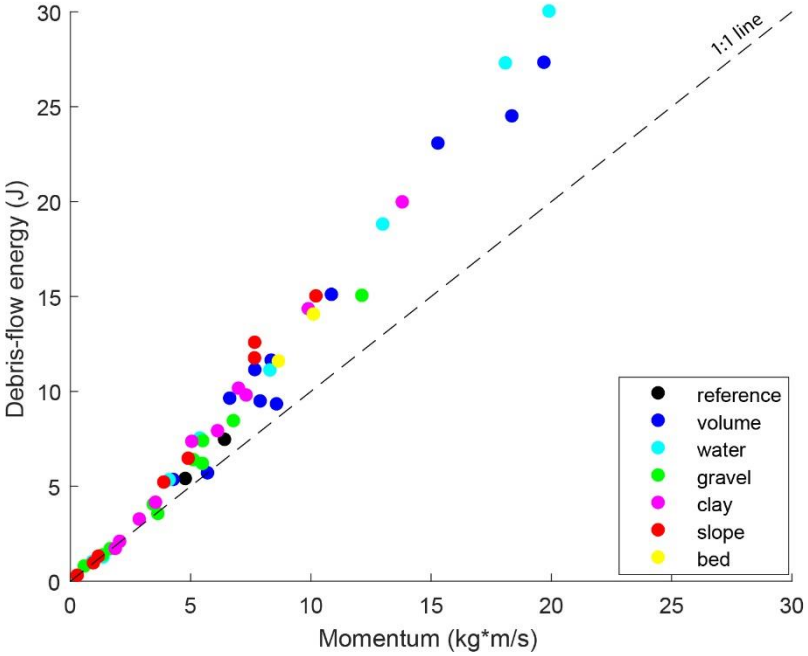

Figure 4.31. Debris-flow energy against debris-flow momentum, with a 1:1 line.

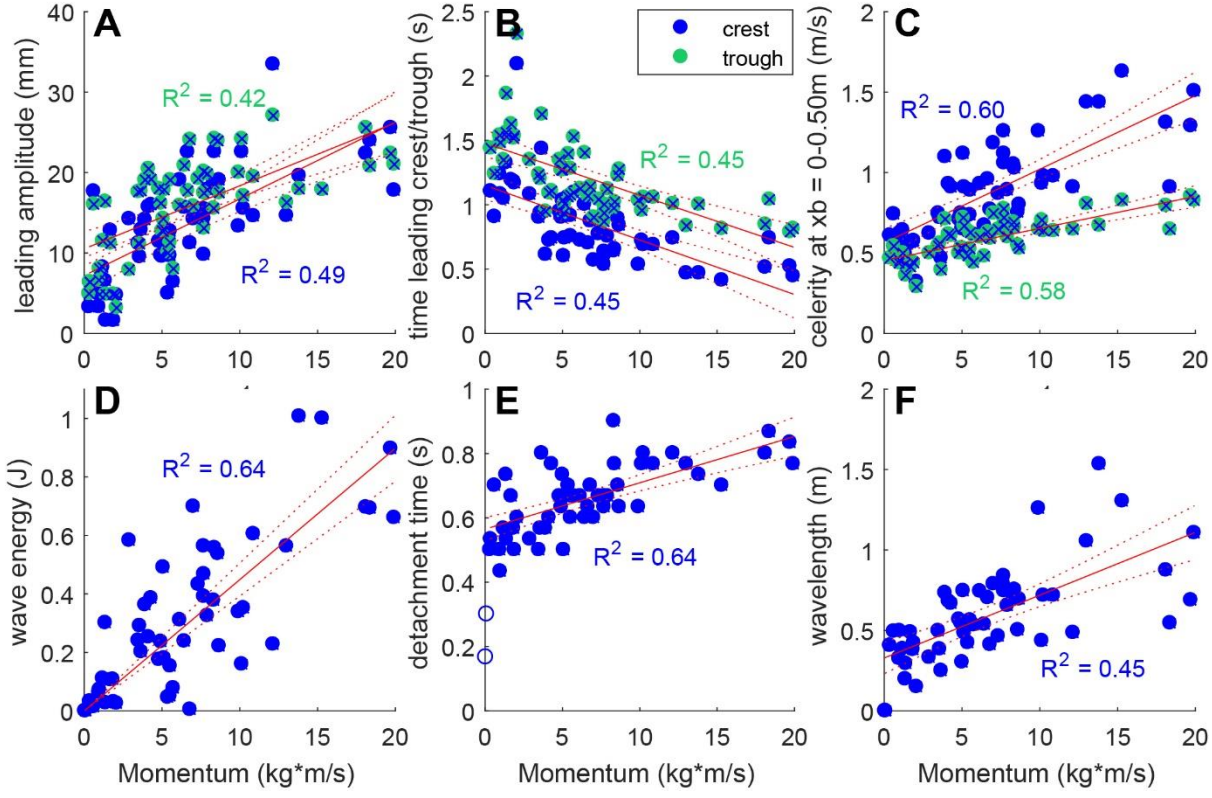

Figure 4.32. The relation between debris-flow momentum and wave characteristics. **A)** leading amplitude at x_b = 0.85 m (p= 2.7 * 10^{-9}, 7.1 * 10^{-8} (crest, trough), **B)** travel time of first crest/trough to pass by x_b = 0.50 m (p = 3.6 * 10^{-8}, 3.2 * 10^{-8} (crest, trough)). **C)** celerity between x_b = 0-0.50 m (p = 7.62 * 10^{-12}; 3.65 * 10^{-11} (crest, trough)). **D)** wave energy (p = 1.4 * 10^{-11}). **E)** detachment time, with the lineair relation forced trough zero. The open circles indicate runs with the lowest volume, resulting in capilary ripples without a sensible detachment time (p = 2.0 * 10^{-8}). **F)** wavelength at x_b = 0.50 m (p = 1.3 * 10^{-8}).

4.4.4 Summary influence of debris-flow on impulse wave

An increase in debris-flow volume leads to an increase in debris-flow thickness and velocity. Correspondingly, the wave amplitude is increased. An increase in water content leads to a faster debris flow. Similar observations are done for an increase in clay content, until a certain threshold when the flow becomes too viscous. The gravel content does not show a relation with the wave characteristics. A faster debris flow results in a higher wave celerity. An increase in outflow slope results in higher and faster waves, until the difference between the outflow slope and the wave basin becomes too large and energy is lost during this transition. The characteristics of the debris flow and waves are summarized in the parameters energy and momentum, which show the same correlations as the parameters they are derived from.

5. Discussion

The results will be interpreted and compared to literature (5.1), where after the applicability of previously developed predictive equations will be assessed (5.2). Next, the influence of scaling in this research is discussed (5.3) and this chapter ends with a short note about the practical impact (5.4) and recommendations for further research (5.5).

5.1 The influence of debris-flow characteristics on impulse waves

The different experimental runs, varying in volume, composition and slope, result in different debris-flow characteristics in terms of velocity, thickness and weight. It is clear that near-field crest amplitude and detachment time are not fully related to any of the debris-flow features (Table 5.1). The other relations are stronger ($R^2 > 0.5$) for at least one debris-flow parameter. Debris-flow velocity shows the strongest relation to travel time, crest celerity and wavelength. Both debris-flow energy and momentum are relatively well correlated to the wave characteristics. Debris-flow thickness and weight are not correlated, but a relatively stronger correlation with effective mass is present.

Debris-flow velocity turns out to be the best general predictor for wave characteristics (Table 5.1). Average wave celerity is about 0.5 times the average debris-flow celerity during outflow. This allows the water to be pushed up by the debris flow, which takes much less time than the time to wave detachment. The larger the difference between the velocity and celerity, the more the water will be pushed up before wave release. The relation between debris-flow velocity and wave amplitude decreases with increasing distance from the impact area, where the wave becomes less over-steepened. However, the relation with debris-flow velocity and wave celerity decreases with increasing distance from the impact area, indicating that the debris-flow velocity is a direct cause for the wave celerity.

Besides flow velocity, both debris-flow energy and momentum are relatable to the wave characteristics. This finding is in agreement with other studies (e.g. *Fritz et al., 2004; Mulligan & Take, 2017*). Both parameters are a measure of debris-flow effective mass and velocity. Intuitively, these two parameters are the most important for wave generation and evolution. Momentum is indeed the best parameter to predict (far-field) wave amplitude. The combined effect is however not always better than assessing the debris-flow velocity only. As shown in chapter 4.2.4, debris-flow velocity is mostly determined by water and clay content, which both can be a lubricant for the flow. It is therefore an important conclusion to state that debris-flow composition does matter for tsunami assessment.

The strength of the relation can give an indication to which extend the variable can be used for prediction. For example, the debris-flow velocity will be a relatively good parameter for estimating the average crest velocity. One could argue that the R^2-values are relatively low to generate a significant conclusion. However, it should be realized that the amount of natural scatter (see Figure 4.1), gives an indication of the expected strength of the relations. By composing relations out of completely different types of debris flow, as much scatter as possible was created. Still, relations can be drawn. Logically, the relations are much stronger when dealing with just one experimental set (for example, water content variations). This is however out of the scope of this thesis, which tries to obtain general understanding of all types of debris flows, because of its relevance in practice.

Debris flow → Waves ↓	**velocity**	**effective mass**	**energy**	**momentum**
leading crest amplitude at x_b = 0.50 m	0.30	0.29	0.28	0.49
leading crest amplitude at x_b = 1.20 m	0.50	0.57	0.58	0.60
travel time of leading crest to x_b = 0.50 m	0.77	0.39	0.49	0.45
average crest celerity	0.79	0.39	0.65	0.60
wave energy at x_b = 0.50 m	0.53	0.53	0.68	0.64
detachment time	0.30	0.50	0.40	0.47
wavelength at x_b = 0.50 m	0.64	0.39	0.50	0.45
predictor strength	0.55	0.44	0.51	0.53

Table 5.1. R^2 values (indicating linear correlation) of debris-flow characteristics and the corresponding wave characteristics. The darker the green color, the stronger the correlation. The slope of the linear regression lines can be found in Appendix 2, Table A2.3.

Distinctive characteristics of this study are the addition of water to the debris-flow mixture, the varying sediment composition of the debris flow, the sloping bed of the wave basin and the 3D wave propagation. Altogether, this research is a start of experimenting with a less idealized, more realistic, world. The findings of this research are compared with other studies in more detail, see Table 5.2 and 5.3. The relative wave period is somewhat low compared to other studies, while the celerity is remarkably larger. This indicates a relatively strong pushing effect of the debris flow, which might be related to the 10° slope of the wave basin, causing a longer detachment time compared to studies with a horizontal basin slope.

The paper of *de Haas et al. (2015*) is the only research dealing with debris-flow composition variations (for subaerial debris flows). Our results regarding water and clay content do follow *de Haas'* findings. Water acts as a lubricant for the flow and an increase in clay content has the same effect, most likely due to the better retained excess pore pressure (*de Haas et al., 2015*). Contrarily to their research, there was no trend between gravel content and debris-flow or wave characteristics. They found that at a small gravel content the levees where insignificant, promoting lateral spread instead of longitudinal growth, while a large gravel content caused increased gravel accumulation at the flow front, reducing runout distance. Three hypotheses are put forward to explain the absence of this trend. First, when increasing the gravel content, more material stays behind on the outflow slope and the tail of the debris flow is thicker. This will cause a relatively lower momentum transfer than predicted. Second, the size of the gravel is relatively large compared to the outflow slope width (2-5 mm and 12 cm, respectively). This could cause the grains to collide more often and loosing energy by friction. Finally, the volume used in this set of experiments is larger than in *de Haas et al. (2015*) (8kg instead of 6kg). This might impede the accumulation effect in the flow front. Also, the relation with outflow slope is not in agreement with their findings. A steeper slope causes a faster debris flow and waves with a higher amplitude and celerity. However, at an outflow slope of 40° the aforementioned factors decrease compared to a 35° angle. This is either a random expression of natural variability, falling within the error margin, or an indication that the debris flow loses energy during the transition of a 40° outflow slope to a 10° slope of the wave basin. This is reflected in the subaerial deposit showing a wide deposit near the impact area. This is however not seen in the subaqueous deposit.

In *Fritz et al. (2004*), the amplitude of the maximum crest always matched or exceeded the maximum trough amplitude, which is also true in our research. However, when looking at the leading crest and trough amplitudes, this is not the case. At x_b = 0.50 m, 73% of the time the leading trough amplitude is larger than the leading crest amplitude. This percentage decreases to 70, 45 and 20 % at x_b = 0.85, 1.20 and 1.55 m, from which follows that in the far-field, the crest amplitude is dominant. In agreement with *Fritz et al. (2004*) findings, the wave period could not be linked to the debris-flow characteristics or volume of displaced water.

A tsunami wave in deep water travels as a dispersive, non-linear wave, where the dispersion ($u^2 = h^2/ \lambda^2$) and the non-linearity (here expressed as $\epsilon = H/h$) are in the same order of magnitude (*Madsen et al., 2008*). This is also found for the far-field waves in this research. A tsunami wave in deep water travels with a constant wavelength and amplitude, and only starts to deform (decreasing period and increasing non-linearity) when approaching shallower water (*Hammack, 1973*). In deep water, the wave celerity is influenced by its period, following the deep water equation (equation 2.8A). It is therefore expected that the created impulse waves in this research, gradually will 'recover' from the over steepening and acceleration caused by the imposed impulse, and will ultimately reach a constant period, celerity and wavelength.

Wave amplitude, celerity and shape are reflected in the wave energy. In the current study, 0.1-22 % of the debris-flow energy is transferred to the waves. This is in agreement with values found in previous studies (e.g. *Mohammed & Fritz, 2016* found 1-24 %). *Heller & Hager (2011*) argue that energy transition during impact is more efficient if the water splash is relatively small and limited air is entrained. Furthermore, the impact with the channel bottom plays a role in their research, but this is negligible in this study due to the sloping bottom. Presumably only at an outflow slope of 40°, the impact with the channel bottom results in energy 'loss', and correspondingly lower energetic waves.

Momentum was found to be the most important characteristic for wave amplitude prediction by *Mulligan & Take (2017*). The majority of the momentum and energy is transferred almost instantly at the impact (*Heller et al., 2016*). Secondary waves are formed if the momentum transfer of the debris flow to the water is not large enough to oppose the restoring force of gravity. Debris flows with a small momentum will therefor result in multiple smaller waves, while larger momentum flows will generate one larger wave. Although theoretically the concept of momentum provides a good explanation of impact of 2D near-dry granular slides, it appears not to be the strongest predictor in this research (see 5.2.3 for elaboration on momentum as predictor for wave amplitude). The wave basin slope of 10° could lead to a longer detachment time and thus a larger momentum transfer. The longer detachment time could increase the importance of debris-flow velocity as predictor for wave characteristic.

reference	*this study*	*Fritz et al., 2004; Heller & Hager, 2010; Heller & Hager, 2011;*	*Mohammed & Fritz, 2012*	*Heller & Spinneken, 2015*	*McFall & Fritz, 2016*	*Mulligan & Take, 2017; Miller et al, 2017*
type of debris flow	granular, varying grain size, saturated	granular, constant grain size, forced velocity and thickness	granular, varying grain size, forced velocity and thickness	rigid PVC-slides, forced velocity and width	granular, 2 sediment types	granular, constant grain size
2D/3D	3D	2D	3D	2D, 3D	3D	2D
scale outflow slope	2.0 x 0.1 m 20-40°	3.0 x 0.5 m 45°	9.3 x 1.2 m 27°	21.0 x 0.6 m 45°	9.3 x 1.2 m 27°	6.7 x 2.1 m 30°
scale wave basin	1.9 x 0.9 m with sloping bed (10°)	11.0 x 0.5 x 1.0 m	48.8 x 26.5 m	20.0 x 7.4 m	48.8 x 26.5 m	33.0 x 2.1 m
water depth	0 - 0.33 m (sloping)	0.30, 0.45, 0.68 m	0.30, 0.60, 0.90, 1.20 m	0.24, 0.48 m	0.30, 0.60, 0.90, 1.20 m	0.05 - 0.50 m
parameter variations	DF volume, DF composition, outflow slope	water depth, DF-velocity, DF- thickness	water depth, DF volume	water depth, DF volume	shape of outflow slope, sediment type, water depth, volume	water depth, DF volume

Table 5.2. Summary of methods of various comparable studies.

		this study [a]	*Fritz et al., 2004*	*Heller & Hager 2010, 2011*	*Mohammed & Fritz, 2012*	*Heller & Spinneken, 2015*	*McFall & Fritz, 2016*	*Mulligan & Take, 2017; Miller et al, 2017*	*Natural debris flow and wave* [b]
debris-flow velocity [m/s]	u_s	1.00-3.74	-	2.06-8.77	-	0.94-3.79	-	2.5-4.8	0.01-1 [c]
relative debris-flow height [-]	h_s/h	0.03-0.24	0.07-0.6	0.09–1.64	0.1-0.9	0.25-0.5	0.08-0.46	0.07-0.7	0.005-0.5 [c]
relative wave amplitude [-]	a_c / h	0.01-0.2	0.05-1.3	<2.5	<0.38	0.003-1.23	0.001-0.35	0.2-2.5	1-10 [d e]
relative wave celerity [-]	$c\sqrt{gh}$	4.9-12.7	0.3-2.5	-	0.7-1.2	~0.5-1.5	0.70-1.3	4.0-11.5	<~19 [f]
relative wave period [-]	$T\sqrt{g/h}$	3.62-7.9	6-22	~1-40	6-26	6.1-31.3	2-22	-	~2.6 [f]
Froude number [-]	Fr (eq2.1)	1.4-2.6	~1.0-4.8	0.9-6.8	1-4	0.5-2.5	1.0-3.9	~0.2-4.8 [a]	1-4 [g]
Ursell number [-]	U (eq2.5)	0.01-95	1-22	$2.7\text{-}10^4$	0.2-55	$0.5\text{-}10^3$	0.01-55	-	-
wave type	Figure 2.8	sinusoidal, stokes, cnoidal?	stokes, cnoidal, solidary, bore	stokes, cnoidal, solidary, bore	stokes, cnoidal	-	-	solidary, bore	-

Table 5.3. Parameter values found in various comparable studies. Values are taken or calculated form the source in the header, unless specified otherwise in the footnotes. [a]calculation of relative values by using h=0.165 m. [b] calculation of relative values by using h=20m. [c] *Iverson (1997)*. [d] *Hermanns et al. (2004)*. [e] *Bussman & Anselmetti (2010)*. [f] Goff & Chauge-Goff (2014) [g] *Mcfall & Fritz (2016)*.

5.2 Applicability of predictive equations

In this section is studied to which degree the experimental output fits the previously conducted, more idealized, impulse wave predictors is applicable to this research.

5.2.1 Froude number and breaking waves

The Froude number is the dimensionless form of the impact slide velocity divided by the wave celerity. It is generally determined following equation 2.1. In this research, this equation is adapted by using the measured celerity instead of the predicted celerity following c = $\sqrt{gh}$, since this predictive formula is not directly applicable on the data (see section 5.2.2). When correcting the average debris-flow velocity for the angle of the outflow and wave basin slope, the Froude number reads as follows:

$$Fr_m = \frac{u_s \frac{cos\alpha}{cos\theta}}{c_{c1}} \quad (5.1)$$

Mulligan & Take (2017) corrected this Froude number by accounting for slide thickness relative to water depth, and bulk density differences between the sliding material and the water. This can again be used in two forms, using the measured or the predicted value for the wave celerity (resulting in $Fr_{d,m}$ and F_d, respectively).

$$Fr_{d,m} = \frac{u_s \frac{cos\alpha}{cos\theta}}{c_{c1}} * \sqrt{\frac{h_s}{h} * \frac{\rho_s - \rho}{\rho}} \quad (5.2)$$

The different ways of calculating the Froude number results in different parameter values (Table 5.4 and Figure 5.1). The Froude number calculated with the theoretical crest celerity results in higher values than calculated with the measured average crest celerity. Correcting the Froude number for water depth and density differences results in a significant lowering of the number. The Froude numbers (following equation 2.1) found in comparable studies are highly variable and range between 0.2 - 6.8, this study included (Table 5.3).

Mulligan & Take (2017) state that for $Fr_d > 1$ supercritical conditions occur, resulting in a breaking bore. When submerged, the debris flow slows down until $Fr_d = 1$ where after the wave is released. For $Fr_d < 1$, the debris flow still pushes the water, however the wave celerity exceeds the debris-flow velocity. This causes a non-breaking wave travelling away from its source region. Hence, at $Fr_d = 1$, the largest wave amplitude can be formed. However, in the current research, no breaking occurs although occasionally Fr_d or $Fr_{d,m}$ exceeds 1. This opposes the studies of *Miller et al., (2016)* or *Heller & Hager (2010)*. The explanation of the absence of breaking waves can be found in the sloping bed of the wave basin. Waves which are about to break, travel to deeper water and therefore breaking does not occur for the range of parameters used in this study.

Froude number	**equation**	**min**	**max**	**mean**	**% Fr ≥ 1**
theoretical	Fr (eq 2.1)	1.39	2.60	2.12	100
measured	Fr_m (eq 5.1)	1.33	2.80	1.64	100
theoretical corrected	Fr_d (eq 5.2 with $c_{c1} = \sqrt{gh}$)	0.48	1.38	0.98	50
measured corrected	$Fr_{d,m}$ (eq 5.2)	0.59	1.06	0.77	3.3

Table 5.4. Four different ways of calculating the Froude number and the corresponding parameter ranges of this research.

Besides predicting wave breaking, the Froude number is an important number for prediction of wave amplitude and wave shape (see section 5.2.3 and 5.2.4). The choice of equation to calculate the Froude number is very important for the outcome of these predictive formulas. Figure 5.2 shows the Froude number for varying debris-flow mass, composition and outflow slope. An increase in mass leads to an increase in Froude number for all ways of calculating except for Fr_m, which shows a decreasing trend. An increase in water content leads to an increase in Froude number when using the calculated celerity, but a decrease in Froude number for the measured celerity. These opposing trends show the importance of choosing the appropriate way of calculating the Froude number.

A short note about hydroplaning should be added. According to literature (see section 2.2), hydroplaning occurs for Fr < ~0.3. Hydroplaning does not occur in this study, having a too coarse grain size and a too large Froude number. The existence of outrunners in the debris-flow deposit could be explained by the coarse grains being pushed out of the water by turbulence (Figure 4.20B), therefore occurring in the upper layer of the water for a longer period of time, increasing the settling time. I refer to the MSc thesis of *N. Santa (in progress*) for a more detailed analyses.

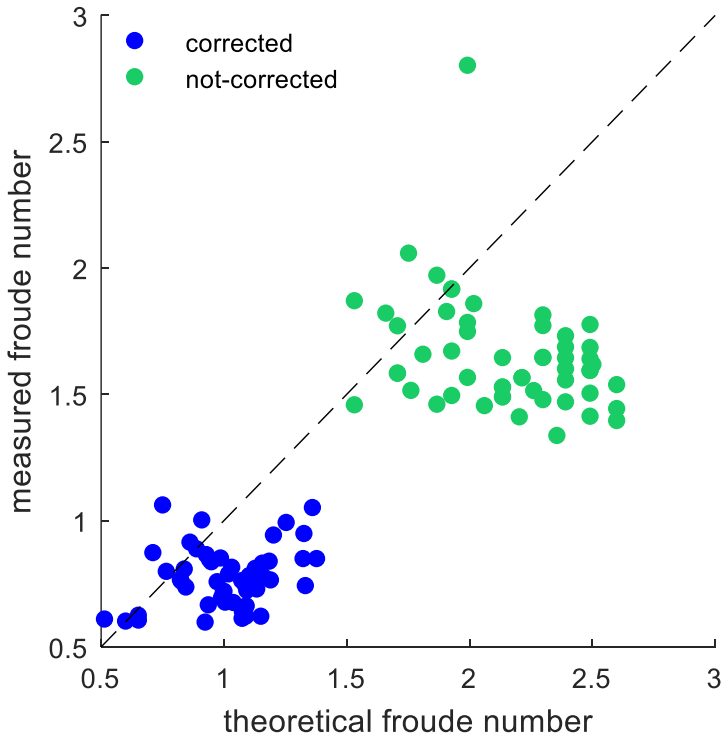

Figure 5.1. Different calculations of the Froude number. Theoretical Froude number (Fr and Fr_c) against measured Froude number (Fr_m and $Fr_{d,m}$) for corrected and non-corrected values.

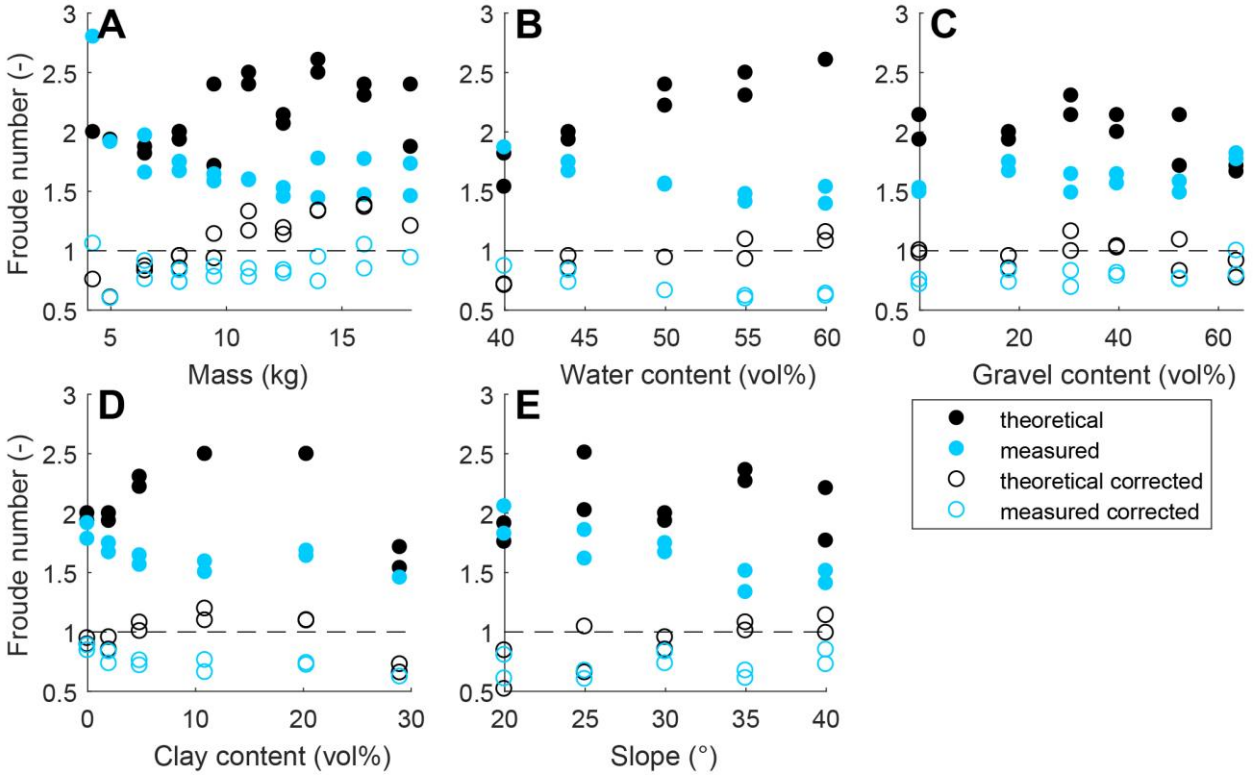

Figure 5.2. The influence of mass, debris-flow composition and slope on the Froude number.

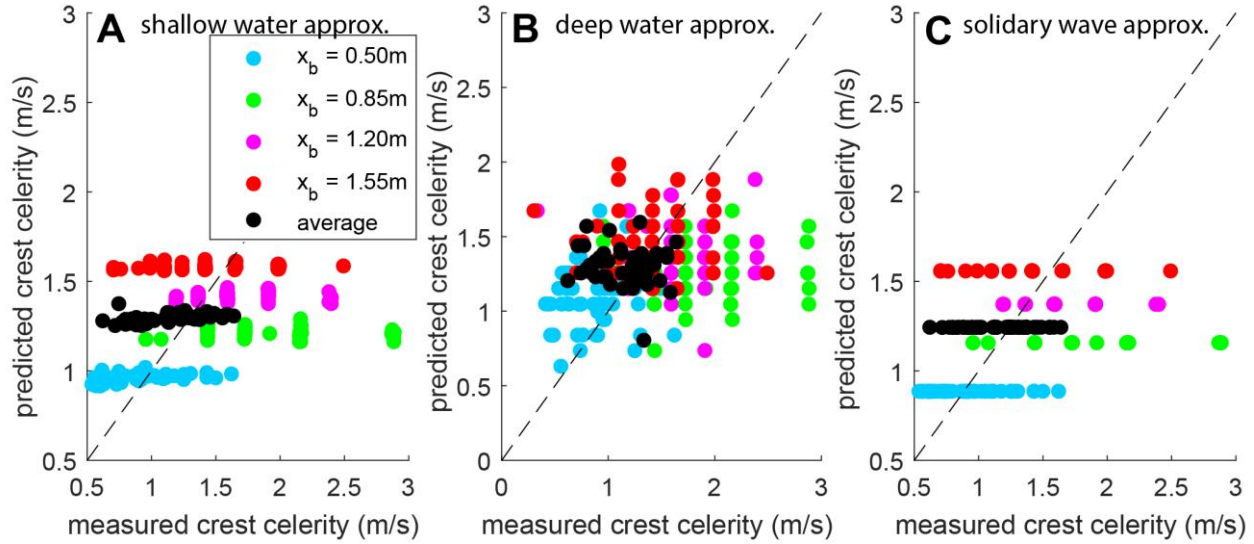

Figure 5.3. Different predictions of celerity compared with the measured crest celerity. **A)** shallow wave equation. **B)** deep water equation. **C)** solidary wave equation.

5.2.2 Prediction of celerity

Wave celerity is commonly predicted using equation 2.8a for deep water, 2.8b for shallow water, or equation 2.9 for solidary waves. However, these equations are not always applicable to debris-flow generated tsunami waves, since the pushing of the debris flow causing the celerity to exceed the predicted value. In *Mohammed & Fritz (2012*), the first wave crest follows the solidary wave approximation, while in *Miller et al. (2017*) only the bores in the far-field match this celerity.

In this research, the measured crest celerity is much more variable than calculated with shallow water approximation and solidary wave approximation (Figure 5.3). The celerity predicted with deep water approximation is much more variable, because the measured (thus variable) period is included in the equation. The large variability in measured celerity is caused by the different types of debris flows, with each its distinct velocity and thickness. This causes wave celerity not to be a simple function of water depth or wave period. It is therefore not possible to predict wave celerity from these well-known formulas, rather debris-flow characteristics such as velocity should be used.

5.2.3 Prediction of wave amplitude

There are various approaches to predict wave amplitude. *Fritz et al. (2004*) performed 2D granular rock slide experiments, for varying water depths and different debris-flow masses. They applied multiple regression for the wave crest amplitude, resulting in:

$$\frac{a_c}{h} = 0.25\ Fr^{1.4} \left(\frac{h_s}{h}\right)^{0.8} \tag{5.3}$$

Heller & Hager (2010) performed 211 experiments, in which they forced the acceleration of the granular material. They varied water depth, landslide velocities, slide thickness and slope. Their empirical relation is based on the impulse product parameter, and both landslide thickness h_s and mass m are taken relatively to still water level.

$$P = Fr \left(\frac{h_s}{h}\right)^{0.5} \left(\frac{m_s}{\rho b h^2}\right)^{0.25} \cos\left(\frac{6\alpha}{7}\right)^{0.5} \tag{5.4}$$

$$\frac{a_c}{h} = \frac{4}{9} P^{0.8} \tag{5.5}$$

This prediction is improved by *Miller et al. (2017*) by implementing the effective mass instead of the total mass. They state deviations from this equation can be either due to scale effects, or due to other mechanisms like breaking.

The prediction of *Mulligan & Take (2017*) is based on hydrodynamic and hydrostatic momentum transfer. This leads to an analytical equation of the near-field maximum wave amplitude in a 2D-wave field, based on landslide properties. The equation is developed for (near)dry granular landslides, which are less mobile than debris flows. *Mulligan & Take (2017*) expect that the underlying assumption of momentum transfer is not applicable to debris flows due to their high mobility, and therefore to be not/less applicable to this research. This formula is simplified by estimating the length and time scales until detachment. In addition, the wave celerity is estimated with $c = \sqrt{gh}$. The maximum wave amplitude is furthermore limited by wave breaking limit ($a_c/h = 0.78$) and the fluid continuity limit.

$$a_c = \sqrt{h^2 + \frac{\rho_s h_s (u_s \cos\alpha)^2}{\rho g}} - h \qquad (5.6)$$

$$\frac{a_c}{h} = \frac{h_s u_s \cos\alpha \, \Delta t_{eff}}{h L} + 1 \qquad \text{fluid continuity limit} \qquad (5.7)$$

L = distance the landslide travels until detachment [m].

The choice of the Froude number calculation is very important for the amplitude prediction. I choose to follow *Mulligan and Take (2017*) using Fr_d, which gives the best fit possible. Furthermore, the relation of Fr_c and maximum crest amplitude is the best (R^2 = 0.62). The second challenge of applying the equations to this research, is the estimation of the water depth. The sloping bed of the wave basin results in a gradually increasing water depth. Furthermore, *Heller et al. (2008*) state that water depths shallower than h = 0.2 m might be influenced by scale effects

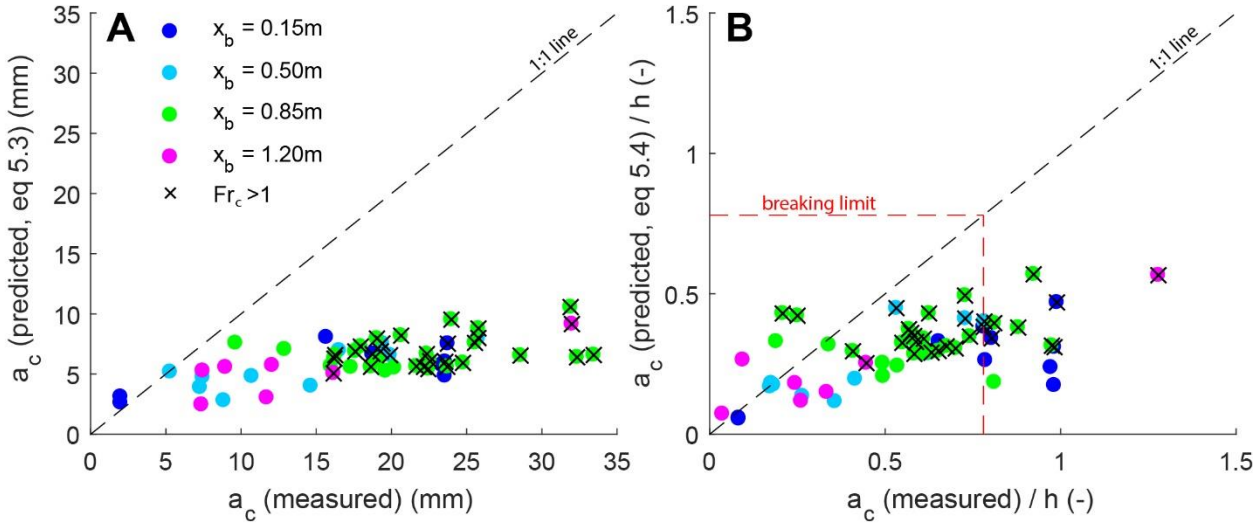

Figure 5.4. Prediction of maximum crest amplitude against the measured amplitude. Both predictors are calculated with h = 0.079 at x_b = 0.50 m. **A)** equation 5.3 (*Fritz et al., 2004*). **B)** equation 5.4 (*Heller & Hager, 2010*).

The wave amplitude predictors of *Fritz et al. (2004*) (eq 5.3) and *Heller & Hager (2010*) (eq. 5.4) are shown in Figure 5.4. The predicted value of a_c in this figure is calculated using a water depth of 0.079 m at x_b = 0.5 m, because detachment occurs at approximately this location. However, for both predictors, the choice of the water level (ranging between h = 0.02-0.33 m) does not influence the strength of the predictor. Figure 5.4A is shown in its dimensional form, to avoid the use of an arbitrary chosen water level. In all cases, the predictor underestimates the maximum crest amplitude. Figure 5.4B is shown in its non-dimensional form, avoiding the conversion of equation 5.4 to its dimensional form using the water depth. The measured amplitude is the largest amplitude measured at any time at any location during the experimental run, divided by the water depth at that specific location. The location of maximum crest amplitude is indicated with a color. For small water depths, the predictor overestimates the crest amplitude, while it under predicts the amplitude for lager measured amplitudes. In general, both predictors perform relatively poor.

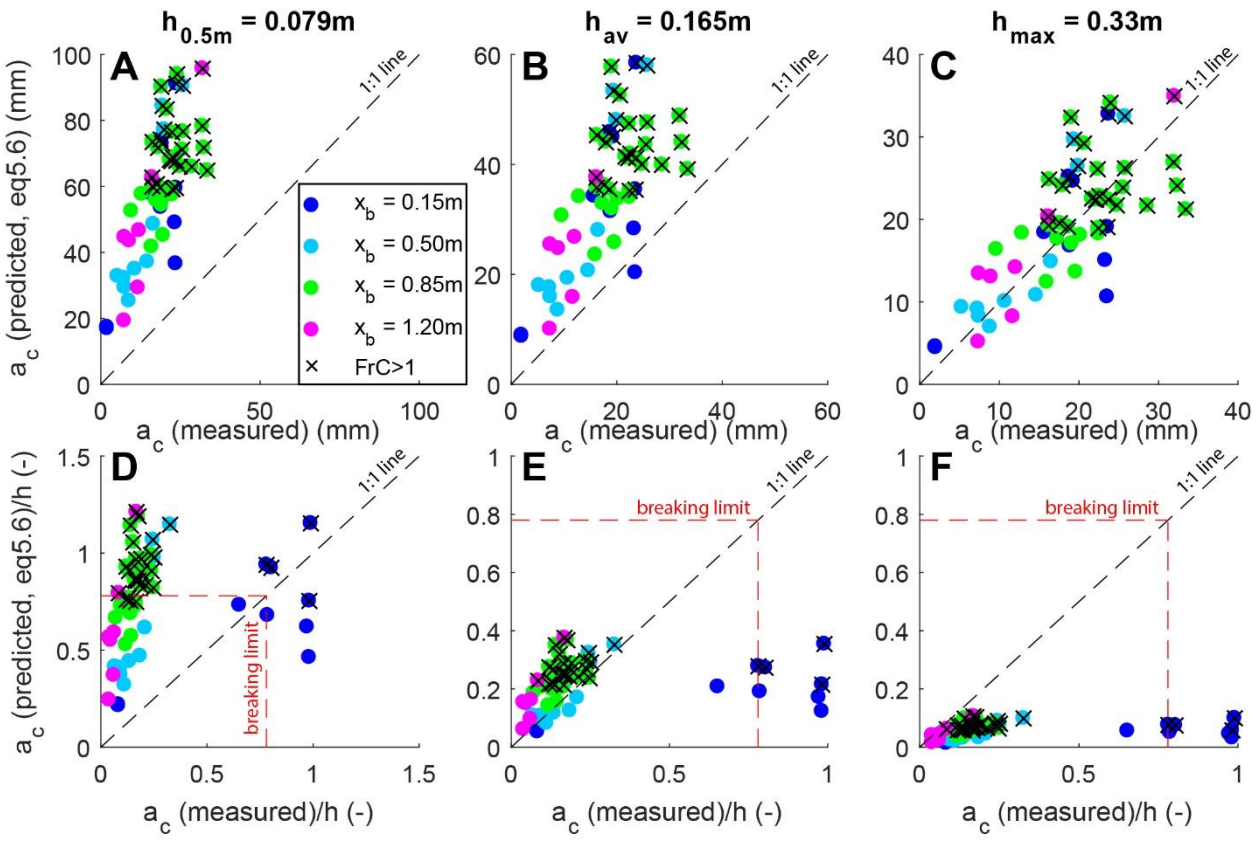

Figure 5.5. Prediction of maximum crest amplitude against the measured amplitude with equation 5.6 for different water depths (left, middle, right), in its dimensional (A, B, C) and non-dimensional form (D, E, F). C: $R^2 = 0.54$, $p=1.08*10^{-10}$

The applicability of the amplitude predictor of *Mulligan and Take (2017*) is shown in Figure 5.5. The wave amplitude is presented in its dimensional (A, B, C) and non-dimensional form (D, E, F). The amplitude is made non-dimensional by dividing it with the corresponding water level.

The applicability of the equation of *Mulligan and Take (2017*) is highly dependent on water depth (Figure 5.5). Unfortunately, parametrization of the variable water depth is one of the challenges by comparing this study to other studies with a constant water depth. When predicting wave amplitude with the water depth at the approximate detachment location x_b = 0.50 m, the predictor highly overestimates the wave height (Figure 5.5A, D). The predictor now shows that a $Fr_d > 1$ occurs only above the breaking limit, confirming the hypothesis of *Mulligan & Take (2017).* Possible explanations for the over estimation can be the 3D character of this study, or the different interaction between a water-saturated debris flow entering the basin (this study) or a dry-granular debris flow.

When setting the water depth to the average value of h = 0.165 m (Figure 5.5B, D), the dimensional form still shows an over prediction, while the non-dimensional form is more or less accurate, with the exception of outliers with a relatively large a_c/h, due to the small water depth at location x_b = 0.15 m. Entering the maximum water depth of this setup, h = 0.33 m, the dimensional form of the predicted and measured crest amplitude coincide relatively well ($R^2 = 0.54$), but the non-dimensional form shows a large under prediction (Figure 5.5C, F). Figure 5.5C is however not in accordance with *Mulligan & Take's (2017*) findings, where the predictor provides an upper limit for crest amplitude. The average water depth of h = 0.165 m therefore seems to be the best fit.

Summarizing, it can be said that the amplitude predictor of *Mulligan & Take (2017*) does show a clear correlation with this experimental data. It shows that the assumption of momentum exchange is also valid for saturated debris flows, contrary to *Mulligan & Take's (2017*) constraints. However, the correct fit results from using the average water level, indicates that future work to further elucidate the effect of a sloping wave basin bed, is warranted.

5.2.4 Prediction of wave shape

The shape of the waves in this research are difficult to observe during the experiments or from the given wave profiles. Intuitively, the waves are sinusoidal or cnoidal waves. The previously defined impulse product parameter (equation 5.4) is not successful in classifying waves, hence *Heller and Hager (2011*) provide an empirical predictor determining wave type, from slide thickness, volume and density, impact angle and water depth. This predictor, called the wave type product T_p (*Heller et al., 2009*) is defined:

$$T_p = \left(\frac{h_s}{h}\right)^{1/3} \left(\frac{m_s}{\rho b h^2}\right) \cos\left(\frac{6\alpha}{7}\right) \quad (5.8)$$

$T_p < \frac{4}{5} Fr^{-7/5}$ Stokes-like waves (5.9)

$\frac{4}{5} Fr^{-7/5} \leq T_p \leq 11\ Fr^{-5/2}$ cnoidal- or solitary-like waves (5.10)

$T_p > 11\ Fr^{-5/2}$ bore-like waves (5.11)

Equation 5.8 is in this study adapted to:

$$T_p = \left(\frac{h_s}{h}\right)^{1/3} m_{eff} \cos\left(\frac{6\alpha}{7}\right) \quad (5.12)$$

According to *Heller & Hager (2011)*, impulse waves change their type over a short distance due to energy dissipation and air detrainment. In their research, relative grain diameter has a negligible effect on wave type, and landslide Froude number and relative slide mass are dominant. The Froude number is calculated using the water depth at the approximate point of detachment (h=0.079 m, x_b = 0.50 m) and the average water depth (h = 0.165 m, x_b = 0.93 m). As well Fr (used in the research of *Heller & Hager, 2011*) as Fr_d (used for the prediction of wave amplitude, section 5.2.3) are compared. The wave type product T is calculated using the effective mass instead of the relative mass, following equation 5.12. Figure 5.6 shows the predicted wave shape for different values for h and Fr. Clearly, the wave shape prediction is sensitive for different calculations of the Froude number and water depth. Figures 5.6A and 5.6B predict that 50% and 40% of the waves will be breaking bores, which is clearly not the case in this research. When using the corrected Froude number, the predictions become closer to the observations, however the percentage of stoke waves increases. Stoke waves are characterized by an equally high crest and trough amplitude, but a longer trough than crest. This is not convincingly observed in the wave evolution graphs (Figure 4.9).

As expected, the waves which are most likely the closest to breaking (for example run 19, 20, 29 and 30 with a high volume or water content), appear in the upper right corner of the graphs. Similarly, the runs with a low volume, low water and clay content and low slope, appear in the lower left corner. This proves that the determination of wave type with the wave type product and the Froude number is applicable to this research, but the threshold values between the wave types should be adapted.

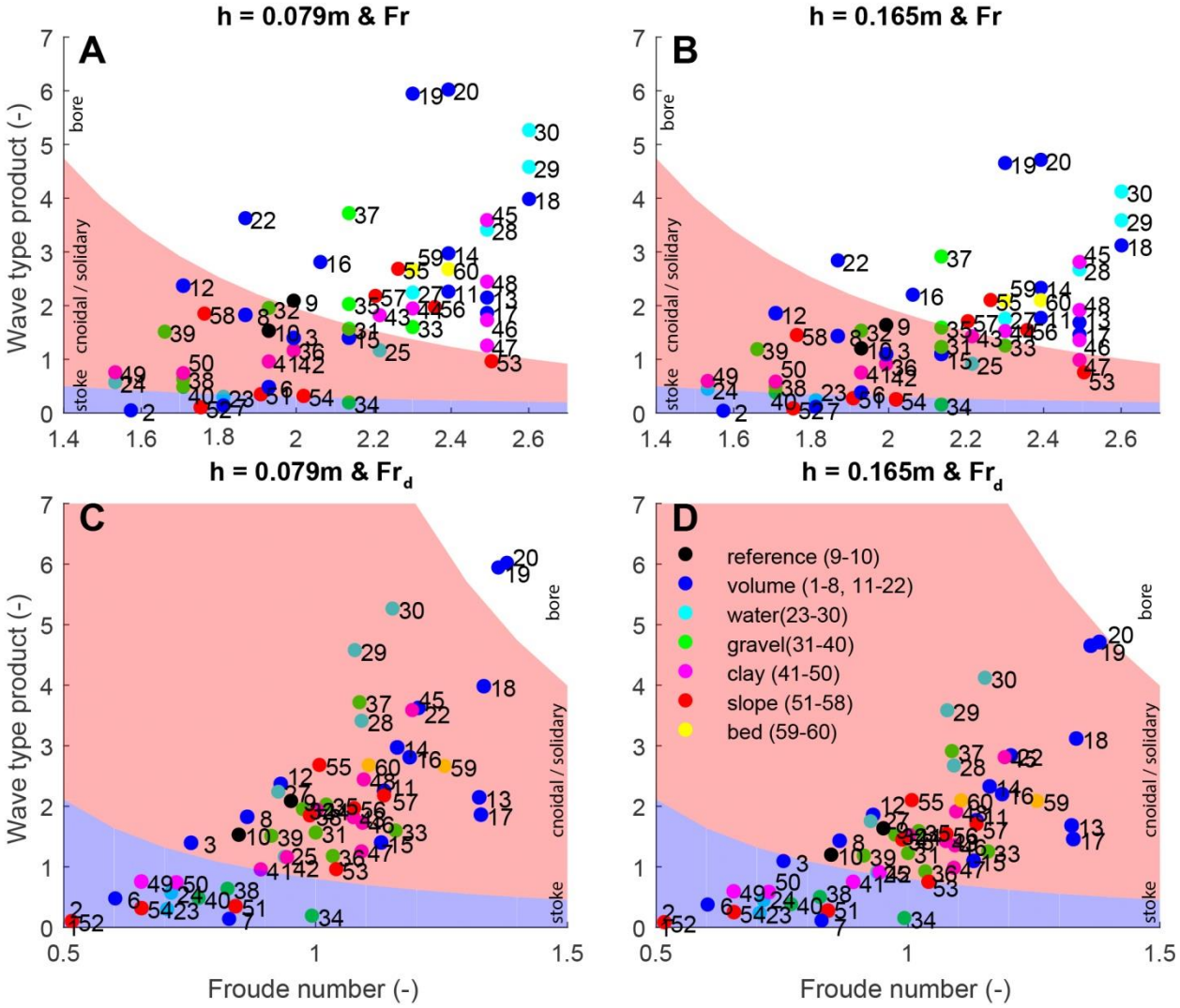

Figure 5.6. Wave shape, predicted with the wave type product (equation 5.12) For different values for h and Fr. The blue shaded area indicates stoke-like waves, red area indicates cnoidal or solidary waves, the white area indicates breaking bores.

Wave nonlinearity is observed in all comparable studies, however, the wave shape observed in this research is not necessarily similar (see Table 5.3). In the research of *Fritz et al. (2004*), all four wave types are observed. They found a relation between the non-linearity and the location of the maximum crest, where in the strong non-linear regime the leading wave amplitude is equal to the maximum wave amplitude. This relation is not observed in this study. *Miller et al. (2017*) only observed solidary waves and breaking bores, depended on the ratio between volume and water depth. The study of *Mohammed & Fritz (2012*) is most comparable to our study in terms of debris-flow type (granular, varying grain size) and setup (3D), and also the observed wave types are similar. It is hypothesized that besides the sloping wave basin floor, the 2D or 3D character of the physical experiments is important for the development of a specific wave type.

5.3 Consideration of scaling

Debris-flow and wave behavior in this setup are comparable to larger scaled studies. In earlier subaerial research with the same setup, *de Haas et al. (2015*) found a flow behavior, deposit morphology, grain size sorting, channel width-depth ratio, and runout length comparable to nature. Therefore, it can be said that the relations found in this research are most certainly applicable to natural situations, however the quantitative correlations cannot be directly applied in the field.

Table 5.5 compares the range of (non)dimensional parameters of this study regarding the debris flow, to the research of *Iverson (1997*) and natural debris flows. A small setup means a relatively large influence of flow viscosity, capillary forces and grain inertia, but a disproportionally small influence of pore pressure on the debris-flow behavior. This results in a large Bagnold number (large influence of collisional forces of grains) and a large Reynolds grain number (larger effect of particle collision than pore fluid viscosity). These scale problems could affect the thickness and velocity of the debris flow, but do not directly affect the generated impulse waves.

When assessing the traditional scaling rules as described in *Heller (2011*), the Reynolds (Re) and Froude (Fr) number fall within the range of the rule of thumb determined by *Heller et al. (2008*) for impulse transfer. However, with the average water depth used in this setup, scale effects for surface tension should be taken into account. *Heller (2011)* states that surface tension becomes relevant in models which include wave breaking (air entrainment), small water depths and capillary waves. Surface tension could suppress the wave height and increase dissipation. However, the suppression of wave height in combination with the surface tension, could also avoid breaking, resulting in a larger wave amplitude than when breaking would have occurred.

To determine the influence of scale effects on waves, the Weber number is calculated (equation 3.14). In this research, Wb > 60, indicating inertial forces are dominant over surface tension forces. To avoid the dominance of scale effects, there is carefully dealt with runs with capillary waves (<2 mm) during analyses. This was only necessary at a few low volume runs and waves at x_b > 1.55 m. The capillary force acting on one wave (surface tension coefficient for water 0.07 N/m * surface area of the wave), expressed in surface tension energy, is <0.005 J. On average, the surface tension is about 1% the size of the wave energy, which is at the limit of the traditional scaling rules (Table 2.1). This amount is negligible considering qualitative relations, however this implies that quantitative relations found cannot be used directly in the field.

parameter	symbol (unit)	this study	USGS Flume[a]	natural debris flows[a]
grain diameter	δ (m)	0.0005-0.003	0.001	10^{-5} -10^{1}
flow depth	h_s (m)	0.005-0.04	0.1	0.1-10
flow velocity	u_s (m/s)	1.00-3.74	10	0.1-20
flow shear rate	γ (1/s)	44.5- 300.8	100	1-100
solid density	ρ_s (kg/m^3)	2650-3400	2700	2500-3000
fluid density	ρ (kg/m^3)	1000	1100	1000-1200
solid volume fraction	v_s (-)	0.4-0.6	0.6	0.4-0.8
fluid volume fraction	v_f (-)	0.4-0.6	0.4	0.2-0.6
fluid viscosity	μ (Pa s)	0.001-0.0035[b]	0.001	0.001-0.1
friction angle	ϕ (°)	42[g]	40	25-45
hydraulic permeability	k (m^2)	1.1 * 10^{-16} -2.1* 10^{-13} [b]	10^{-11}	10^{-13} -10^{-9}
hydraulic diffusivity	D (m^2/s)	5.8* 10^{-9} - 1.2 * 10^{-1} [b]	10^{-4} [c]	10^{-8} -10^{-2} [c]
slide Froude number	Fr (-)	2.9-7.7	10.1	0.01-20.2
Savage number	Sv (-)	3.51*10^{-5}- 0.49	0.2	10^{-7}-10^{0} [a, e, f]
Bagnold number	Bg (-)	1.12*10^{4} - 3.59*10^{6}	400	10^{0} –10^{8} [a, e]
friction number	Fn (-)	117-5.25*10^{4}	2*10^{3}	10^{0} - 10^{5} [a, f]
mass number	Mn (-)	1.8-4.0	4	1-10 [b]
Darcy number	Dc (-)	7.75*10^{3} -6.74 * 108	600	10^{4}-10^{8}
Reynolds number	Re (-)	4.33*10^{4}-1.04*10^{5}	3*10^{3} [d]	10^{5}-10^{7} [d, e]
grain Reynolds number	Re_g (-)	2.82*10^{3} -2.03*10^{6}	100	0.01-2 [a, f]

Table 5.5. (non)Dimensional parameters of this small scale study compared to the USGS flume and natural debris flows. Values are taken or calculated form the source specified in the header unless specified otherwise in the footnotes. [a] *Iverson (1997)*. [b] *de Haas et al. (2015)*. [c] *Major (2000)*. [d] *Iverson et al. (2010)*. [e] *Iverson and Denlinger (2001)*. [f] *Zhou and Ng (2010)*. [g] Estimated values

5.4 Practical impact

When a debris flow debouches in a lake, this can have very big impacts. An impulse wave of more than 200m high is estimated by *Hermanns et al. (2004*) during a landslide impact 4000 B.P in Argentina. In 1806 AD, a landslide caused a 15 m high impulse wave at the southern slope of the Rossberg mountain, Switzerland (*Bussman & Anselmetti, 2010*). The landslide generated tsunami in Lituya Bay, USA in 1958 produced a run-up of 524 m (*Fritz et al., 2001*). More recently, in 2015 a run-up height of 192 m is measured in southeast Alaska, after a massive landslide debouched in a lake (*Dufresne et al., 2018*), in 2007 a rock slide entered Chehalis lake in Canada, resulting in a run-up height of 18 m. In September 2018 a debris-flow generated tsunami (3-10 m high waves) initiated by an earthquake in Indonesia caused many casualties. The country got hit again in December 2018, this time by a debris-flow generated tsunami induced by a volcanic eruption, resulting in 1-3 m high waves.

The effect of the debris flow pushing the impulse wave forward in the near-field zone, is recorded during the tsunami generation in September 2018. Figure 5.6 shows the resemblance of the real situation (A) and the performed physical experiments (B). This is again an indication or even proof that small-scale experiments which encounter scale-effects, show close similarity with nature.

The abovementioned examples show the importance of accurate prediction of debris-flow generated tsunamis. This study is one of the contributions which is ultimately aiming in decreasing the damage and casualties by these hazards. I showed that debris-flow velocity is dependent on its volume, composition and slope. The debris flow pushing the wave forward until detachment is the main driver for wave celerity. This relation should be expanded to make it suitable for prediction of natural debris-flow generated impulse waves. Wave amplitude is the most difficult to predict, given the large variation I found. Predictive formulas based on momentum transfer should be adapted to include a multi-phase debris flow and a sloping lake bottom. Amplitude imposes, next to celerity, the largest risk for coast populations, hence accurate prediction of those values is therefore valuable for hazard management.

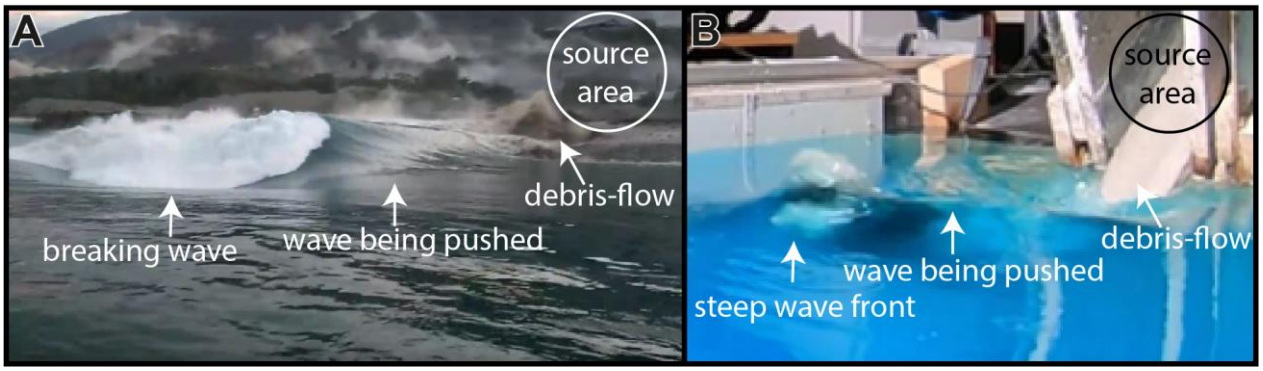

Figure 5.7. Comparison between debris-flow generated tsunami in nature, Sulawesi 2018 (A) and in our setup (B).

5.5 Recommendations for future research

First, methodological improvements can be suggested. The measurement devices work at their lower limits. Since small-scale experiments allow for that many systematic measurements in a short amount of time, improvement in measuring on such a small scale is desirable.

Next, the displacement and dispersal of debris-flow sediment by the waves, and the influence on this on the wave development, is a topic for follow up research. As briefly discussed in section 4.3, the character of the initial bed of the wave basin influences the interaction of the debris flow with the bed, which in turn influences the wave characteristics. Experiments to study this effect are desired.

The slope of the wave basin highly influences the wave behavior, since the wave travels to deeper water. Numerical modeling could help in unraveling the influence of lake bathymetry on wave development and evolution. The currently developed model r.avaflow could be a useful tool for this (*Mergili et al., 2017*).

Although physically based and proved in *Mulligan & Take (2017*), the momentum transfer theory does not give satisfying results in predicting wave characteristics. Rather, debris-flow velocity is the best predictor. What is the physical explanation behind this?

The relation between debris-flow velocity and wave celerity is strong. It is desired to expand this relation to make it suitable for real life predictors. Furthermore, more research is necessary to explore the driving factor(s) for wave amplitude.

6. Conclusions

Debris-flow generated impulse waves are particularly dangerous because of their unpredictability and large and fast wave. It can have devastating effects on landscape and society. This master thesis aims to study the wave generation and evolution of impulse waves for different debris-flow characteristics. Within a small scale 3D physical laboratory model, a multi-phase debris flow flows down an outflow slope (2.0 x 0.12 m) and debouches into a wave basin (1.85 x 0.9 m, 10°) where a tsunami wave is generated. 60 experiments are conducted in which debris-flow volume (3.5-18 kg), water content (40-60 vol%), gravel content (0-64 vol%), clay content (0-29 vol%) and outflow slope (20-40°) are systematically varied. The herein presented results of the experimental study can be summarized as followed:

- Debris-flow thickness is mostly determined by its volume, while velocity is mostly controlled by water and clay content due to its lubricating effect. There is an optimum debris-flow composition for clay content, which act as a lubricant by retaining the excess pore pressure, until the viscosity effect takes over, reducing the debris-flow velocity. The trends in debris-flow thickness and velocity, are reflected in the amplitude and celerity of the leading waves.
- Both energy and momentum scale relatively well with the wave energy, but debris-flow velocity is the best predictor for celerity and wavelength. The amplitude of the leading crest is difficult to correlate to debris-flow characteristic, but is the best estimated using debris-flow momentum.
- Wave generation starts with the formation of an impact crater, and the water surface becomes turbulent. The debris flow pushes the water forward, transferring 0.1-22 % of its energy to the leading crest, hereby over steepening and accelerating the wave. The wave is detached when the wave celerity exceeds the debris-flow velocity. Debris flows with a low momentum/energy result in a relatively small amount of air entrainment during wave generation, a quick release of the wave and therefore the development of more, smaller waves following the leading crest.
- All waves occur in the intermediate water regime and are non-linear. Close to the impact area, wave heights could exceed the wave breaking criteria. However, breaking waves are not observed due to the down sloping floor of the wave basin.
- Wave amplitudes varied between 2-34 mm, and are the largest just after detachment (approximately at x_b = 0.50 m). Wave celerity (0.62-1.65 m/s) decreases with increasing travel distance till the value predicted by the deep water approximation. The period (0.47-1.03 s) increases in the far-field. Both are the result of the over steepening and acceleration caused by the debris flow in the near-field zone.
- Predictive formulas developed by previous research perform poorly with our experimental data. The wave amplitude predictors of *Fritz et al. (2004*) and *Heller & Hager (2010*) both underestimate the measured maximum amplitude. The wave amplitude predictor of *Mulligan & Take (2017*) is highly sensitive to water depth, and performs the best using the average water depth. It shows that the assumption of momentum exchange is, contrary to *Mulligan & Take's (2017*) constraints, also valid for saturated debris flows. The wave shape predictor of *Heller & Hager (2011*) should be adapted with the use of the corrected Froude number (eq. 5.2) and a sloping wave basin floor should be incorporated before being able to make accurate predictions.
- Using a small setup gives the advantage of being able to perform many systematic experiments. In this study, scale effects affect the debris flow by grains inertia and capillary forces having a disproportionally large influence, while pore pressure is relatively small. Surface tension affected the smallest waves, but is on average less than 1 % of the total wave energy.
- Being able to predict wave height and celerity from debris-flow characteristics is very important to hazard management. This study brings us one step further in understanding and predicting debris-flow generated tsunami waves.

References

Acosta, E.A., Tibana, S., de Souza Soares de Almeida, M., Saboya Jr. (2017) Centrifuge modeling of hydroplaning in submarine slopes. Ocean Engineering 129, 451–458

Ataie-Ashtiani, B., and A. Najafi-Jilani (2008). Laboratory investigations on impulse waves caused by underwater landslides, Coastal Eng., 55, 989–1074.

Ataie-Ashtiani, B., and Nik-Khah, A. (2008), Impulsive waves caused by subaerial landslides, Environ. Fluid Mech., 8, 263–280.

Atwater, B.F., Moore, A.L. (1992). A tsunami about 1000 Years Ago in Puget Sound, Washington. Science, New Series, 258, 5088, pp. 1614-1617

Bagnold, R.A. (1954). Experiments on a gravity-free dispersion of large solid spheres in a Newtonian fluid under shear. Proc. R. Soc. Londen, Ser. A. 225, 49-63.

Boussinesq, J. (1872). "Théorie des ondes et des remous que se propagent le long d'un canal rectangulaire horizontal, en communiquant au liquid contenu dans ce canal des vitesses sensiblement pareilles de la surface au fond." J. Math. Pures Appl., 17, 55–108.

Bryant, S. K., Take, W.A., and Bowman, E.T. (2015), Observations of grain-scale interactions and simulation of dry granular flows in a largescale flume, Can. Geotech. J., 52(5), 638–655.

Bussmann, F., Anselmetti, F.S. (2010). Rossberg landslide history and flood chronology as recorded

Charvet, I., Suppasri, A., Kimura, H., Sugawara, D., and Imamura, F. (2015). A multivariate generalized linear tsunami fragility model for Kesennuma City based on maximum flow depths, velocities and debris impact, with evaluation of predictive accuracy. Natural Hazards, 79(3), 2073-2099.

Chen, C., Yu, F. (2011). Morphometric analysis of debris flows and their source areas using GIS. Geomorphology 129, pp 387–397

Comiti, F., Marchi, L., Macconi, P., Arattano, M., Bertoldi, G., Borga, M., and Theule, J. (2014). A new monitoring station for debris flows in the European Alps: first observations in the Gadria basin. Natural hazards, 73(3), 1175-1198.

Costa, J. E. and Williams, G. P. (1984) Debris-flow dynamics: U.S. Geological Survey Open File Report 84-606, 1 VHS videotape

Costa, J.E. (1988). Rheologic, geomorphic, and sedimentologic differentiation of water floods, hyperconcentrated flows, and debris flow. Flood geomorphology. 113-122. 113-122.

Coussot, P. (1997) Mudflow Rheology and Dynamics. IAHR Monograph, Balkema, Rotterdam, 272 pp

Cuomo, G., Allsop, W., Takahashi, S. (2010). Scaling wave impact pressures on vertical walls. Coastal Engineering 57(6), 604–609.

De Blasio, F.V., Elverhøi, A., Engvik, L.E., Issler, D., Gauer, P. and Harbitz, C. (2006) Understanding the high mobility of subaqueous debris flows. Norwegian Journal of Geology,Vol. 86, pp. 275-284

Dufresne, A., Geertsema, M., Shugar, D. H., Koppes, M., Higman, B., Haeussler, P. J., Stark, C., Venditti, J.G., Bonno, D., Larsen, C., Gulick, S. P. S., McCall, N., Walton, M., Loso, M.G., Willis, M.J. (2018). Sedimentology and geomorphology of a large tsunamigenic landslide, Taan Fiord, Alaska. Sedimentary Geology, 364, 302-318.

de Haas, T., L. Braat, J. R. F. W. Leuven, I. R. Lokhorst, and M. G. Kleinhans (2015), Effects of debris flow composition on runout, depositional mechanisms, and deposit morphology in laboratory experiments, J. Geophys. Res. Earth Surf., 120

de Haas, T., van den Berg, W., Braat, L., Kleinhans, M.G. (2016). Autogenic avulsion, channelization and backfilling dynamics of debris-flow fans. Sedimentology 63, 1596-1619

Dean RG, Dalrymple RA. (1991). Water wave mechanics for engineers and scientists. Singapore:

Dean, R. G., and Dalrymple, R. A. (1991). "Water wave mechanics for engineers and scientists." Advanced series on ocean engineering, Vol. 2, World Scientific, Singapore.

deformable granular landslides on planar and conical slopes. Landslides 15, 1713–1730.

Deng, J., Zhang, X., Shen, S., and Koseki, J. (2018). Low friction coefficient (approximately tan1) of subaqueous debris flow in rotating flume tests and its mechanism. Bulletin of Engineering Geology and the Environment, 1-9.

Edgers, L., and Karlsrud, K. (1981). Viscous analyses of submarine flows. Report 52207. Norwegian Geotechnical Institute, Norway.

Elverhøi, A., Harbitz, C. B., Dimakis, P., Mohrig, D., Marr, J., and Parker, G. (2000). On the dynamics of subaqueous debris flows. Oceanography, 13(3), 109-117.

Fritz HM, Hager WH, Minor H-E. (2001) Lituya Bay case rockslide impact and wave run-up. Sci. Tsunami Haz. 19, 3–22

Fritz, H. M., and Liu, P. C. (2002). "An application of wavelet transform analysis to landslide generated impulse waves." Proc., 4th Int. Symp. on Ocean Wave Measurement and Analysis, San Francisco, 2001, B. L. Edge et al., eds., ASCE, Reston, Va., 2, 1477-1486.

Fritz, H. M., Hager, W. H., and Minor, H. E. (2004). Near field characteristics of landslide generated impulse waves. Journal of waterway, port, coastal, and ocean engineering, 130(6), 287-302.

Fritz, H. M., W. H. Hager, and H.-E. Minor (2003a), Landslide generated impulse waves. 1. Instantaneous flow fields, Exp. Fluids, 35, 505–519

Fritz, H. M., W. H. Hager, and H.-E. Minor (2003b), Landslide generated impulse waves. 2. Hydrodynamic impact craters, Exp. Fluids, 35, 520–532

Gauer, P., Kvalstad, T. J., Forsberg, C. F., Bryn, P., and Berg, K. (2005). The last phase of the Storegga Slide: simulation of retrogressive slide dynamics and comparison with slide-scar morphology. In Ormen Lange–an Integrated Study for Safe Field Development in the Storegga Submarine Area, pp. 171-178.

Godt, J.W., Coe, J.A. (2007). Alpine debris flows triggered by a 28 July 1999 thunderstorm in the central Front Range, Colorado. Geomorphology, 84, 1–2, pp 80-97

Goff, J. and Chauge-Goff, C. (2014) The Australian Tsunami Database: A Review. Progress in Physical Geography 38, 2, 218-240

Hammack, J.L. (1973) A note on tsunamis: their generation and propagation in an ocean of uniform depth. Journal of fluid mechanics, 60, 4pp. 769-799

Hampton, M.A. (1972) The Role of Subaqueous Debris Flow in Generating Turbidity Currents. Journal of Sedimentary Petrology, 42- 4, pp775-793

Hartmann, D.L., Klein Tank, A.M.G., Rusticucci, M., Alexander L.V., Brönnimann, S., Charabi, Y., Dentener, F.J., Dlugokencky, E.J., Easterling, D.R., Kaplan, A., Soden, B.J., Thorne, P.W., Wild, M., and Zhai, P.M. (2013): Observations: Atmosphere and Surface. In: Climate Change 2013: The Physical Science Basis. Contribution of Working Group I to the Fifth Assessment Report of the Intergovernmental Panel on Climate Change [Stocker, T.F., D. Qin, G.-K. Plattner, M. Tignor, S.K. Allen, J. Boschung, A. Nauels, Y. Xia, V. Bex and P.M. Midgley (eds.)]. Cambridge University Press, Cambridge, United Kingdom and New York, NY, USA

Heller, V. (2011), Scale effects in physical hydraulic engineering models, J. Hydraul. Res., 49(3), 293–306.

Heller, V., Hager, V.H., Minor, H.E. (2008). Scale effects in subaerial landslide generated impulse waves. Exp. Fluids 44 (5), 691-703.

Heller, V., Hager, V.H., Minor, H.E. (2009). Landslide generated impulse waves in reservoirs – basics and computation. In: Boes, R, VAW-Mitteilung, 211. ETH Zurich, Zurich.

Heller, V., and Hager, W. H. (2010). Impulse product parameter in landslide generated impulse waves. Journal of waterway, port, coastal, and ocean engineering, 136(3), 145-155.

Heller, V., and Hager, W. H. (2011). Wave types of landslide generated impulse waves. Ocean Engineering, 38(4), 630-640.

Heller, V., and Spinneken, J. (2013), Improved landslide-tsunami prediction: Effects of block model parameters and slide model, J. Geophys. Res. Oceans, 118(3), 1489–1507

Heller, V., and Spinneken, J. (2015). On the effect of the water body geometry on landslide–tsunamis: Physical insight from laboratory tests and 2D to 3D wave parameter transformation. Coastal Engineering, 104, 113-134.

Heller, V., Bruggemann, M., Spinneken, J.,Rogers, B.D. (2016). Composite modelling of subaerial landslide–tsunamis in different water body geometries and novel insight into slide and wave kinematics, Coast. Eng. 109, 20–41.

Hermanns, R.L., Niedermann, S., Ivy-Ochs, S., Kubik, P.W. (2004). Rock avalanching into a landslide-dammed lake causing multiple dam failure in Las Conchas valley (NW Argentina) — evidence from surface exposure dating and stratigraphic analyses. Landslides 1, 113–122

Hoefling, R. (2004), High-speed 3D imaging by DMD technology, in Machine Vision Applications in Industrial Inspection XII, pp. 188–194, Int. Soc. for Optics and Photonics, San Jose, California

Hooke, R.L., (1968). Model geology: prototype and laboratory streams: discussion. Geological Society of America Bulletin 79, 391–394

Hooke, R.B. and Rohrer, W.L. (1979) Geometry of alluvial fans: effect of discharge and sediment size. Earth Surf. Proc., 4, 147–166.

Huber, A. (1980), Schwallwellen in Seen als Folge von Bergstürzen, VAW Mitteil. 47, Versuchsanst. Für Wasserbau, Hydrol. und Glaziol., ETH Zurich, Zurich, Switzerland.

Hughes, S.A. (1993). Advanced series on ocean engineering 7. Physical models and laboratory techniques in coastal engineering. World Scientific, London.

Ilstad, T., De Blasio, F. V., Elverhøi, A., Harbitz, C. B., Engvik, L., Longva, O., and Marr, J. G. (2004c). On the frontal dynamics and morphology of submarine debris flows. Marine Geology, 213(1-4), 481-497.

Ilstad, T., Elverhøi, A., Issler, D., and Marr, J. G. (2004b). Subaqueous debris flow behaviour and its dependence on the sand/clay ratio: a laboratory study using particle tracking. Marine Geology, 213(1-4), 415-438.

Ilstad, T., Marr, J. G., Elverhøi, A., and Harbitz, C. B. (2004a). Laboratory studies of subaqueous debris flows by measurements of pore-fluid pressure and total stress. Marine Geology, 213(1-4), 403-414.

Imran, J., Parker, G., Locat, J., Lee, H.J. (2001). 1-D numerical model of muddy subaqueous and subaerial debris flows. ASCE Journal of Hydraulic Engineering. 127, 959-968.
in Lake Lauerz sediments (Central Switzerland). Swiss J Geoscience 103, 43–59

Iverson, R.M. (1997). The physicis of debris flows. Reviews of Geophysics, 35, 3, 245–296

Iverson, R. M., and Denlinge, R.P. (2001), Flow of variably fluidized granular masses across three-dimensional terrain: 1. Coulomb mixture theory, J. Geophys. Res., 106(B1), 537–552.

Iverson, R. M., Logan, M., LaHusen, R.G., Berti, M. (2010), The perfect debris flow? Aggregated results from 28 large-scale experiments, J. Geophys. Res., 115, F03005

Iverson, R. M., Reid, M.E., and LaHusen, R.G. (1997). Debris-flow mobilization from landslides, Ann. Rev. Earth Planet. Sci., 25, 85–138

Iverson, R.M., Costa, J.E., and LaHusen, R.G. (1992). Debris-flow flume at H. J. Andrews Experimental Forest, Oregon. U.S. Geological Survey, Dept. of the Interior.

Johnson, A.M. (1970). Physical Processes in Geology. Freeman and Cooper, San Francisco, California

Johnson, C.G., Kokelaar, B.P., Iverson, R.M., Logan, M., LaHusen, r.G., Gray, J.M.N.T. (2012). Grain-size segregation and levee formation in geophysical mass flows. J. Geophys. Res. 117, F01032

K. Sassa, Canuti, P. (2000), Landslides – Disaster Risk Reduction, Springer-Verlag Berlin Heidelberg

Kafle, J., Pokhrel, P.R., Khattri, K.B., Kattel, P., Tuladhar, B.M. Pudasaini, S.P. (2016). Landslide-generated tsunami and particle transport in mountain lakes and reservoirs. Annals of Glaciology 57(71)

Laberg, J. S., and Vorren, T. O. (1995). Late Weichselian submarine debris flow deposits on the Bear Island Trough mouth fan. Marine Geology, 127(1-4), 45-72.

Laitone E.V. (1960). The second approximation to cnoidal and solitary waves. J. Fluid Mech. 9, 430–444.

Lamb H. (1932). Hydrodynamics. New York, NY: Dover.

Lighthill J. (2001). Waves in fluids. Cambridge, UK: Cambridge University Press.

Locat, J., and Lee, H. J. (2005). Subaqueous debris flows. In Debris-flow hazards and related phenomena (pp. 203- 245). Springer, Berlin, Heidelberg.

Logan, M., Iverson, R.M., and Obryk, M.K. (2018). Video documentation of experiments at the USGS debris-flow flume 1992–2017 (ver 1.4, January 2018): U.S. Geological Survey Open-File Report 2007–1315

Madsen, P. A., Fuhrman, D.R., and Schaffer, H.A. (2008), On the solitary wave paradigm for tsunamis, J. Geophys. Res.,113, C12012,

Major, J. J. (2000), Gravity-driven consolidation of granular slurries—Implications for debris-flow eposition and deposit characteristics, J. Sediment. Res., 70(1), 64–83.

Marchi L., Arattano M., Deganutti A.M. (2002). Ten years of debris-flow monitoring in the Moscardo Torrent (Italian Alps). Geomorphology 46(1-2), 1-17.

McCowan, J. (1894), On the highest wave of permanent type, Philos. Mag., 38(233), 351–358.

McFall, B. C. and H. M. Fritz (2016). Physical modelling of tsunamis generated by 3D deformable granular landslides on planar and conical island slopes, Proc. R. Soc. A, 472(2188), 20160052

McFall, B.C., Mohammed, F., Fritz, H.M., Liu, Y. (2018). Laboratory experiments on three-dimensional deformable granular landslides on planar and conical slopes. Landslides (2018) 15:1713–1730

Mergili, M., Fischer, J.-T., Krenn, J., Pudasaini, S.P. (2017): r.avaflow v1, an advanced open source computational framework for the propagation and interaction of two-phase mass flows. Geoscientific Model Development 10: 553-569.

Miller, G. S., W. Andy Take, R. P. Mulligan, and S. McDougall (2017), Tsunamis generated by long and thin granular landslides in a large flume, J. Geophys. Res. Oceans, 122

Mohammed, F., and Fritz, H.M. (2012), Physical modeling of tsunamis generated by three-dimensional deformable granular landslides, J. Geophys. Res., 117, C11015

Mohrig, D., Ellis, C., Parker, G., Whipple, K. X., and Hondzo, M. (1998). Hydroplaning of subaqueous debris flows. Geological Society of America Bulletin, 110(3), 387-394.

Mohrig, D., Elverhøi, A., and Parker, G. (1999). Experiments on the relative mobility of muddy subaqueous and subaerial debris flows, and their capacity to remobilize antecedent deposits. Marine Geology, 154(1-4), 117-129.

Motulsky, H. J., Ransnas, L. A. (1987). Fitting curves to data using nonlinear regression: a practical and nonmathematical review. FASEBJ 1, 365-374

Mulligan, R.P. and Take, W.A. (2017) On the transfer of momentum from a granular landslide to a water wave. Coastal Engineering 125 (2017) 16–22.

Najafi-Jilani, A., Ataie-Ashtiani, B., (2008). Estimation of near-field characteristics of tsunami generation by submarine landslide. Ocean Engineering 35 (2008) 545–557

Norem, H., Locat, J., Schieldrop, B. (1990). An approach to the physics and the modelling of subaqueous landslide. Marine Geotechnology, 9, 93-111.

Novak, P. (1984). Scaling factors and scale effects in modelling hydraulic structures. Symp. Scale effects in modelling hydraulic structures 0(3), 1–5. H. Rouse, ed. Technische Akademie, Esslingen.

Novak, P., Cabelka, J. (1981). Models in hydraulic engineering. Pitman, Boston.

Oerlemans, J. (2008). Minimal Glacier Models. Institute for Marine and Atmospheric Research Utrecht, Utrecht University. Igitur, Utrecht Publishing and Archiving Services. Second edition 2011.

Panizzo, A., DeGirolamo, P., and Petaccia, A. (2005). Forecasting impulse waves generated by subaerial landslides, J. Geophys. Res., 110, C12025.

Paola, C., Straub, K., Mohrig, D., Reinhardt, L. (2009). The “unreasonable effectiveness” of stratigraphic and geomorphic experiments. Earth-Science Reviews 97, 1–43.

Parsons, J. D., K. X. Whipple, and A. Simoni (2001), Experimental study of the grain-flow, fluid-mud transition in debris flows, J. Geology, 109(4), 427–447.

Prior, D. B., Bornhold, B. D., and Johns, M. W. (1984). Depositional characteristics of a submarine debris flow. The Journal of Geology, 92(6), 707-727.

Pudasaini, S. P. (2014). Dynamics of submarine debris flow and tsunami. Acta Mechanica, 225(8), 2423-2434.

Roberts, N.J., McKillop, R.J., Lawrence, M.S., Psutka, J.F., Clague, J.J., Brideau, M., Ward, B.C. (2013). Impacts of the 2007 Landslide-Generated Tsunami in Chehalis Lake, Canada. In: Margottini C., Canuti P., Sassa K. (eds) Landslide Science and Practice. Springer, Berlin, Heidelberg

Saelevik, G., Jensen, A., and Pedersen, G. (2009). Experimental investigation of impact generated tsunami; related to a potential rock slide, Western Norway, Coastal Eng., 56, 897–906.

Sitar, N., Anderson, S.A. and Johnson, K.A. (1992). Conditions for initiation of rainfall-induced debris flows, in Stability and Performance of Slopes and Embankments II Proceedings, pp. 834–849 Geotech. Eng. Div., Am. Soc. of Civ. Eng., New York.

Sterne, J. A. C., Smith, G.D., (2001). Sifting the evidence—what's wrong with significance tests? Physical Therapy 81 - 8, pp1464–1469.

Sumner, E.J., Talling, P.J. and Amy, L.A. (2009) The deposits of flows transitional between turbidity currents and debris flow. Geology, 37, 991–994

Talling, P. J., Masson, D. G., Sumner, E. J., and Malgesini, G. (2012). Subaqueous sediment density flows: Depositional processes and deposit types. Sedimentology, 59(7), 1937-2003.

Van Dine, D. (1996). Debris Flow Control Structures for Forest Engineering. Research Branch, Ministry of Forests, Victoria, BC Working Paper 22/1996.

Wiberg, P.L., Sherwood, C.R. (2008). Calculateing wave-generated bottom orbital velocites from surface-wave parameters. Computers&geosciences 34, 1243-1262.

Xian, B., Liu, J., Dong, Y., Lu, Z., He, Y., and Wang, J. (2017). Classification and facies sequence model of subaqueous debris flows. Acta Geologica Sinica (English Edition), 91(2), 751-752.

Yalin, M.S. (1971). Theory of hydraulic models. Macmillan, London.

Yavari-Ramshe, S., and Ataie-Ashtiani, B. (2016). Numerical modeling of subaerial and submarine landslide-generated tsunami waves—recent advances and future challenges. Landslides, 13(6), 1325-1368.

Yin, M., and Rui, Y. (2018). Laboratory study on submarine debris flow. Marine Georesources & Geotechnology, 36(8), 950-958.

Yin, M., Rui, Y., Xue,Y. (2018). Centrifuge study on the runout distance of submarine debris flows, Marine Georesources & Geotechnology.

Zhou, G. G., and C. W. Ng (2010), Dimensional analysis of natural debris flows, Can. Geotech. J., 47(7), 719–729.

Zweifel, A. (2004). Impulswellen: Effekte der Rutschdichte und der Wassertiefe. Ph.D. thesis, ETH Zurich, Zurich (in German)

Appendices

A1. Supplementary data

A1.E supplementary excel files

- A1.E1: E1_ experimental runs
- A1.E2: E2_debris-flow characteristics
- A1.E3: E3_wave height

A1.S supplementary movies

- A1.S1: S1_front004_m=4kg
- A1.S2: S2_front019_m=16kg
- A1.S3: S3_side023_water=0.4
- A1.S4: S4_side029_water=0.6
- A1.S5: S5_front037_gravel=0.52
- A1.S6: S6_front047_clay = 0.2
- A1.S7: S7_front050_clay=0.29
- A1.S8: S8_front052_slope=20
- A1.S9: S9_front057_slope=35

A2. Statistical relations

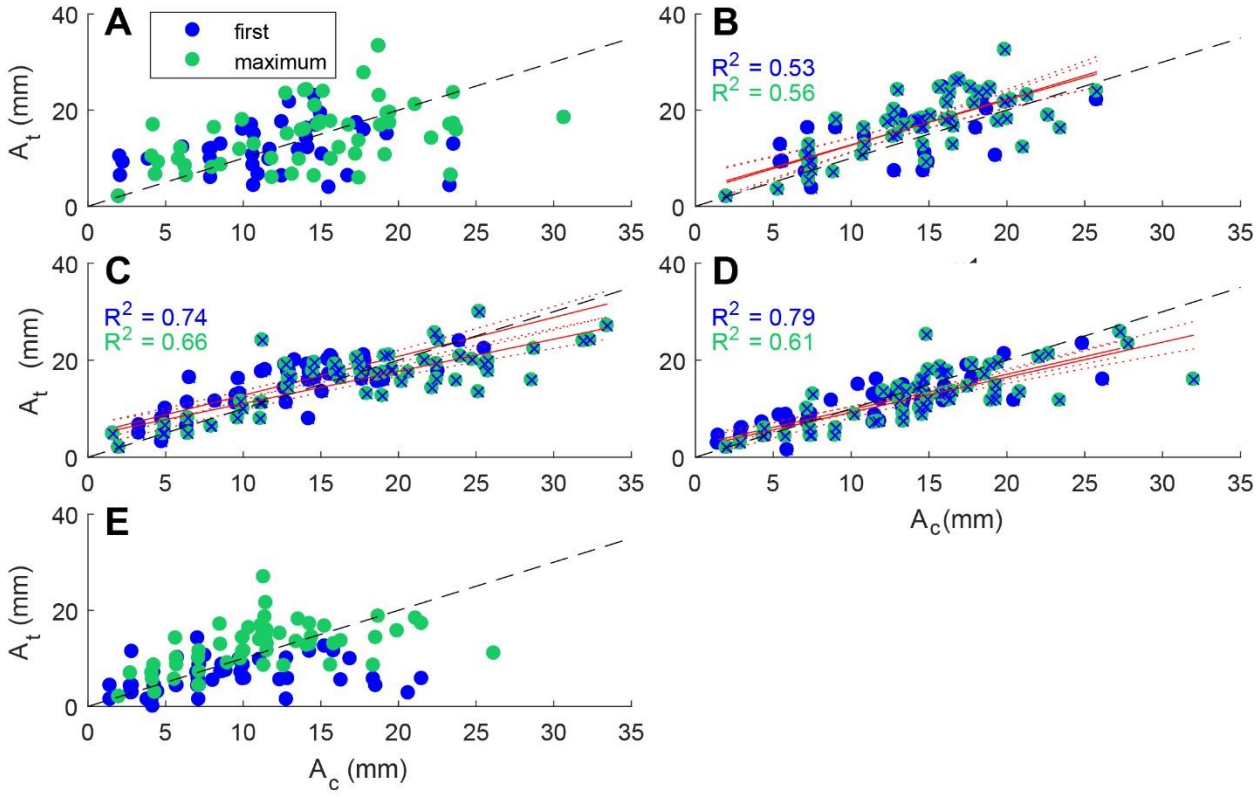

Figure A2.1. Crest against trough amplitude per location (x_b = 0.15, 0.50, 0.85, 1.20, 1.55 m).

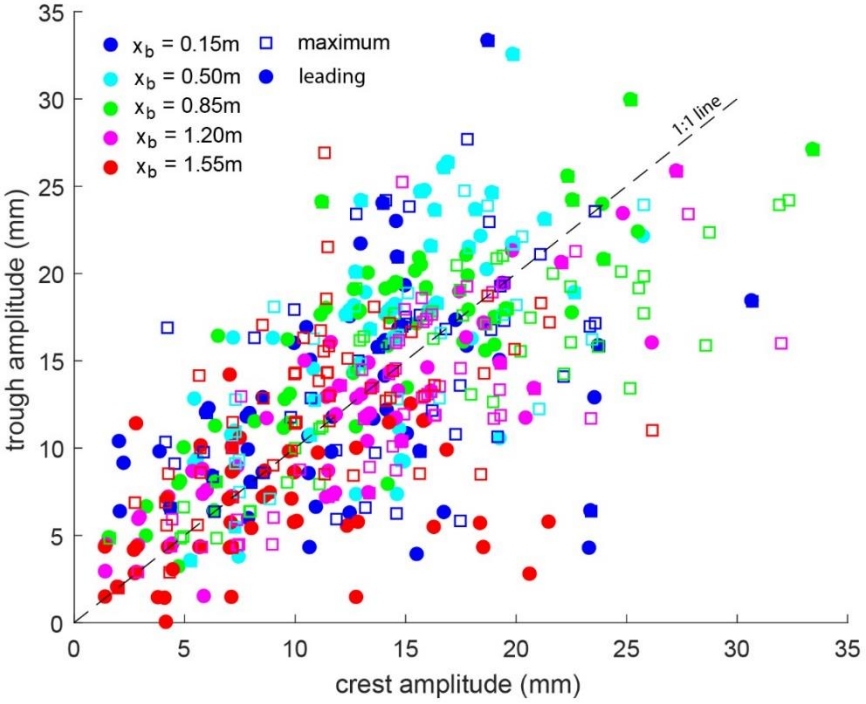

Figure A2.2. Trough against crest amplitude for both crest and trough at all locations.

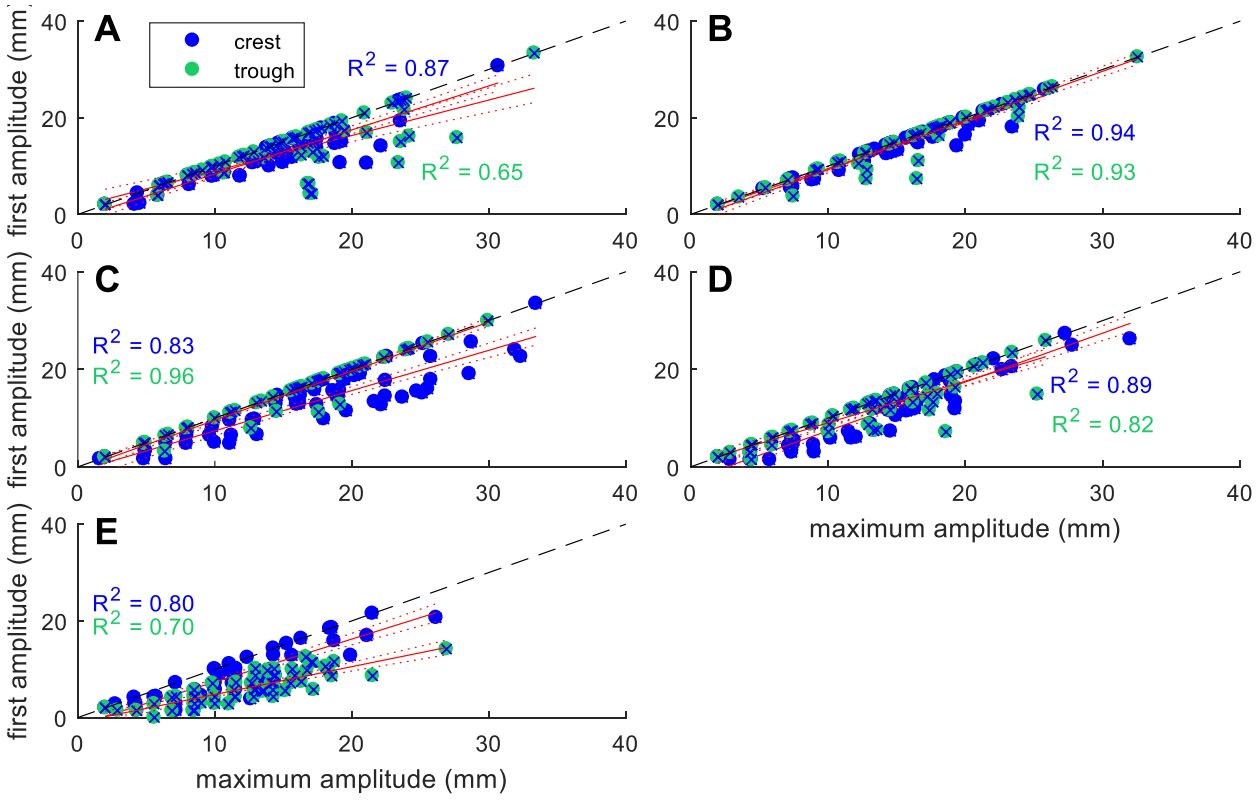

Figure A2.3. First amplitude against maximum amplitude per location (x_b = 0.15, 0.50, 0.85, 1.20, 1.55 m)

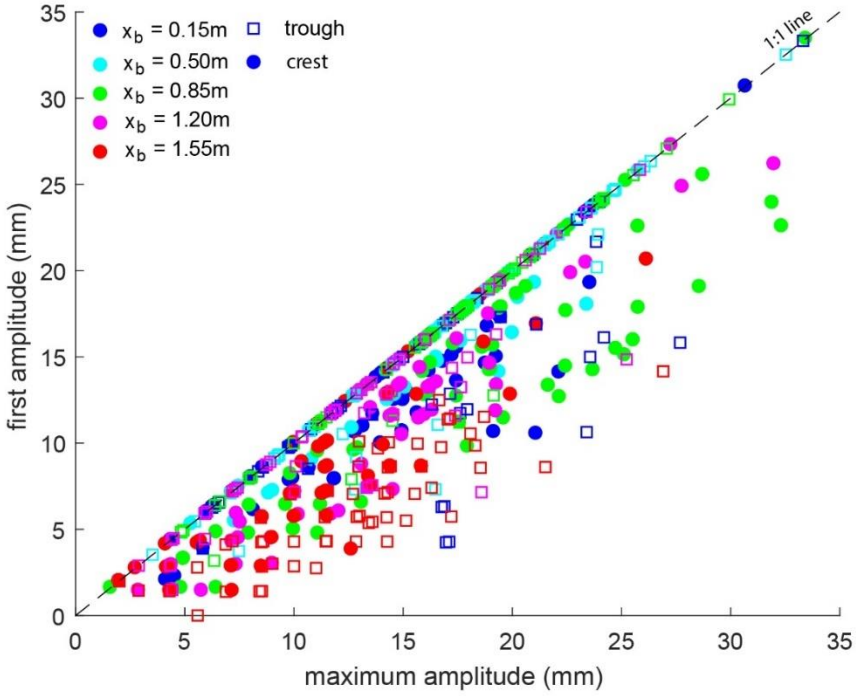

Figure A2.4. First amplitude against maximum amplitude for both crest and trough at all locations.

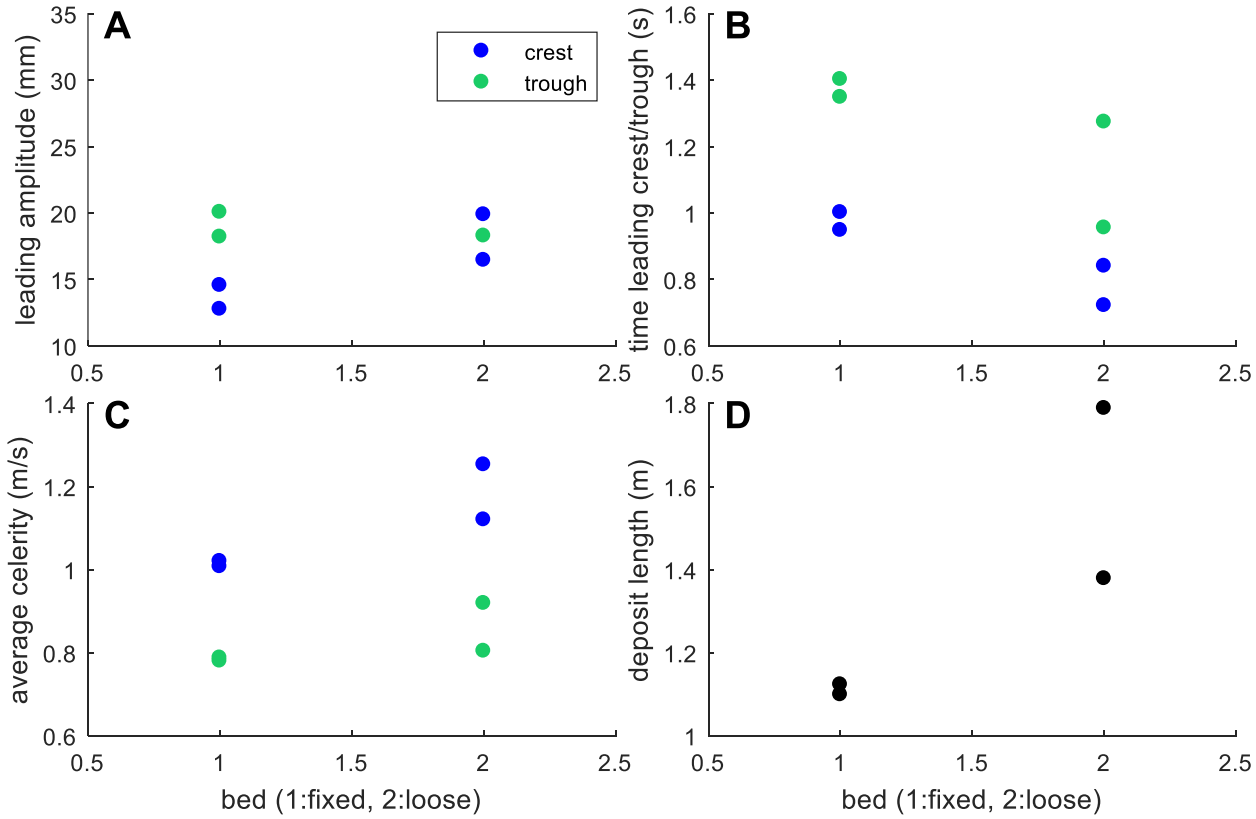

Figure A2.5. Importance of initial bed for wave and deposit characteristics.

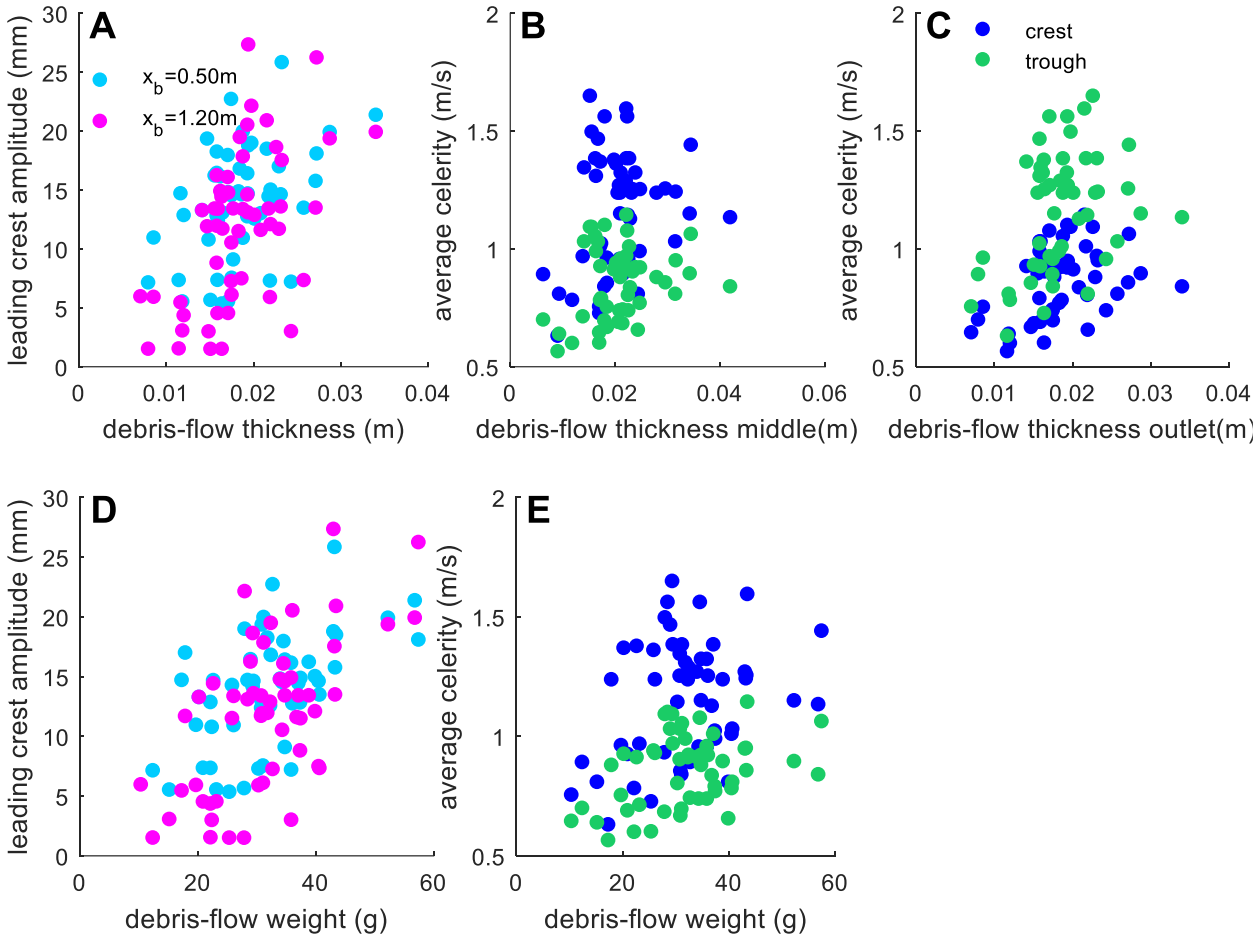

Figure A2.6. Influence of debris-flow thickness and weight on wave characteristics

	volume		**water content**		**gravel content**		**clay content**		**slope**	
	relation	R^2	relation	R^2	relation	R^2	relation	R^2	relation	R^2
thickness (outlet)	2.0 mm kg^{-1}	0.88	0.29 mm $\%^{-1}$	0.56	-	-	-*	0.39*	0.59 mm $^{\circ -1}$	0.65
weight	2.84 g kg^{-1}	0.71	-	-	-	-	-0.004 g $\%^{-1}$	0.69	1.12 g $^{\circ -1}$	0.72
velocity (mean)	0.05 m s^{-1} kg^{-1}	0.44	0.04 m s^{-1} $\%^{-1}$	0.90	-	-	-*	0.93*	0.03 m s^{-1} $^{\circ -1}$	0.43
energy	1.36 J kg^{-1}	0.57	1.24 J $\%^{-1}$	0.84	-	-	-*	0.73*	0.56 J $^{\circ -1}$	0.66
momentum	0.98 kg m*s^{-1} g^{-1}	0.61	0.79 kg m s^{-1} $\%^{-1}$	0.85	-	-	-*	0.68*	0.35 kg m s^{-1} $^{\circ -1}$	0.65
average predictor strength		0.64		0.79				0.69		0.62

Table A2.1. Linear regression and its R^2 values of debris-flow parameters and the corresponding thickness, weight and velocity. The darker the green color, the stronger the correlation. No value means an insignificant relation. * indicates a polynomial regression (quadratic relation).

	volume		**water content**		**gravel content**		**clay content**		**slope**	
	relation	R^2	relation	R^2	relation	R^2	relation	R^2	relation	R^2
leading crest amplitude	1.03 mm kg^{-1}	0.60	0.4 mm $\%^{-1}$	0.63	-	-	-*	0.42*	0.02 mm $°^{-1}$	0.51
time leading crest to x_b = 0.50	-0.05 s kg^{-1}	0.56	-0.04 s $\%^{-1}$	0.86	-	-	-*	0.93*	-0.02 s $°^{-1}$	0.27
average crest celerity	0.06 m s^{-1} kg^{-1}	0.56	0.04 m s^{-1} $\%^{-1}$	0.91	-	-	-*	0.96*	0.02 m s^{-1} $°^{-1}$	0.35
wave energy	0.03 J kg^{-1}	0.65	0.02 J $\%^{-1}$	0.92	-	-	-*	0.58*	0.007 J / $°^{-1}$	0.33
average predictor strength		0.59		0.83				0.72		0.37

Table A2.2. Linear regression and its R^2 values of debris-flow parameters and wave characteristics. The darker the green color, the stronger the correlation. No value means an insignificant relation. * indicates a polynomial regression (quadratic relation).

Debris flow → Waves ↓	**DF velocity**		**DF effective mass**		**DF energy**		**DF momentum**	
	relation	R^2	relation	R^2	relation	R^2	relation	R^2
leading crest amplitude at x_b = 0.50 m	8.27 mm $(m\ s^{-1})^{-1}$	0.30	1.19 mm kg^{-1}	0.29	0.36 mm J^{-1}	0.28	0.54 mm $(kg\ m\ s^{-1})^{-1}$	0.49
leading crest amplitude at x_b = 1.20 m	14.53 mm $(m\ s^{-1})^{-1}$	0.50	2.09 mm kg^{-1}	0.57	0.65 mm J^{-1}	0.58	0.97 mm $(kg\ m\ s^{-1})^{-1}$	0.60
travel time of leading crest to x_b = 0.50 m	-0.89 s $(m\ s^{-1})^{-1}$	0.77	-0.89 s kg^{-1}	0.39	-0.03 s J^{-1}	0.49	-0.04 s $(kg\ m\ s^{-1})^{-1}$	0.45
average crest celerity	0.69 m s^{-1} $(m\ s^{-1})^{-1}$	0.79	0.07 m s^{-1} kg^{-1}	0.39	0.04 m s^{-1} J^{-1}	0.65	0.05 m s^{-1} $(kg\ m\ s^{-1})^{-1}$	0.60
wave energy at x_b = 0.50 m	0.33 J $(m\ s^{-1})^{-1}$	0.53	0.05 J kg^{-1}	0.53	0.015 J J^{-1}	0.68	0.02 m $(kg\ m\ s^{-1})^{-1}$	0.64
detachment time	0.23 s $(m\ s^{-1})^{-1}$	0.30	0.04 s kg^{-1}	0.50	0.01 s J^{-1}	0.40	0.02 s $(kg\ m\ s^{-1})^{-1}$	0.47
wavelength at x_b = 0.50 m	0.74 m $(m\ s^{-1})^{-1}$	0.64	0.08 m kg^{-1}	0.39	0.03 m J^{-1}	0.50	0.04 m $(kg\ m\ s^{-1})^{-1}$	0.45
predictor strength		0.55		0.44		0.51		0.52

Table A2.3. Linear regression and its R^2 values of debris-flow and wave characteristics. The darker the green color, the stronger the correlation. No value means an insignificant relation. * indicates a polynomial regression (quadratic relation).

A3. Exclusion of data

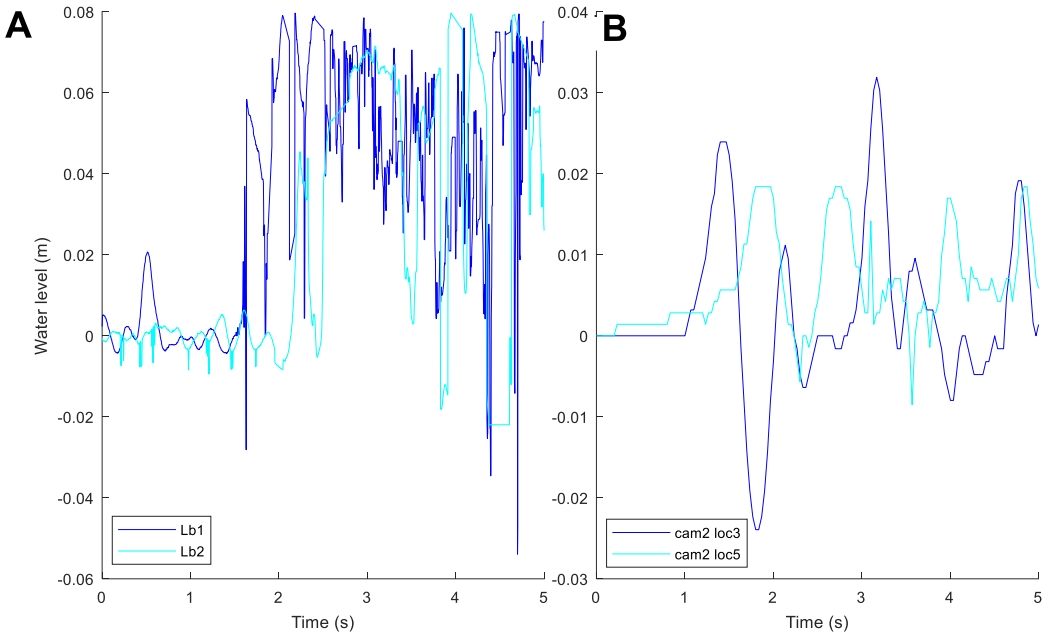

Figure A3.1. Water level over time for experiment 022. **A)** Incorrect laser measurements of the water level. **B)** corresponding water level measured with cam2.

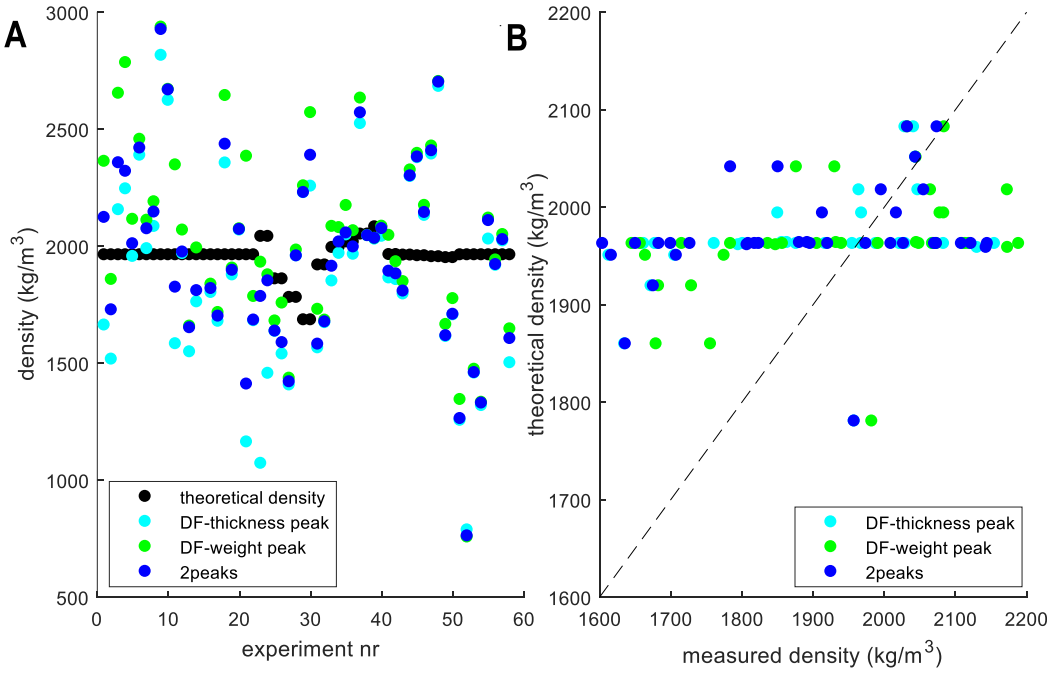

Figure A3.2. Incorrect flow-density calculated by dividing debris flow mass by its volume (determined from its thickness). Theoretical density: using the density following from the original debris-flow mass and volume. DF-thickness peak: using the moment in time of the maximum thickness for the calculation. DF-weight peak: using the moment in time of the maximum weight for the calculation. 2peaks: using the peak of the thickness and the peak of the weight for the calculation.

Statement of originality of the MSc thesis

I declare that:

1. this is an original report, which is entirely my own work,

2. where I have made use of the ideas of other writers, I have acknowledged the source in all instances,

3. where I have used any diagram or visuals I have acknowledged the source in all instances,

4. this report has not and will not be submitted elsewhere for academic assessment in any other academic course.

Student data:

Name: Sjoukje de Lange

Registration number: 4137493

Date: 15-01-2019

Signature: